ADAPTIVE GLIDE SLOPE CONTROL FOR PARAFOIL AND PAYLOAD AIRCRAFT

A Dissertation
Presented to
The Academic Faculty

by

Michael Ward

In Partial Fulfillment
of the Requirements for the Degree
Doctor of Philosophy in the
School of Aerospace Engineering

Georgia Institute of Technology
May 2012

ADAPTIVE GLIDE SLOPE CONTROL FOR PARAFOIL AND PAYLOAD AIRCRAFT

Approved by:

Dr. Mark Costello, Advisor
School of Aerospace Engineering
Georgia Institute of Technology

Dr. Eric Feron
School of Aerospace Engineering
Georgia Institute of Technology

Dr. Eric Johnson
School of Aerospace Engineering
Georgia Institute of Technology

Dr. Nathan Slegers
Department of Mechanical and Aerospace Engineering
University of Alabama, Huntsville

Mr. Steve Tavan
Natick Soldier Research, Development and Engineering Center
U.S. Army

Date Approved: April 27, 2012

ACKNOWLEDGEMENTS

I wish to thank Mark Costello for his advice and support for these past 4 years. I would especially like to thank him for funding my paragliding lessons. They were absolutely crucial to the success of this research, I swear. I wish to thank Steven Tavan and the Natick Soldier Research, Development and Engineering Center for supporting this exciting, fascinating, frustrating, and extremely rewarding research. I wish to thank Alek Gavrilovski, my partner for the majority of this research. Without his fabrication and especially his outstanding piloting skills, this research would literally never have gotten off the ground. I would like to thank Keith Bergeron for his practical insight and advice as an expert in extreme landing accuracy. Finally, I would like to thank my parents for their love, support, and interest.

TABLE OF CONTENTS

LIST OF TABLES

LIST OF FIGURES

SUMMARY

Airdrop systems provide a unique capability of delivering large payloads to undeveloped and inaccessible locations. Traditionally, these systems have been unguided, requiring large landing zones and drops from low altitude. The invention of the steerable, gliding, ram-air parafoil enabled the possibility of precision aerial payload delivery. In practice, the gliding ability of the ram-air parafoil can actually create major problems for airdrop systems by making them more susceptible to winds and allowing them to achieve far greater miss distances than were previously possible. Research and development work on guided airdrop systems has focused primarily on evolutionary improvements to the guidance algorithm, while the navigation and control algorithms have changed little since the initial autnomous systems were developed. Furthermore, the control mechanisms have not changed since the invention of the ram-air canopy in the 1960's. The primary contributions of this dissertation are: 1) the development of a reliable and robust method to identify a flight dynamic model for a parafoil and payload aircraft using minimal sensor data; 2) the first demonstration in flight test of the ability to achieve large changes in glide slope over ground using coupled incidence angle variation and trailing edge brake deflection; 3) the first development of a control law to implement glide slope control on an autonomous system; 4) the first flight tests of autonomous landing with a glide slope control mechanism demonstrating an improvement in landing accuracy by a factor of 2 or more in especially windy conditions, and 5) the first demonstrations in both simulation and flight test of the ability to perform in-flight system identification to adapt the internal control mappings to flight data and provide dramatic improvements in landing accuracy when there is a significant discrepancy between the assumed and actual flight characteristics.

CHAPTER 1

INTRODUCTION

The idea of delivering cargo from an airplane in flight is as old as the airplane itself. Grant Morton became the first skydiver when he jumped from a Wright Model B aircraft in 1911 grasping a folded up parachute in his arms [1-3]. The first instance of aerial re-supply to a military unit was performed by the British in 1915 [4]. Medicine and supplies were dropped from U.S. Marine Corp Aircraft to troops in Nicaragua in 1927 [4-5]. An article in the November, 1929 issue of Popular Mechanics describes the aerial delivery of emergency supplies to flood victims in Alabama and Florida [5].

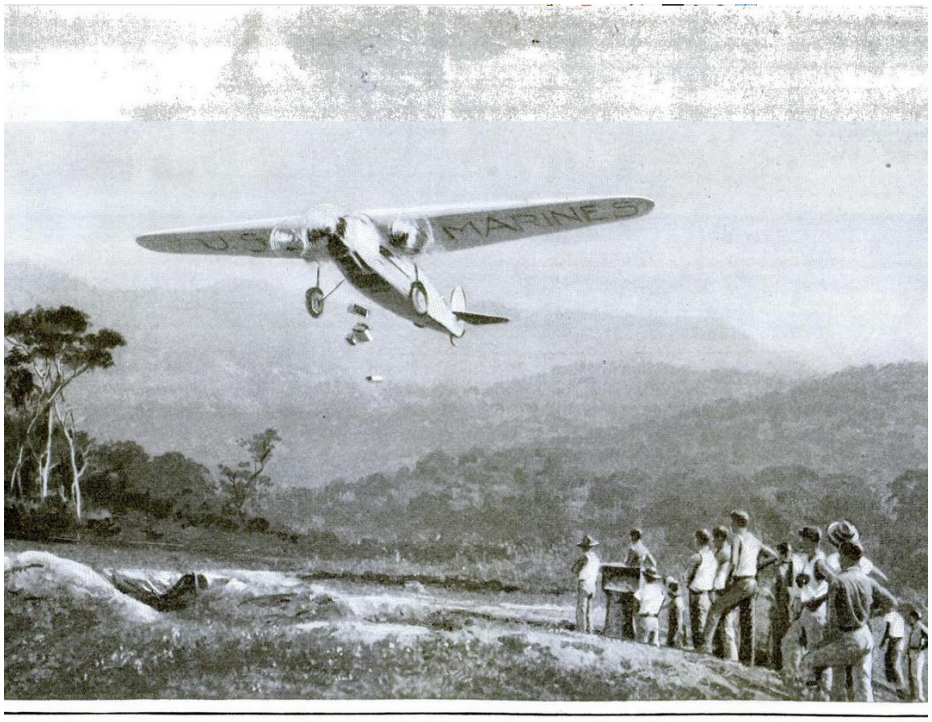

Swooping Close to the Ground in a Tri-Motor Plane, Marine Corps Flyers Toss Out Supplies to a Detachment in Nicaragua

Figure 1.1: Airdrop in 1929 [4]

The use of parachutes to deliver cargo provides a unique capability for the rapid deployment of very large payloads to remote and inaccessible locations. Traditional airdrop systems are based on round, unguided parachutes which slow the descent rate of a payload by producing a large amount of drag. A typical deployment sequence for the delivery of a large payload under multiple round parachutes is shown in Figure 1.2. These systems follow a ballistic trajectory after release and are heavily influenced by winds. To minimize the wind drift during descent, airdrops have historically been performed at the minimum altitude required for reliable canopy openings, which restricted release altitudes to a range of 700-1500 ft depending on load size parachute configuration [5,7]. The primary source of error for these low altitude drops was then the uncertainty in the shape of the ballistic trajectory, especially during canopy opening, and errors in timing the actual release of the payload from the aircraft. To put the scale of the problem in context, the nominal airspeed during payload release is 130 knots for a C-130, and 250 knots for a C-17 [8]. This means that a 1 second delay in releasing the payload from the aircraft translates into a 220 ft ground offset when dropping from a C-130, and a 420 ft ground offset when dropping from a C-17.

In order to expand the range of acceptable release altitudes and improve accuracy, a "Computed Air Release Point" (CARP) is determined based on forecast wind and atmospheric conditions, expected descent rate, and average ballistic parachute release and opening trajectories [9]. More recently, the Precision Aerial Delivery Systems (PADS) program sought to automate the process of selecting the release point.

Figure 1.2: Opening Sequence for Payload Delivery with Multiple Round Parachutes [6]

The PADS automated process incorporates wind forecast data and in situ wind profile measurements provided by dropsondes or weather balloons to simulate the release, opening, and flight through the estimated wind environment to compute an optimum release point for the aircraft operators [10-14]. The use of PADS has been demonstrated in flight test with 2,000 lb class payloads and release altitudes from 18,000-25,000 ft. The standard CARP procedure at these altitudes produced an expected average landing accuracy of approximately 1,000 meters. Average miss distances from the flight tests using PADS were 260 meters when dropping from a C-130 and 308 meters when dropping from a C-17 [13-14]. These numbers represent the average landing accuracy with the current state of the art of unguided aerial payload delivery.

In an effort to improve the landing accuracy with minimal changes to the unguided airdrop architecture, the Affordable Guided Airdrop System (AGAS) was developed. This system is based on the idea of using pneumatic actuators to distort the shape of the circular canopy to induce a slight glide angle and steering control. This control mechanism can achieve glide ratios (the ratio of horizontal to vertical airspeed) on the order of 0.5 [15]. AGAS was flight tested using PADS to compute optimal release points, and average landing accuracies of 100 meters were demonstrated [15-17].

An alternative form of airdrop to drag-based, round parachutes is a form of gliding parachute invented by Domina Jalbert in the 1960's known as a parafoil [18-20]. Parafoils are built of similar materials as typical parachutes, but whereas typical parachutes rely on drag to achieve low descent rates, parafoil canopies are gliding wings with airfoil cross-sections. An example parafoil is shown in Figure 1.3. The parafoil

canopy is constructed out of a series of airfoil shaped cells with openings in the leading edge. Air flows into the leading edge openings, pressurizing the canopy and maintaining the inflated shape. The payload is hung from the canopy through a network of rigging lines. Control is achieved through separate brake lines run to the right and left sides of the trailing edge. Pulling the trailing edge down on one side produces a turn in the direction of the deflected side. Pulling the trailing edge down symmetrically produces a reduction in airspeed.

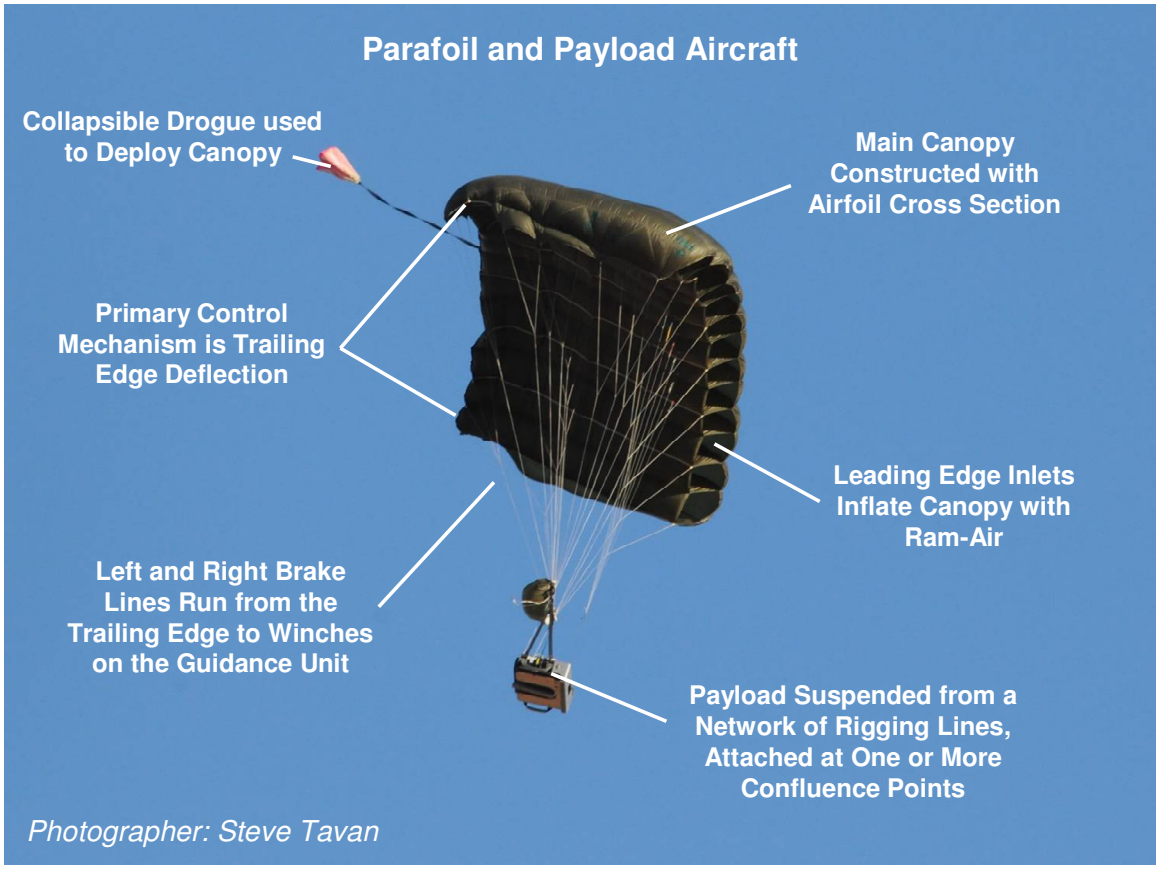

Figure 1.3: Main Features of a Parafoil and Payload Aircraft

Wind tunnel and flight tests performed by Nicolaides [21-24] quickly established that parafoil canopies are extremely stable in flight, capable of glide ratios of 4 to 1 or more,

able to open reliably with payloads weights of 2000 lbs, and capable of practical maximum forward flight speeds in excess of 30 mph while maintaining the ability to slow sufficiently for a safe landing. Parafoils are an attractive option for payload delivery because they provide the low weight and packing volume of a parachute along with the ability maneuver and penetrate winds. In contrast to drag-based airdrop systems, a high altitude release can be beneficial for parafoils since it increases the range that the parafoil can travel from the release point.

The potential application of the parafoil for autonomous guided cargo delivery was recognized immediately, and the first autonomous flight tests were performed in 1966 by Knapp and Barton [25]. Guidance was achieved with radio frequency homing. Radio antennas were placed on the left and right side of the payload, and winches connected to the trailing edge brakes were used to steer towards which ever antenna was receiving the strongest radio signal from a ground-based transmitter. The trajectory from an autonomous flight test using this technique is shown in Figure 1.4. The system landed 600 ft from the target.

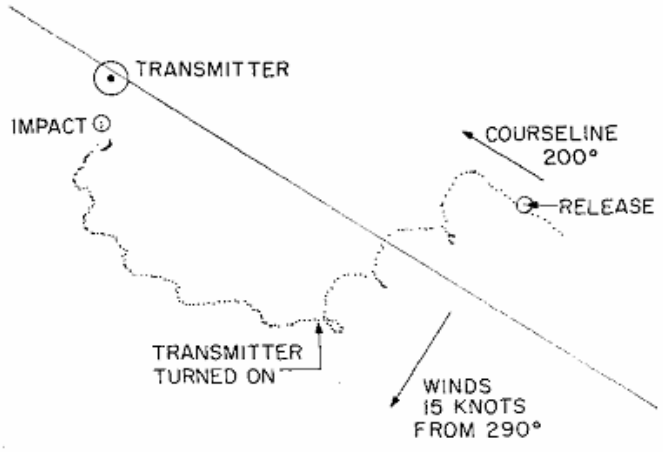

Figure 1.4: Radar Plot of Autonomous Controlled Parafoil Flight in 1966 [25]

Initial autonomous flights simply attempted to home to the target until the system hit the ground. Goodrick tested a variety of different homing control schemes in simulation and showed how the homing pattern over the target and hence landing accuracy was effected by the wind [26]. He and others also demonstrated that if only more sensor information were available it would be possible to plan optimal approach trajectories to land precisely at the target flying into the wind [27]. He then went on to suggest possible hardware implementations involving multiple ground transmitters to achieve sufficiently accurate position feedback for precision landing [28]. An alternative demonstrated by Mayer in 1984 [29] was to use the RF homing method to get the system near the target, then fly the system manually under remote control for the terminal portion of the flight. He reported consistent landings within 25 ft of the target with a 240lb payload.

The advent of the global positioning system finally provided the practical, reliable, and accurate position feedback required to enable precision autonomous airdrop. In the early 1990's, NASA and the U.S. Army started programs to develop guided parafoil aircraft, and the guidance, navigation, and control software for both programs was developed at the C.S. Draper Laboratory [29-32]. The basic flight profile established during these programs, shown in Figure 1.5, is the standard for all current guided parafoil algorithms [33-46]. There are three basic phases to a guided airdrop flight: 1) go to the target, 2) loiter, and 3) execute a landing maneuver. Current autonomous airdrop GNC algorithms typically take advantage of the loiter phase to perform in-flight wind estimation. This wind estimate is then used to plan the final landing maneuver. There is

normally sufficient time during loiter to obtain a very accurate wind estimate, so unless there is some type of malfunction, all landing errors can be traced to some source of uncertainty during the final landing approach. The primary sources of uncertainty are deviations from the assumed model dynamics and deviations from the estimated wind.

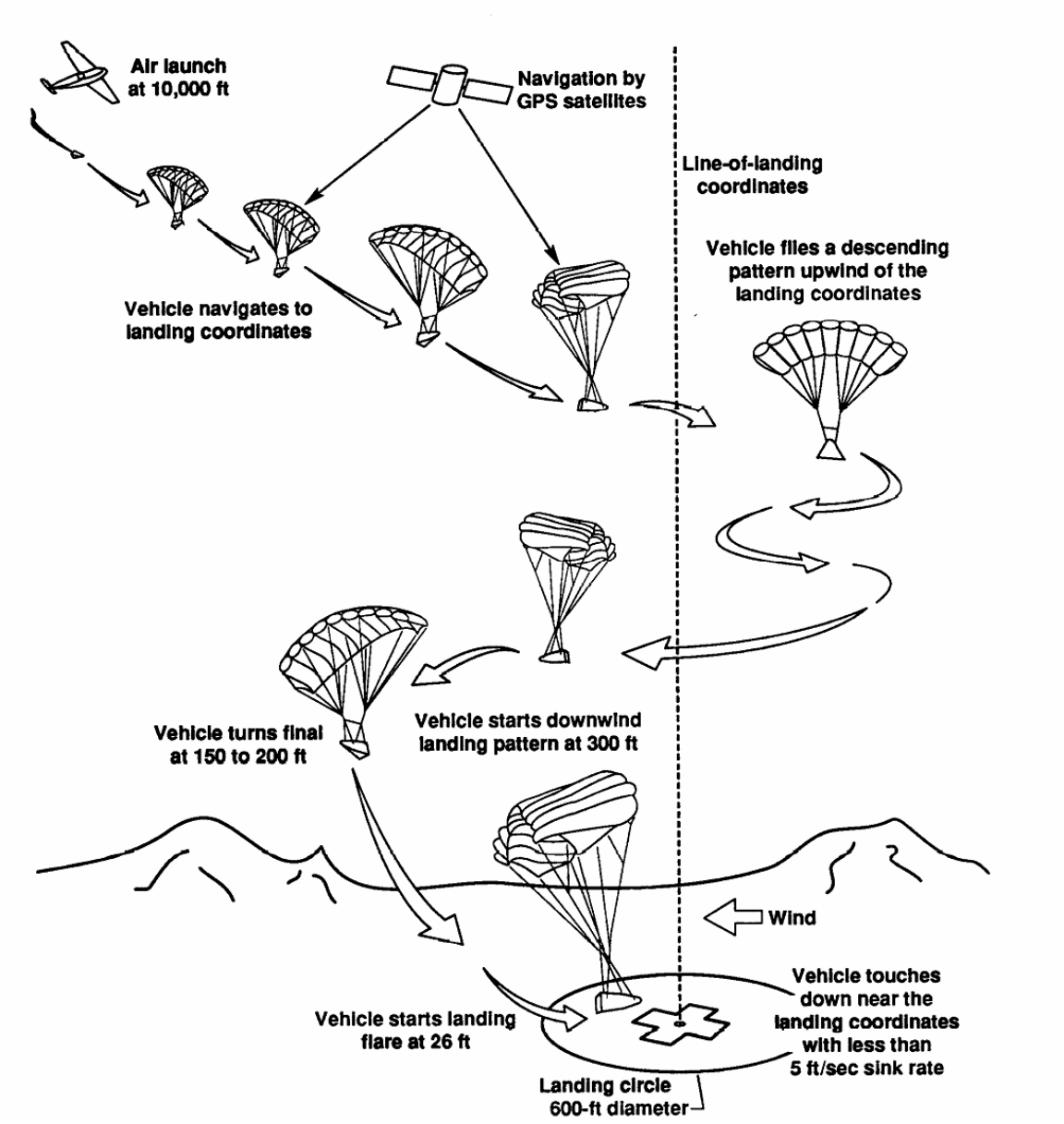

Figure 1.5: Typical Flight Profile for Modern Guided Airdrop [29]

The average accuracy of current guided parafoils is somewhere between 75 meters and 100 meters [47]. There is very little difference in the landing accuracies between current systems because they all have converged to essentially the same approach. One notable exception is the micro parafoil Snowflake, which has a reported average accuracy of 48m and median accuracy of 35 meters [46,48]. This improvement in landing accuracy is likely a result of a combination of two distinguishing factors, 1) the small size of the Snowflake system allows a smaller turning radius, 2) a barometric pressure sensor and magnetic compass are used to supplement the GPS data and provide improved state estimates.

The problem of compensating for deviations in the wind or errors in the assumed flight characteristics during final approach is very difficult. Parafoil control mechanisms have not changed since the invention of the ram-air canopy in the 1960's. The trailing edge of the canopy is deflected downward asymmetrically to turn and symmetrically to change speed or to flare while landing. Symmetric deflection of the trailing edge brakes produces an increase in both lift and drag; this provides a reduction in speed but little change in glide angle until stall. The limited longitudinal control of current airdrop systems makes it difficult to address the possibility of deviations from the assumed wind during landing approach. Yakimenko, Slegers, and Tiaden showed that deviations in the wind below an altitude of 100 meters can shift the landing point of their system by over 100 meters off target [48].

The simplest and most direct way of addressing this problem is to provide a means of controlling the glide slope on final approach. Slegers, Beyer, and Costello demonstrated

the use of variable rigging geometry to obtain glide slope control of a parafoil and payload system [49]. This novel control mechanism is explored in depth in the current work with a flight test program examining the coupled effect of incidence angle and trailing edge brake deflection on the flight characteristics of canopies of two different aspect ratios. Based on this understanding of incidence angle as a control mechanism, a glide slope control algorithm is developed to respond to variations in the wind with optimal incidence angle and brake deflection inputs.

Model uncertainty can be addressed by identifying the needed dynamic and control characteristics in flight using a system identification algorithm. The key quantities to estimate for an autonomous airdrop system are the airspeed, descent rate, and the lateral control response. Recently, the need for in-flight estimation of these characteristics has been recognized and efforts to address this are beginning to appear in the literature. Jann [42] and Carter et al. [45] developed GNC algorithms with the ability to estimate airspeed in flight. Calise [50] developed an adaptive control law for lateral control of a parafoil. In the current work, a thorough examination is performed of the benefits of estimating the system characteristics in-flight with different levels of sensor error and turbulence. A robust methodology is then developed to adapt the internal model of the flight dynamic characteristics to match these in-flight estimates.

Chapter 2 presents a discussion of parafoil modeling and a development of the flight dynamic simulation used throughout the dissertation. In Chapter 3, the system identification methodology used to match the simulation model to flight test data is described. Chapter 4 presents the basic guidance, navigation and control algorithm used

for autonomous landings. In Chapter 5, flight test results exploring the coupling between incidence angle and brake deflection as glide slope control mechanisms are given. Based on the insights from these flight tests, a glide slope control algorithm is developed in Chapter 6. Chapter 7 explains the benefits of and limitations of in-flight system identification and outlines a robust methodology for adapting the internal flight dynamic model to in-flight estimates of the relevant flight characteristics. Finally, Chapter 8 presents simulation and flight test results for autonomous landings using the glide slope controller in a range of atmospheric conditions as well as simulation results showing the related effects of in-flight adaptation and model uncertainty on landing accuracy.

CHAPTER 2

PARAFOIL FLIGHT DYNAMIC MODELING

Modern engineering of airdrop systems leans heavily on flight dynamic modeling and simulation to predict a multitude of drop events virtually so that guidance, navigation, and control (GNC) software can be developed and tested in a cost efficient manner. There is a large body of work on different methods of parafoil dynamic modeling. The simplest approach is to model the entire parafoil and payload aircraft as a rigid body and decouple the longitudinal and lateral dynamics to obtain a reduce order model. One use of these simplified models is to obtain insight into particular aspects of parafoil flight dynamics. As early as 1975, Goodrick [51] developed a 3 degree of freedom (DOF) model to study longitudinal stability and the reponse to changes in incidence angle and brake deflection, Crimi [52] used a 3 DOF lateral model to study lateral stability, and Iosilevskii [53] used a 3 DOF longitudinal model to study the effect of forward and aft shifting of the payload center of gravity. While these reduced order models can provide insight into a particular aspect of parafoil flight dynamics, it is necessary to model the full set of rigid body states in order to provide a realistic environment to test lateral and longitudinal guidance and control algorithms. Goodrick used a 6 degree of freedom model to study the parafoil response to control input, test control laws [54] and eventually test an autonomous guidance algorithm [55]. In reality, the relative motion between the payload and canopy can be significant, which calls for additional degrees of freedom beyond the rigid body motion. Slegers and Costello [56], Mooij et al. [57], and Prakash and Ananthkrishnan

[58] presented 9 degree of freedom models that captured the relative rotations in all three axes between the canopy and payload. Gorman and Slegers, presented a comparison of the dynamics of 6, 7, 8, and 9 degree of freedom parafoil simulations [59]. They concluded that a 7 degree of freedom was adequate to capture the most significant features of the relative motion between the parafoil and payload. They also concluded that at least a 7 degree of freedom is required if any sensor information related to payload orientation is used for control. The goal of the simulation models developed in this dissertation are to provide a sufficiently accurate representation of key vehicle dynamics to provide a realistic test of the autonomous guidance, navigation, and control algorithm using only GPS and barometric pressure for position and velocity feedback. In this situation, the minimal order model which captures the relevant dynamics is a 6 degree of freedom model.

In what follows, the equations of motion for the 6 degree of freedom model are derived. Then the sensor error model used to generate synthetic measurement data. Finally the wind model used to provide realistic atmospheric disturbances is given.

A. Equations of Motion

Figure 2.1 shows a schematic of a parafoil and payload system. With the exception of movable parafoil brakes, the parafoil canopy is considered to be a fixed shape. The canopy is allowed to rotate with respect to the system through the incidence angle, Γ. The combined system of the parafoil canopy and the payload are modeled with 6 DOF, including three inertial position components of the total system mass center as well as the three Euler orientation angles. The canopy aerodynamic forces and moments are

computed about the canopy aerodynamic center (point M in Figure 2.1). The transformation from the body frame to the canopy reference frame is defined by a single axis rotation in pitch by the canopy incidence angle.

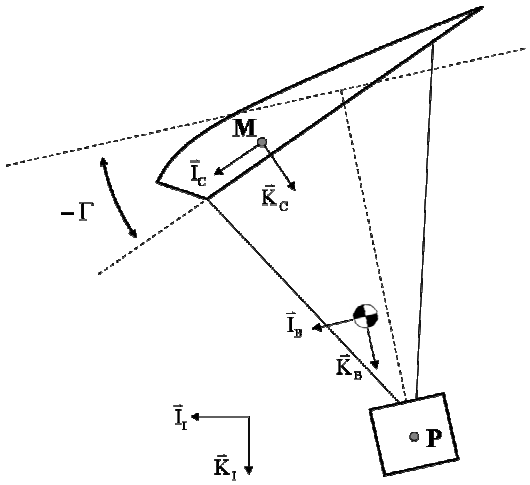

Figure 2.1: Parafoil and Payload Schematic

The kinematic equations for the parafoil and payload system are provided in Eqs. (2.1) and (2.2). The common shorthand notation for trigonometric functions is employed where $\sin(x) \equiv s_x$, $\cos(x) \equiv c_x$, and $\tan(x) \equiv t_x$.

$$\begin{Bmatrix} \dot{x} \\ \dot{y} \\ \dot{z} \end{Bmatrix} = [T_{IB}]^T \begin{Bmatrix} u \\ v \\ w \end{Bmatrix} \tag{2.1}$$

$$\begin{Bmatrix} \dot{\phi} \\ \dot{\theta} \\ \dot{\psi} \end{Bmatrix} = \begin{bmatrix} 1 & s_\phi t_\theta & c_\phi t_\theta \\ 0 & c_\phi & -s_\phi \\ 0 & s_\phi / c_\theta & c_\phi / c_\theta \end{bmatrix} \begin{Bmatrix} p \\ q \\ r \end{Bmatrix} \tag{2.2}$$

The matrix $[T_{IB}]$ represents the transformation matrix from the inertial reference frame to the body reference frame.

$$T_{IB} = \begin{bmatrix} c_\theta c_\psi & c_\theta s_\psi & -s_\theta \\ s_\phi s_\theta c_\psi - c_\phi s_\psi & s_\phi s_\theta s_\psi + c_\phi c_\psi & s_\phi c_\theta \\ c_\phi s_\theta c_\psi + s_\phi s_\psi & c_\phi s_\theta s_\psi - s_\phi c_\psi & c_\phi c_\theta \end{bmatrix} \tag{2.3}$$

The dynamic equations are formed by summing forces and moments about the system CG, both in the body reference frame, and equating to the time derivative of linear and angular momentum respectively.

$$m\left(\begin{Bmatrix} \dot{u} \\ \dot{v} \\ \dot{w} \end{Bmatrix} + [S_\omega^B] \begin{Bmatrix} u \\ v \\ w \end{Bmatrix} \right) = \begin{Bmatrix} X_W \\ Y_W \\ Z_W \end{Bmatrix} + \begin{Bmatrix} X_{AM} \\ Y_{AM} \\ Z_{AM} \end{Bmatrix} + \begin{Bmatrix} X_{A,P} \\ Y_{A,P} \\ Z_{A,P} \end{Bmatrix} + \begin{Bmatrix} X_{A,C} \\ Y_{A,C} \\ Z_{A,C} \end{Bmatrix} \tag{2.4}$$

$$[I_T] \begin{Bmatrix} \dot{p} \\ \dot{q} \\ \dot{r} \end{Bmatrix} + S_\omega^B [I_T] \begin{Bmatrix} p \\ q \\ r \end{Bmatrix} = \begin{Bmatrix} L_{AM} \\ M_{AM} \\ N_{AM} \end{Bmatrix} + [S_{cg,M}^B] \begin{Bmatrix} X_{AM} \\ Y_{AM} \\ Z_{AM} \end{Bmatrix} + [S_{cg,P}^B] \begin{Bmatrix} X_{A,P} \\ Y_{A.P} \\ Z_{A.P} \end{Bmatrix} + \begin{Bmatrix} L_{A,C} \\ M_{A,C} \\ N_{A,C} \end{Bmatrix} \tag{2.5}$$

$S_a^{\ b}$ is the skew symmetric operator, used to express the cross product of two vectors in terms of the components of the vectors in a specified frame. For example, if the vectors **a**, **b**, and **c** are expressed in terms of their components in frame B:

$$\mathbf{c} = \mathbf{a} \times \mathbf{b} \Leftrightarrow \begin{Bmatrix} c_x \\ c_y \\ c_z \end{Bmatrix} = \begin{bmatrix} 0 & -a_z & a_y \\ a_z & 0 & -a_x \\ -a_y & a_x & 0 \end{bmatrix} \begin{Bmatrix} b_x \\ b_y \\ b_z \end{Bmatrix} = [S_a^B] \begin{Bmatrix} b_x \\ b_y \\ b_z \end{Bmatrix} \tag{2.6}$$

Forces appearing in Eq. (2.4) have contributions from weight, aerodynamic loads on the canopy and payload, and apparent mass. The weight contribution is given in Eq. (2.7).

$$\begin{Bmatrix} X_W \\ Y_W \\ Z_W \end{Bmatrix} = mg \begin{Bmatrix} -s_\theta \\ s_\phi c_\theta \\ c_\phi c_\theta \end{Bmatrix} \tag{2.7}$$

Defining the transformation from the body frame to the canopy frame through the canopy incidence angle as $[T_{BC}]$ and defining the wind vector components in the inertial frame as $V_{w,x}$, $V_{w,y}$ and $V_{w,z}$, the aerodynamic velocity of the canopy is given by Eq. (2.8). The aerodynamic velocity of the payload is given by the same equation with the body frame to element transformation equal to the identity matrix.

$$\begin{Bmatrix} \tilde{u} \\ \tilde{v} \\ \tilde{w} \end{Bmatrix} = [T_{BC}] \left(\begin{Bmatrix} u \\ v \\ w \end{Bmatrix} - [S^B_{cg,i}] \begin{Bmatrix} p \\ q \\ r \end{Bmatrix} - [T_{IB}] \begin{Bmatrix} V_{W,x} \\ V_{W,y} \\ V_{W,z} \end{Bmatrix} \right) \tag{2.8}$$

The longitudinal aerodynamic forces on the canopy are functions of the angle of attack of the canopy, the canopy incidence angle, and the level of symmetric trailing edge brake deflection (δ_B). The canopy incidence angle produces a rotation of the canopy reference frame through the transformation matrix $[T_{BC}]$ as shown in Eq. (2.8), which results in a change in angle of attack. Because the incidence angle changes slowly, any dynamics associated with the rate of the incidence angle change are neglected. The basic lift and drag coefficients are determined from lookup tables as functions of angle of attack. The effect of the brakes is to produce a change in the level and slope of the lift and drag curves as well as a change in the effective angle of attack used for the lookup tables. The

basic angle of attack of the canopy, $\alpha_{BASE} = \tan^{-1}(\tilde{w}/\tilde{u})$, is altered by the brake deflection to produce an effective angle of attack, $\alpha = \alpha_{BASE} + \partial\alpha_B \delta_B$, used in all lift and drag calculations. The form of the lift and drag relations are shown in Eqs. (2.9) and (2.10). In addition to the longitudinal forces, a side force is computed proportional to the side slip angle of the canopy, $\beta = \sin^{-1}(\tilde{v}/\tilde{V})$. Equation (2.11) defines the canopy aerodynamic forces in the body reference frame.

$$C_L = C_{L,BASE}(\alpha) + C_{LB}\delta_B + C_{LAB}\alpha\delta_B \tag{2.9}$$

$$C_D = C_{D,BASE}(\alpha) + C_{DB}\delta_B + C_{DA2B}\alpha^2\delta_B \tag{2.10}$$

$$\begin{Bmatrix} X_{A,B} \\ Y_{A,B} \\ Z_{A,B} \end{Bmatrix} = \frac{1}{2}\rho\tilde{V}_A^2 S[T_{BC}]^T \begin{bmatrix} \cos\alpha & 0 & -\sin\alpha \\ 0 & 1 & 0 \\ \sin\alpha & 0 & \cos\alpha \end{bmatrix} \begin{Bmatrix} -C_L \\ C_{YB}\beta \\ -C_D \end{Bmatrix} \tag{2.11}$$

Canopy aerodynamic moments are functions of the angular rates and the level of asymmetric trailing edge brake deflection (δ_A) as shown in Eqs. (2.12)-(2.15).

$$\begin{Bmatrix} L_{A,B} \\ M_{A,B} \\ N_{A,B} \end{Bmatrix} = \frac{1}{2}\rho\tilde{V}_A^2 S \begin{Bmatrix} bC_l \\ cC_m \\ bC_n \end{Bmatrix} \tag{2.12}$$

$$C_l = \frac{b}{2\tilde{V}_A}(C_{lp}p + C_{lr}r) + C_{lA}\delta_A \tag{2.13}$$

$$C_m = \frac{c}{2\tilde{V}_A}C_{mq}q \tag{2.14}$$

$$C_n = \frac{b}{2\tilde{V}_A}(C_{np}p + C_{nr}r) + C_{nA}\delta_A \tag{2.15}$$

The aerodynamic force on the payload consists entirely of profile drag and is given by Eq. (2.16).

$$\begin{Bmatrix} X_{A,P} \\ Y_{A.P} \\ Z_{A.P} \end{Bmatrix} = -\frac{1}{2}\rho S_P C_{D,P}\sqrt{\tilde{u}_P^2 + \tilde{v}_P^2 + \tilde{w}_P^2}\begin{Bmatrix} \tilde{u}_P \\ \tilde{v}_P \\ \tilde{w}_P \end{Bmatrix} \tag{2.16}$$

Parafoils with small mass to volume ratios can experience large forces and moments from accelerating fluid. These are termed "apparent mass" effects. A precise accounting of these effects can substantially complicate the dynamic equations, but it is possible to obtain a good approximation of the effects with only a few terms. The approximate forms used for the apparent mass forces and moments are given in Eqs. (2.17) and (2.18) [60-62]. Parametric approximations given by Lissaman and Brown are used to determine the apparent mass and inertia coefficients in Eq. (2.19).

$$\begin{Bmatrix} X_{AM} \\ Y_{AM} \\ Z_{AM} \end{Bmatrix} = -[I_{AM}]\left(\begin{Bmatrix} \dot{\tilde{u}} \\ \dot{\tilde{v}} \\ \dot{\tilde{w}} \end{Bmatrix} - [S^B_{cg,M}]\begin{Bmatrix} \dot{\tilde{p}} \\ \dot{\tilde{q}} \\ \dot{\tilde{r}} \end{Bmatrix}\right) \tag{2.17}$$

$$\begin{Bmatrix} L_{AM} \\ M_{AM} \\ N_{AM} \end{Bmatrix} = -[I_{AI}]\begin{Bmatrix} \dot{\tilde{p}} \\ \dot{\tilde{q}} \\ \dot{\tilde{r}} \end{Bmatrix} \tag{2.18}$$

$$[I_{AM}] = \begin{bmatrix} A & 0 & 0 \\ 0 & B & 0 \\ 0 & 0 & C \end{bmatrix}, \quad [I_{AI}] = \begin{bmatrix} P & 0 & 0 \\ 0 & Q & 0 \\ 0 & 0 & R \end{bmatrix} \tag{2.19}$$

The dynamic equations of motion are found by substituting all forces and moments into Eqs. (2.4) and (2.5), resulting in the matrix solution in Eqs. (2.20) to (2.22).

$$\begin{bmatrix} m[I]+[I_{AM}] & -[I_{AM}][S^B_{cg,M}] \\ [S^B_{cg,M}][I_{AM}] & [I_T]+[I_{AI}]-[S^B_{cg,M}][I_{AM}][S^B_{cg,M}] \end{bmatrix} \begin{Bmatrix} \dot{u} \\ \dot{v} \\ \dot{w} \\ \cdots \\ \dot{p} \\ \dot{q} \\ \dot{r} \end{Bmatrix} = \begin{bmatrix} B_1 \\ \cdots \\ B_2 \end{bmatrix} \tag{2.20}$$

$$B_1 = -m[S^B_\omega] \begin{Bmatrix} u \\ v \\ w \end{Bmatrix} + \begin{Bmatrix} X_W \\ Y_W \\ Z_W \end{Bmatrix} + \begin{Bmatrix} X_{A,P} \\ Y_{A,P} \\ Z_{A,P} \end{Bmatrix} + \sum_i \begin{Bmatrix} X_{A,i} \\ Y_{A,i} \\ Z_{A,i} \end{Bmatrix} \tag{2.21}$$

$$B_2 = -[S^B_\omega][I_T] \begin{Bmatrix} p \\ q \\ r \end{Bmatrix} + [S^B_{cg,P}] \begin{Bmatrix} X_{A,P} \\ Y_{A,P} \\ Z_{A,P} \end{Bmatrix} + \sum_i [S^B_{cg,i}] \begin{Bmatrix} X_{A,i} \\ Y_{A,i} \\ Z_{A,i} \end{Bmatrix} \tag{2.22}$$

Equation (2.20) represents a set of coupled, nonlinear differential equations. The matrix on the left hand side of Eq. (2.21) is a function of the mass and geometry properties of the parafoil. The geometry of the parafoil is assumed to be fixed, so this matrix is constant and only needs to be inverted once at the beginning of the simulation. With specified initial conditions, the states can be numerically integrated forward in time.

B. Sensor Model

GPS sensor errors are modeled as exponentially correlated Gaussian noise. The form of the measurement signals is given in Eq. (2.23), where y_k is the actual value, v_k is the measured value, n_k is the measurement noise.

$$v_k = y_k + n_k$$

$$n_k = e^{-\Delta t/\tau} n_{k-1} + \xi_k \sqrt{1 - e^{-2\Delta t/\tau}} \tag{2.23}$$

$$\xi_k \sim N(0, \sigma_N)$$

Sensor parameters were selected to represent a low-cost, commercially available GPS receiver and barometric altimeter, and are listed in Table 2.1. A 4 Hz update rate is assumed for the measurements as well as the guidance unit.

Table 2.1: GPS Sensor Error Parameters

	Horizontal Position	Horizontal Velocity	Vertical Position	Vertical Velocity
Standard Dev. (σ_N)	2 m	0.2 m/s	3 m	0.2 m/s
Time constant (τ)	20 s	20 s	1 s	1 s

C. Wind Model

The wind model used is a discrete implementation of the Dryden turbulence spectrum [63-67]. Wind gust velocities and angular rate components are computed for all three axes by driving discrete filters with unit-variance, independent white noise signals (η_i) as shown in below .

$$u_g(k+1) = \left(1 - \frac{V}{L_u}\Delta t\right) u_g(k) + \sqrt{2\Delta t \frac{V}{L_u}}\sigma_u \eta_1 \tag{2.24}$$

$$v_g(k+1) = \left(1 - \frac{V}{L_v}\Delta t\right) v_g(k) + \sqrt{2\Delta t \frac{V}{L_u}}\sigma_v \eta_2 \tag{2.25}$$

$$w_g(k+1) = \left(1 - \frac{V}{L_w}\Delta t\right) w_g(k) + \sqrt{2\Delta t \frac{V}{L_w}}\sigma_w \eta_3 \tag{2.26}$$

$$p_g(k+1) = \left(1 - \frac{2.6}{\sqrt{2L_w b}}\Delta t\right) p_g(k) + \sqrt{2\Delta t \frac{2.6}{\sqrt{2L_w b}}} \frac{1.9}{\sqrt{2L_w b}} \sigma_w \eta_4 \tag{2.27}$$

$$q_g(k+1) = \left(1 - \frac{\pi V}{4b}\Delta t\right) q_g(k) - \frac{\pi}{4b}(w_g(k+1) - w_g(k)) \tag{2.28}$$

$$r_g(k+1) = \left(1 - \frac{\pi V}{3b}\Delta t\right) r_g(k) + \frac{\pi}{3b}(v_g(k+1) - v_g(k)) \tag{2.29}$$

The turbulence length scales are set according to the MIL-F-8785C standard.

$$L_w = h, \;\; L_u = L_v = \frac{h}{(0.177 + 0.000823h)^{1.2}} \tag{2.30}$$

The length scale and airspeed set time constants of the turbulent gusts. At high altitude, the length scales are large and the resulting time constants are large, which creates slowly varying turbulent gust components. As the altitude becomes low, the length scales decrease, the time constants decrease, and the turbulent gust components vary more rapidly. The standard deviation of the wind gust components sets the turbulence level. The standard deviation of the horizontal wind components are related to the standard deviation of the vertical wind component.

$$\sigma_u = \sigma_v = \frac{\sigma_w}{(0.177 + 0.000823h)^{0.4}} \tag{2.31}$$

The standard deviation of the vertical wind component is left as an input parameter to the simulation model. This allows simulations to be run at a variety of wind and

turbulence conditions by specifying only two parameters, the average wind speed and the standard deviation of the vertical wind component.

Example wind profiles from an altitude of 100 meters down to the ground are shown in Figure 2.2. The standard deviation of the vertical wind component was set at 0.8 m/s and the average wind speed was set at 5 m/s. The horizontal wind component in the average wind direction is labeled “head wind”, since this is the wind component that would be opposing the parafoil on final approach. Notice that despite inputting only a constant horizontal wind speed, the turbulence model results in a realistic wind profile with large spatial variations in all 3 wind components.

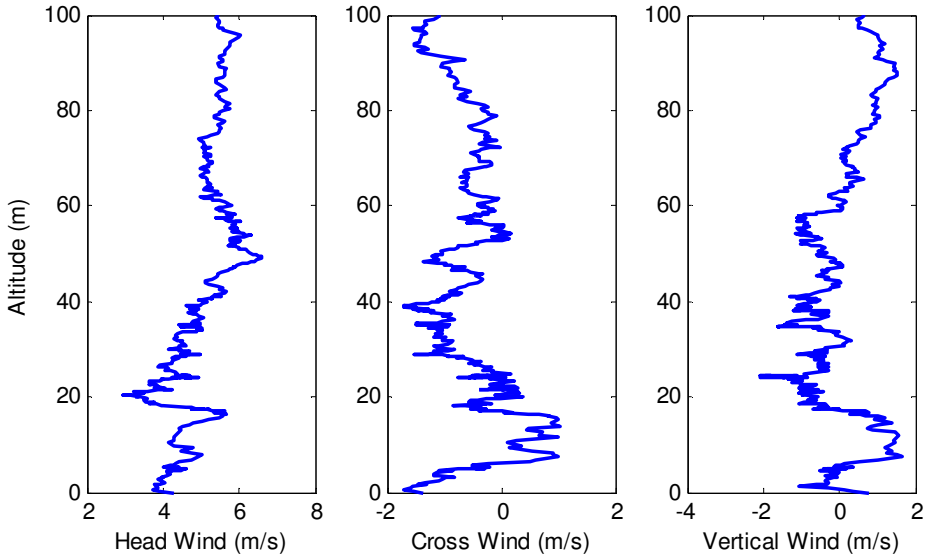

Figure 2.2: Example Profiles for with Constant Mean Wind and Dryden Turbulence

CHAPTER 3

PARAFOIL SYSTEM IDENTIFCATION

For the guidance, navigation, and control development to be successful, reasonably accurate dynamic simulation models that exhibit similar nonlinear behaviors to the actual airdrop systems are required. These models are obtained by performing system identification on flight test data of the system under development. There are a number of peculiar aspects to parafoil and payload systems that make it difficult to apply conventional system identification procedures used for aerospace systems. Parafoil and payload systems are unique because typically there is very little sensor information available, the sensors that are available are separated from the canopy by a complex network of flexible rigging, the systems are very sensitive to wind and turbulence, the systems exhibit a number of nonlinear behaviors, and the systems exhibit a high degree of variability from flight to flight. A specialized system identification procedure for parafoil and payload aircraft was developed to provide reliable 6 degree of freedom parafoil and payload models from GPS data alone. This is the method used to create the simulation model of the flight test vehicle used for autonomous landing accuracy predictions. A description of the system identification method is given, and some sample results comparing the simulation model to flight test results are given.

A. Specialized System Identification Method

The traditional aerodynamic model used for dynamic simulation of aircraft is created using a linearized representation of the system dynamics near trimmed flight [68]. The main difficulty with this representation is the need to identify a large number of aerodynamic coefficients. The coefficients are often correlated with one another and a large number of them can typically be neglected, though the particular coefficients that can be neglected may vary from aircraft to aircraft. The problem is difficult enough for fixed wing aircraft and rotorcraft, but it becomes even more difficult for airdrop systems. The primary differences that cause these difficulties are the limited number of control channels available to excite the system dynamics (the only means of control typically used on a parafoil is differential or symmetric deflection of the trailing edge), the sensitivity of these systems to wind (due to low flight speed and low mass to volume ratios), and the limited amount and quality of available sensor data (due to the typical constraint that sensors must be confined to the payload which is separated from the canopy by a complex network of flexible rigging).

A variety of methods have been developed for air vehicle system identification [69-70]. The two methods that are best suited to the current problem are the output error method (OEM), which is the most common method for parameter identification from noisy measurements, and identification through an extended Kalman filter, which is commonly used when there is both measurement and process noise. These two methods can also be combined to form the filter error method.

A number of efforts have applied aerodynamic parameter identification to airdrop systems [71-78]. Jann, Doherr, and Gockel describe the development of a highly instrumented parafoil and payload research platform, ALEX, incorporating a global positioning system (GPS) receiver, magnetometers, rate gyros, accelerometers, air data probes, and video cameras to address the problem of generating enough data for system identification [71]. With this system, they performed an extensive investigation into the problem of aerodynamic parameter identification for parafoil and payload systems [72-74]. Their initial approach was to develop 3 and 4 DOF models (the extra degree of freedom was added to account for significant bank angles). These models required a small number of coefficients to be identified and good results were obtained [72]. Efforts to identify the extra coefficients needed for a 6 DOF model were more difficult, and a creative approach to generating the coefficients by applying lifting line theory to an arc anhedral wing was used to generate initial estimates of all of the parameters as well as approximate relationships for correlated coefficients [73]. Finally, an 8 DOF model was developed incorporating the relative motion of the payload using the same approach [74]. In each case, the use of the air data probe allowed the estimation of wind and turbulence so that the output error method could be applied on data with the effect of the wind removed. Even so, the process required frequent intervention to produce good results [74]. Hur and Valasek describe the development of another highly instrumented platform including an IMU, flow sensors, and even accelerometers installed in the mid-section of the parafoil [75]. They demonstrated the identification of a linear 8 DOF model from simulation data using an observer/Kalman filter identification method described by

Valasek and Chen [76]. Kothandaraman and Rotea described the use of a computationally efficient method to identify coefficients for a 6 DOF circular parachute model assuming perfect knowledge of the winds [77]. Yakimenko and Statnikov presented a method for identifying aerodynamic coefficients of an 8 DOF parafoil model using a multi-criteria optimization method beginning with a parameter space investigation to help address the problems of local minima and infeasible regions in the parameter space [78]. In particular, they noted that most of the aerodynamic coefficients in a general model of a parafoil and payload system seem to be strongly correlated, there are many sets of parameters that produce equally good reproductions of the observed flight data, and the additional degrees of freedom accounting for payload motion helped to match the natural eigenvalues of the roll, pitch, and yaw measurements but did not effect the matching of the system trajectory.

All of these works approach the problem in slightly different ways, but a common thread among them is the necessity of using a highly instrumented platform specialized for the system identification task in order to obtain sufficient data for succesful aerodynamic parameter identification. In contrast to these specialized platforms, fielded airdrop systems have only a single GPS receiver [41,43,45]. This is desirable to reduce cost and complexity, especially because the GPS receiver does not require any pre-flight calibration. This dissertation describes a reliable system identification procedure that requires only GPS data, which would allow the system identification task to be performed using the same hardware intended for the field. This is highly advantageous in streamlining the development cycle of an airdrop system. Of course, if it is possible to

obtain measurements in addition to GPS, it would not make sense to restrict the system identification to GPS data alone. In this case, the system identification procedure described here could be used to develop an approximate model based on GPS alone which could then be refined with whatever additional sensor information is available. Depending on the available sensor data, this refinement could be performed using similar methods to the existing airdrop identification methods mentioned above [71-77]. Another possibility is that the model made from GPS data using the proposed procedure could be simply augmented to capture un-modeled dynamics observed in the additional sensor channels using more general system identification techniques such as those recently developed by Majji, et al. [79,80].

A number of techniques for deriving particular aspects of the flight dynamic characteristics of a parafoil and payload system using only GPS data have been described [41,43,45]. The restricted amount of sensor information available leads to a very restricted dynamic model of the system, normally a linear 3 degree of freedom representation. Typically, only the steady state longitudinal characteristics are modeled by developing a simple model of air speed and glide path angle as a function of symmetric brake input; lateral dynamics consist of modeling the system heading rate dynamics as a first or second order filter of the asymmetric brake input (trailing edge deflection is commonly referred to as a brake input). In contrast, the system identification method developed here produces a 6 degree of freedom, nonlinear simulation model using only GPS data. This type of simulation model is beneficial during GNC

development to ensure that the guidance and control algorithms are robust to nonlinear behaviors that may not be captured by simpler representations.

The key to developing a six degree of freedom model from GPS data alone is the use of an aerodynamic model which requires the identification of a minimum number of coefficients. An alternative to applying the standard aerodynamic model of a point with force and moment coefficients was used by Slegers and Costello to explore control issues with parafoil and payload systems [55]. Their model makes use of 5 discrete canopy elements producing only lift and drag, so aerodynamic moments and side force are produced by the orientation of the elements and their displacement from the center of mass. This is highly attractive for system identification with minimal sensor data because only lift and drag coefficients need to be estimated to obtain a complete nonlinear 6 DOF simulation model, and these coefficients can be estimated entirely from steady state information.

While the aerodynamic model used in [55] is very convenient for system identification, it is more computationally efficient to use a "point" aero model in simulation, where the aerodynamic forces and moments for the entire canopy are determined at single point. This is the form of the aerodynamic model used in the flight dynamic simulation model described in the previous chapter. The additional aerodynamic coefficients required for the point model are simply set to match the dynamic response of the discrete canopy model produced from the system identification procedure.

The proposed system identification method is summarized in Figure 3.1. The main idea is to match the steady state response to control input extracted from segments of

flight test data. To this end, the majority of the procedure is dedicated to processing flight test data to obtain high quality estimates of the steady state lift, drag, and turn rate response to control input. Aerodynamic coefficients in the simulation model are then used to match these extracted steady state characteristics rather than the flight test data directly. For this procedure, validation refers to checking the identified model against data from a flight that was not used during the matching process.

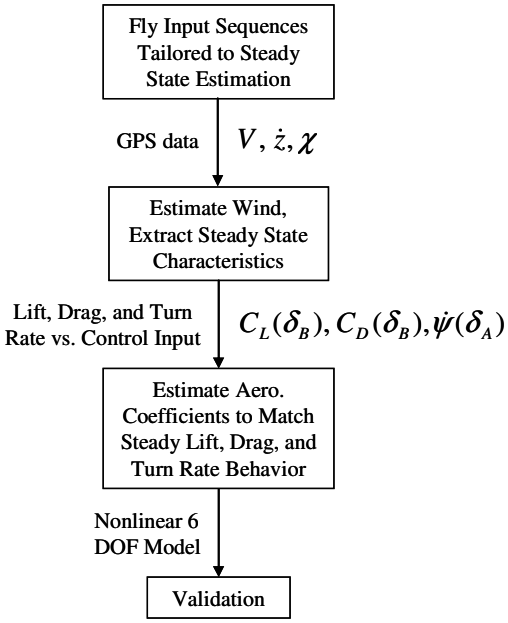

Figure 3.1: System Identification Procedure

1. Input sequences

The structure of the input sequence is critical to obtaining high quality data for system identification. The sequence must ensure that both steady state and transient characteristics can be estimated, and the sequences for each flight must be arranged so that the loss of any single flight is not detrimental to the system identification effort.

The input sequences were designed primarily based on the need to generate high quality estimates of the steady state characteristics of the parafoil and payload system.

This requires relatively long periods of constant control input at various combinations of symmetric and asymmetric brake deflection. Given the total amount of flight testing time available, the number of control input combinations to be tested was chosen so that at some point during flight testing, each control input would be held for two to four times the amount of time necessary for the system to reach steady state. This ensures that there will be enough data available after the system has reached equilibrium to average the steady state response over a series of measurements to reduce the influence of sensor errors and turbulence. In addition, the order of the control input combinations are selected so that the system will receive doublet maneuvers in both symmetric and asymmetric brakes as it transitions from one control combination to the next. This ensures the system is excited sufficiently so that the transient characteristics can be determined. The actual control sequences used in flight test are shown below in the results section.

2. Extracting Steady State Lift, Drag and Turn Rate

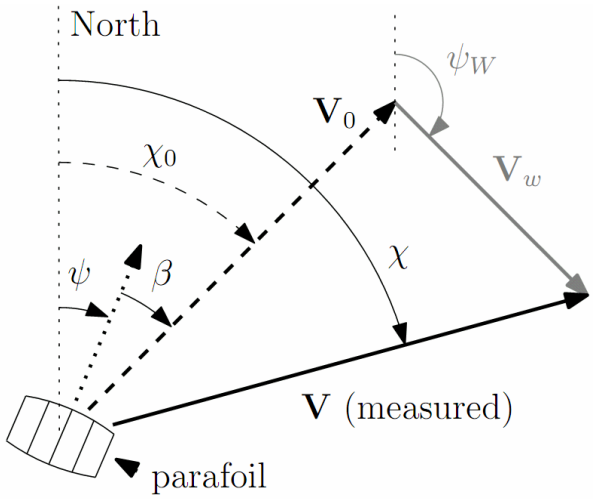

Figure 3.2: Decomposing Measured Velocity Vector

The first step in the system identification process is wind estimation. The ground track velocity measured with GPS can be decomposed into an airspeed vector ($\boldsymbol{V}_0$) and wind vector ($\boldsymbol{V}_w$) as shown in Figure 3.2. Since the ground track velocity vector is the only measured quantity, solution of the vector diagram is an underdetermined problem. Solution of the vector diagram requires a series of measurements at different azimuth angles.

The approach taken is to break the flight into segments of constant control deflection, then assume a constant forward airspeed (V_0) and wind vector for each segment. This leaves three unknowns (two wind vector components and the airspeed) for each of the flight segments. For a series of *n* measurements taking during a constant control segment, the *x* (North) and *y* (East) components of the *i*th measurement of ground track velocity can be decomposed into a wind component and an airspeed component:

$$\dot{x}_i = V_{W,X} + V_0 \cos(\psi_i), \quad \dot{y}_i = V_{W,Y} + V_0 \sin(\psi_i) \tag{3.1}$$

$$V_0^2 = (\dot{x}_i - V_{W,X})^2 + (\dot{y}_i - V_{W,Y})^2 = V_i^2 + V_W^2 - 2(\dot{x}_i V_{W,x} + \dot{y}_i V_{W,Y}) \tag{3.2}$$

For the constant control segment, the airspeed and wind vector are assumed constant, so these terms can be removed from Eq. (3.2) by subtracting the expected values:

$$V_0^2 - E(V_0^2) = 0 = V_i^2 - E(V_i^2) - 2\left((\dot{x}_i - E(\dot{x}_i))V_{W,x} + (\dot{y}_i - E(\dot{y}_i))V_{W,Y}\right) \tag{3.3}$$

where the expected values of the measured quantities are estimated by sample means:

$$E(V_i^2) = \mu_{V2}, \quad E(\dot{x}_i) = \mu_{\dot{x}}, \quad E(\dot{y}_i) = \mu_{\dot{y}} \tag{3.4}$$

The problem of estimating the wind vector components for the constant control segment can now be cast as a linear regression problem as shown in Eq. (3.5). Once the wind vector components have been calculated, the airspeed can be estimated for each measurement according to Eq. (3.6). The steady state airspeed of the vehicle for a given control deflection is obtained as the average of the airspeed estimates over a particular constant control flight segment.

$$\begin{bmatrix} \dot{x}_1 - \mu_{\dot{X}} & \dot{y}_1 - \mu_{\dot{Y}} \\ \vdots & \vdots \\ \dot{x}_n - \mu_{\dot{X}} & \dot{y}_n - \mu_{\dot{Y}} \end{bmatrix} \begin{Bmatrix} V_{W,X} \\ V_{W,Y} \end{Bmatrix} = \frac{1}{2} \begin{Bmatrix} V_1^2 - \mu_{V2} \\ \vdots \\ V_n^2 - \mu_{V2} \end{Bmatrix} \tag{3.5}$$

$$\hat{V}_{0,i} = \sqrt{(x_i^2 - V_{W,X}) + (y_i^2 - V_{W,Y})}\,, \quad \hat{V}_0 = \mu_{V0} \tag{3.6}$$

If the system flies in a straight line, the ground track velocity components will be constant and the matrix on the left handed side of Eq. 3.5 will contain only measurement noise. The conditioning of the problem is improved by adding measurements from a variety of azimuth angles. Each constant control segment will create a constant turn rate and will contain a continuous string of measurements over a span of heading angles. Insight into the effectiveness of airspeed estimation using the specified technique can be given by assuming that GPS measurements are available at a discrete number of heading angles equally spaced over a span $\Delta\psi$. Eq. (3.5) can be solved in closed form and the propagation of GPS measurement errors can be determined analytically for a given number of measurements. An upper bound on the analytical solutions with as few as three heading measurements can be expressed simply by Eq. (3.7).

$$\sigma(\hat{V}_0) < \frac{\sigma(V_{GPS})}{\sin(\delta/4)^2}, \quad \delta = \min(|\Delta\psi|, 2\pi) \tag{3.7}$$

As the heading angle span tends to zero, the airspeed estimate error is unbounded, and as the heading angle span tends to a complete circle, the airspeed estimate error is bounded by the GPS velocity measurement error. If the airspeed error bound obtained from Eq. (3.7) for a particular flight segment is unacceptably large, the wind estimates from adjacent segments of the same flight can be averaged and used in Eq. (3.6).

Once the airspeed is determined, steady state lift, drag and turn rate data can be extracted for each segment of constant control deflection. Based on the vector diagrams in Figure 3.3, lift and drag can be calculated from turn rate, airspeed, and descent rate data according to Eqs. (3.8) through (3.10). The steady state lift and drag data is then converted into coefficient form for matching to simulation.

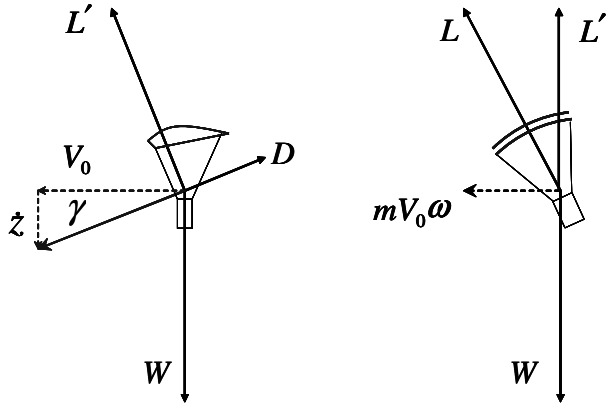

Figure 3.3: Relationship of Lift and Drag to Velocity

$$1/\tan\gamma = V_0/\dot{z} = L'/D \tag{3.8}$$

$$L' = W\cos\gamma \tag{3.9}$$

$$L = \sqrt{L'^2 + (mV_0\omega)^2} \tag{3.10}$$

3. Matching Simulation Model to Steady State Data

The rigging of the parafoil and payload system is fixed, which implies that for a given symmetric brake deflection there exists a single trim angle of attack. This means that the lift and drag vs. angle of attack behavior cannot be estimated from steady state flight test data for a typical airdrop system because the steady state data contains no angle of attack variation.

Nicolaides [19] conducted extensive wind tunnel tests on airdrop canopies and compiled trends of lift and drag vs. angle of attack behavior as a function of aspect ratio. The lift and drag vs. angle of attack coefficients (C_{LA} and C_{DA2}) were selected based on these empirical trends. For the canopy element representation, C_{DA2} is assumed to be constant across the span, while C_{LA} is varied to approximate an elliptical lift distribution while maintaining the lift curve slope of the entire canopy at the desired value. The shape of the lift and drag vs. angle of attack curves are set according to experimental trends, leaving the level of the lift and drag curves to be set to match the trim characteristics observed in flight. Three remaining parameters, C_{L0}, $C_{D0,}$ and the canopy incidence angle are required to determine the trimmed flight condition for the simulation model. For simplicity, C_{L0} is fixed at zero so that C_{D0} and the canopy incidence angle can be set to match the trim lift and drag coefficients derived from flight test. The remaining aerodynamic coefficients (C_{LB} , C_{LB3} , C_{DB} , and C_{DB3}) are associated with steady state response to brake deflection. These coefficients determine the change in longitudinal trim of the system under symmetric braking as well as the change in lateral "trim" of the

system under asymmetric braking. Lateral "trim" is used here to refer to a flight condition in which the system has reached a steady state turn rate under an asymmetric brake input. The small fins under the outboard edges of the canopy will also have an effect on the lateral trim condition. The lift and drag characteristics of these fins were fixed, but their area was allowed to vary. The logic behind this choice is that the effective area of the fins can be increased to account for spanwise effects not modeled by the five main panels. This leaves a total of 5 parameters to be determined to match flight test data for steady state lift and drag at different levels of symmetric brake as well as steady state turn rate at different levels of asymmetric brake.

Longitudinal trim is determined according to Eq. (3.11), which represents a system of three nonlinear equations (nonlinear due to the relationship between trim velocity, angle of attack, and aerodynamic forces). Lateral trim is determined according to Eq. (3.12), which represents a system of 8 nonlinear equations. Lift coefficient is assumed to vary linearly with angle of attack, so there is only one possible trim condition for a given control input. The quadratic relationship between drag coefficient and angle of attack creates a singularity when angle of attack is zero, so the initial guess for the trim velocity components should result in a positive angle of attack (this implies setting the initial guesses for u and w to positive numbers). In the author's experience, quadratic convergence to the trim condition is achieved from the first iteration if the initial guess for the trim velocity components are set to average values observed in flight test.

$$\text{given: } \{\phi, v, p, q, r\}^T = 0, \text{ find: } \{\theta, u, w\}^T, \text{ s.t. } \{\dot{\theta}, \dot{u}, \dot{w}\}^T = 0 \tag{3.11}$$

$$\text{find: } \{\phi, \theta, u, v, w, p, q, r\}^T, \text{ s.t. } \{\dot{\phi}, \dot{\theta}, \dot{u}, \dot{v}, \dot{w}, \dot{p}, \dot{q}, \dot{r}\}^T = 0 \tag{3.12}$$

A nonlinear set of trim equations can be solved to determine steady state behavior at a specified control setting for a given set of aerodynamic parameters. The goal of the system identification exercise is to solve a nonlinear regression problem to determine the aerodynamic parameters such that the trim lift, drag and turn rate vs. control input behavior of the simulation model matches flight test data. Both the nonlinear regression and the nonlinear trim problem are well-behaved so the details of the solution procedure are not critical. The nonlinear regression to determine the aerodynamic parameters is performed using the Levenberg-Marquardt method, while the nonlinear trim equations are solved at each iteration of the aerodynamic parameters using the Newton-Raphson method [81].

B. Example Results

A simulation model was generated to match flight test results for the parafoil and payload aircraft used for autonomous flight testing. The system is described in Chapter 8 of this dissertation in the description of the flight test results, but a comparison of the simulation model to some flight test data is given here to demonstrate the results of the system identification technique. The first set of results is for a step input in symmetric brake deflection. The control input is shown in Figure 3.4 and consists of a 12 cm step in brake deflection (positive indicating trailing edge down). To put this in context, the canopy stalls with 18 cm of brake deflection. The airspeed and descent rate response of the simulation model are compared to flight test data in Figure 3.5 and Figure 3.6.

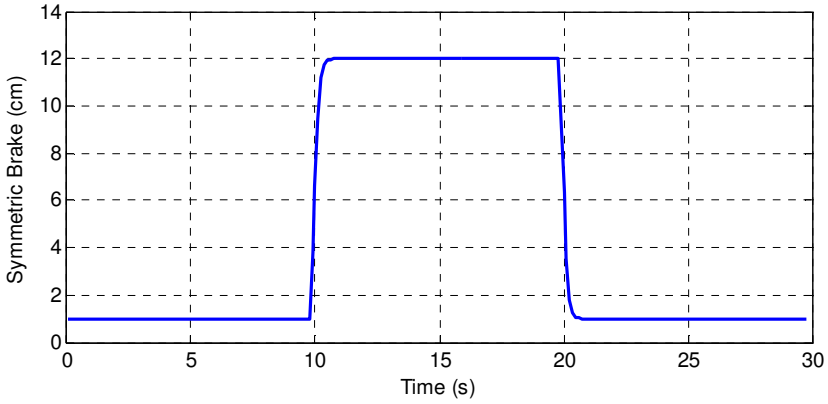

Figure 3.4: Step Brake Input

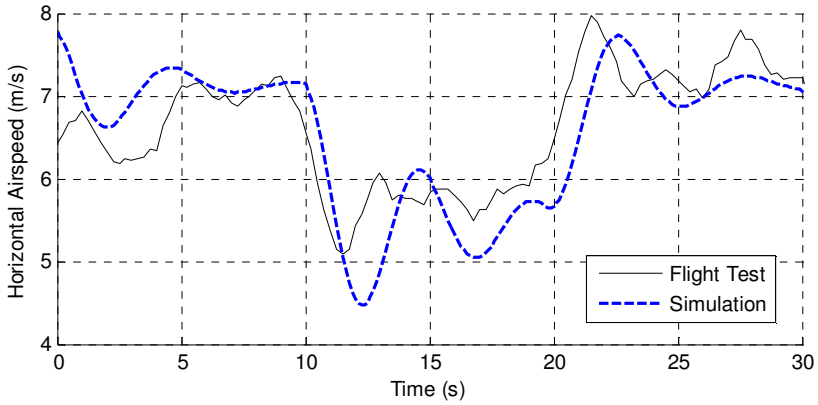

Figure 3.5: Airspeed Response to Brake Step

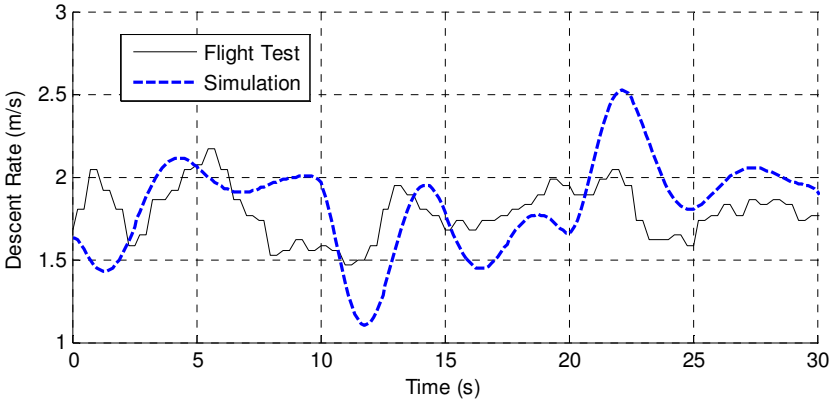

Figure 3.6: Descent Rate Response to Brake Step

The second set of results is for a step input in incidence angle. The control input is shown in Figure 3.7 and consists of pulling the nose of the canopy down 6 cm for a duration of 12 seconds. This corresponds to an incidence angle change of -6 degrees. To put this in context, the canopy collapses when the incidence angle is lowered beyond 12 degrees. The airspeed and descent rate response of the simulation model are compared to flight test data in Figure 3.8 and Figure 3.9.

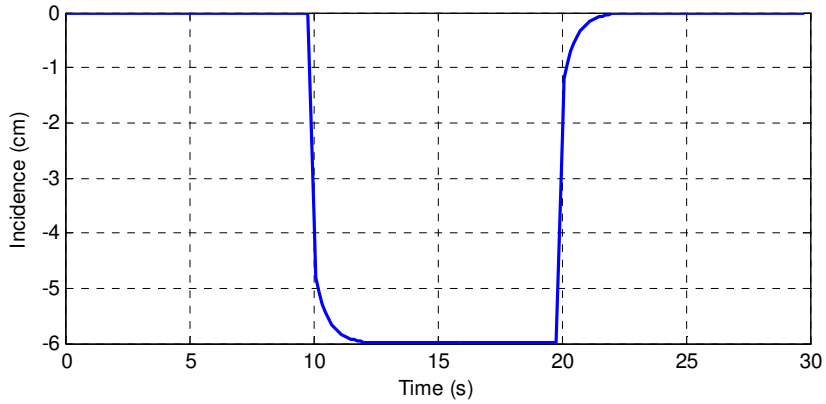

Figure 3.7: Incidence Angle Step

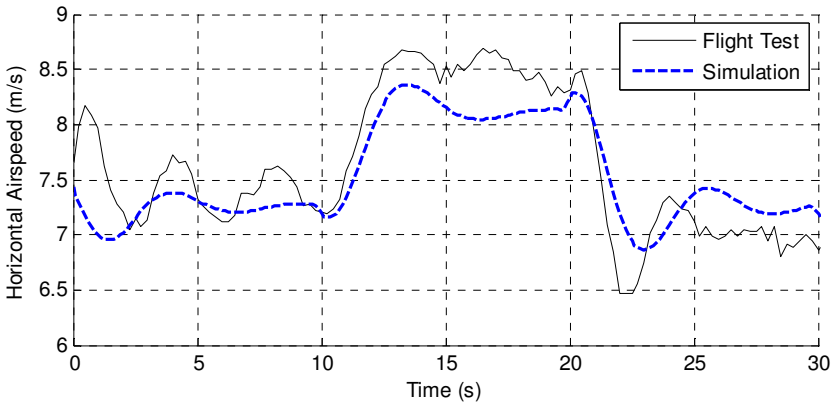

Figure 3.8: Airspeed Response to Incidence Step

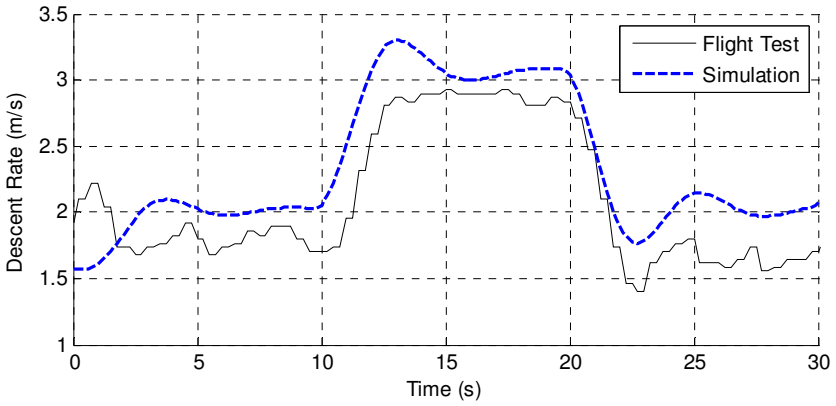

Figure 3.9: Descent Rate Response to Incidence Step

An especially important feature to capture in the simulation model is the difference in turn rate response created as the canopy incidence angle is changed. Figure 3.10 shows the steady state turn rate vs. differential brake deflection of the simulation model compared to simulation data at three different incidence angle settings.

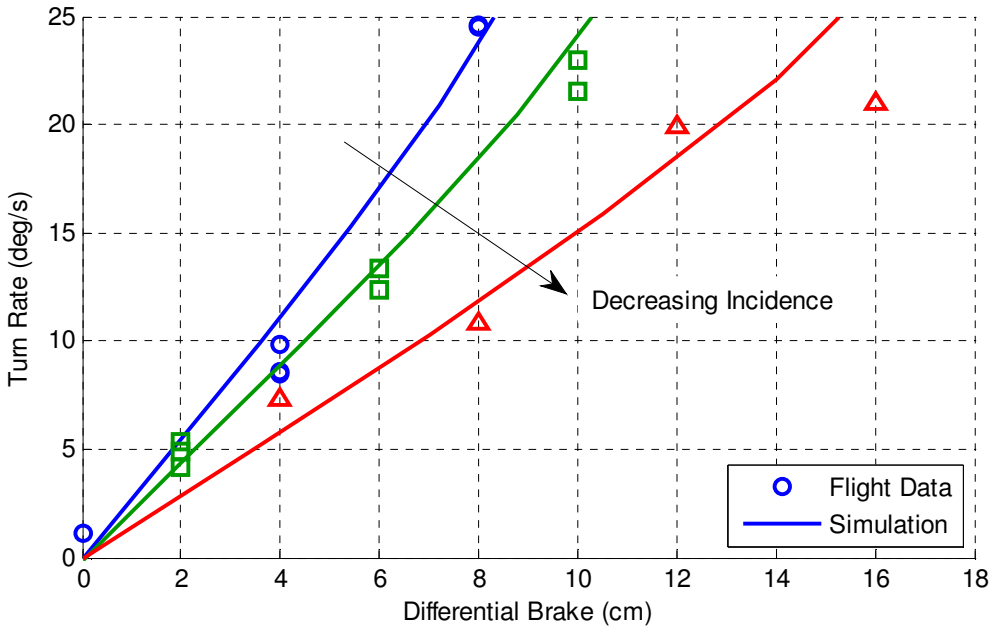

Figure 3.10: Turn Rate vs. Differential Brake and Incidence Angle

CHAPTER 4

GNC ALGORITHM FOR AUTONOMOUS LANDING

This section describes the basic guidance, navigation, and control (GNC) algorithm used for autonomous landings. The basic algorithm is not novel and shares many features with state of the art guided parafoils discussed in the literature [33-46].

A. Guidance

The guidance algorithm splits the flight into 4 main phases: initialization, loiter, final approach, and landing. A simple terminal guidance algorithm for autonomous airdrop systems is an implementation of the "T approach" [1].

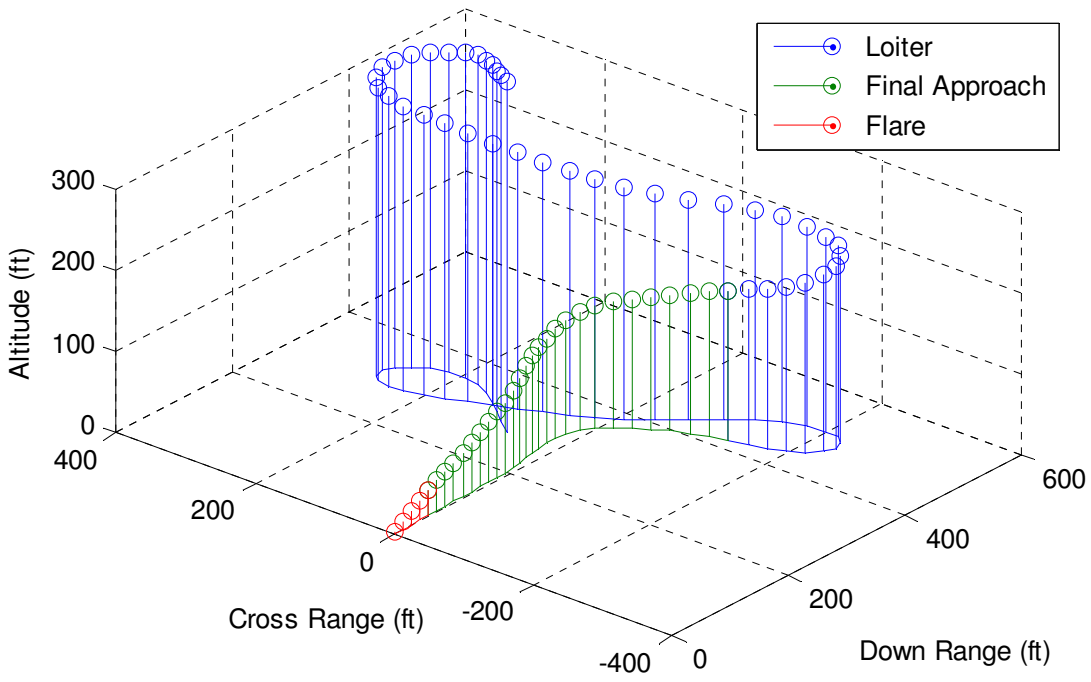

Figure 4.1: Typical Landing Trajectory

This is an approach commonly used by human sky divers and paragliders. The system loiters just downwind of the target by performing a series of figure eight turns. The turns are always made into the wind. This allows the system to enter the final approach trajectory quickly in case conditions change rapidly. Figure 4.1 shows a simulated flight trajectory starting near the end of the loitering phase.

1. Initialization

The purpose of this phase is to provide reasonable initial state estimates of wind and airspeed to the navigation algorithm. The simplest way to obtain these estimates is to hold a constant differential brake deflection long enough for the system to fly at least one complete circle. The length of the initialization phase and initial control setting are input as parameters to the GNC algorithm.

2. Loiter

The loiter phase consists of figure eight turns performed just downwind of the target. This is implemented by assigning homing targets at a specified distance downwind and a specified distance perpendicular to a line drawn straight down wind from the target. When the system reaches a specified radius from the target, the target is switched to the other side of the downwind line. The initial turn when the target is switched is always into the wind, resulting in a figure eight pattern. In very windy conditions it is desirable to prevent the system from flying too far downwind. This is accomplished by "tilting" the loiter targets into the wind so that the figure eight pattern begins close to the target and slowly drifts downwind to obtain the desired offset for final approach.

During loiter, the altitude required to reach the target from the current location is computed constantly. (Note: Heavily filtered state estimates of airspeed, descent rate, and wind components are used for guidance planning and are denoted with a subscript "F", while instantaneous state estimates are denoted with a subscript "k". Also, descent rate is constrained to a reasonable minimum value for all guidance calculations.) The time remaining in the flight is:

$$T = h_k / \dot{z}_F \tag{4.1}$$

The effective distance from the target accounting for the wind is:

$$d = \sqrt{(x_k + V_{WX,F} t)^2 + (y_k + V_{WY,F} t)^2} \tag{4.2}$$

The altitude required to cover this distance is determined from the current estimate of the glide ratio. Some additional altitude is required to make the turn to the target, which is assumed to occur at a constant nominal turn rate. The sum of the altitude required to reach the target is the sum of the altitude used to turn to the target and the altitude used to glide to the target.

$$T_{turn} = | \chi_0 - \tan_2^{-1}(-y,-x) | \dot{\chi}_{nom} \tag{4.3}$$

$$h_{req} = d \frac{\dot{z}}{V_0} + T_{turn} \dot{z} \tag{4.4}$$

The altitude margin is defined as the difference between the current altitude and the altitude required to reach the target. When the altitude margin falls below a specified value, the guidance algorithm switches from the loiter phase to the approach phase.

3. Approach

A two stage final approach is used where the system first tracks an offset target on its way to the desired impact point. This offset target is placed downwind of the desired impact point and the altitude of this offset target is set to lie just above the nominal glide path to the actual impact point. While homing to the offset target, the system computes the altitude margin for reaching the desired impact point. When the altitude margin for reaching the impact point reaches zero, the system begins homing to the actual target. Figure 4.2 shows some example approach trajectories demonstrating the logic of the two stage approach.

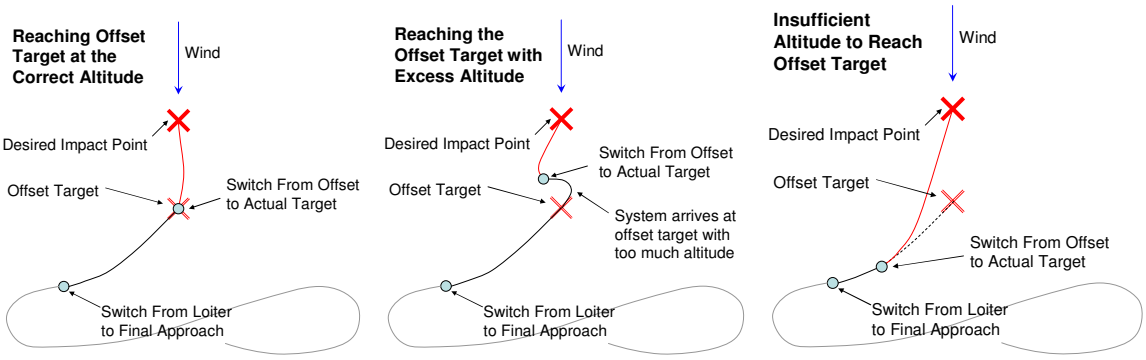

Figure 4.2: Two Stage Final Approach Examples

If the system reaches the offset target with the correct amount of altitude, it then flies to the actual target and lands into the wind. If the system reaches the offset target with excess altitude, it loiters over the offset target until the excess altitude is burned off. Finally, if the system runs out of altitude margin on the way to the offset target, the offset

target is abandoned and the system flies straight at the desired impact point. This allows the approach trajectory to adapt to changes in the wind during final approach. An alternative method is to periodically compute optimal final approach trajectories to track with a path following controller. A simulation study comparing the two approach strategies found that the landing accuracy using the two stage final approach strategy was the same as the landing accuracy with the optimal with significantly reduced computational cost.

4. Landing

The goal of the landing maneuver is to minimize the kinetic energy of the system just before impact. This is accomplished by first releasing the trailing edge brakes to zero deflection and setting the incidence angle to the maximum nose-up setting, then applying full symmetric brake at the maximum rate (flare). The initiation of the brake release and the flare occur at specified altitudes.

B. Navigation

The term navigation is used here to refer to the task of estimating the parafoil aircraft states from the available sensor data. Sensor data is assumed to be 3 dimensional position and the three components of inertial velocity obtained from a single, commercial GPS receiver and a barometric altimeter. State estimation is performed with an extended Kalman filter observer.

The horizontal and vertical position and velocity estimates are obtained from the measurements using a standard Kalman filter [82]. The equation for the predicted north component of position and velocity (x_P) based on a previous estimate (x), is:

$$\begin{Bmatrix} x_{P,k+1} \\ \dot{x}_{P,k+1} \end{Bmatrix} = \begin{bmatrix} 1 & \Delta t \\ 0 & 1 \end{bmatrix} \begin{Bmatrix} x_k \\ \dot{x}_k \end{Bmatrix} + \begin{Bmatrix} \delta x_k \\ \delta \dot{x}_k \end{Bmatrix} \tag{4.5}$$

The state update incorporating the current prediction (x_P) and measurement (x_M) is:

$$\begin{Bmatrix} x_{k+1} \\ \dot{x}_{k+1} \end{Bmatrix} = \begin{Bmatrix} x_{P,k+1} \\ \dot{x}_{P,k+1} \end{Bmatrix} + G \begin{Bmatrix} x_{M,k+1} - x_{P,k+1} \\ \dot{x}_{M,k+1} - \dot{x}_{P,k+1} \end{Bmatrix} \tag{4.6}$$

Where G is the Kalman filter gain matrix which is a constant matrix obtained offline by solution of the matrix equation:

$$\begin{aligned} P_n &= APA^T + Q \\ G &= P_n (P_n + R)^{-1} \\ P &= (I - G) P_n \end{aligned} \tag{4.7}$$

where Q and R are the process and measurement noise covariance matrices.

$$Q_X = \begin{bmatrix} 0 & 0 \\ 0 & q_{xd} \end{bmatrix}, R_X = \begin{bmatrix} \sigma_X^2 & 0 \\ 0 & \sigma_{VX}^2 \end{bmatrix} \tag{4.8}$$

The state update equations are the same for the north, east, and vertical components of position and velocity. The parameters used to define the process and measurement noise variance are given in the table below.

Table 4.1: Noise Parameters for Position and Velocity State Updates

	q_{xd} (m/s)^2	σ_X (m)	σ_{VX} (m/s)
North and East Pos. and Vel.	2	2	0.2
Vertical Pos. and Vel.	1	3	0.5

An extended Kalman filter [82] observer produces an estimate of the wind vector and system heading angle from GPS data by solving the vector diagram in Figure 4.3. The ground track velocity is measured with GPS. It was shown in the discussion of parafoil system identification that the resolution of this ground track vector into the airspeed V_0 and wind vector V_w is not unique. When performing system identification off-line, a series of vector diagrams at a variety of heading angles are solved simultaneously to obtain unique airspeed and wind estimates. To ensure a stable, real-time wind vector estimate, the wind vector estimate is gradually over a series of measurements and the airspeed is not estimated as a state in the observer. A model to compute airspeed as a function of the control inputs is either loaded into the flight computer beforehand or estimated in flight with the process described in the next section. Note that solution of the vector diagram does not directly yield an estimate of the parafoil heading angle ψ, but rather the azimuth angle χ_0. The two are related by the sideslip angle β, which is normally small for parafoil and payload aircraft.

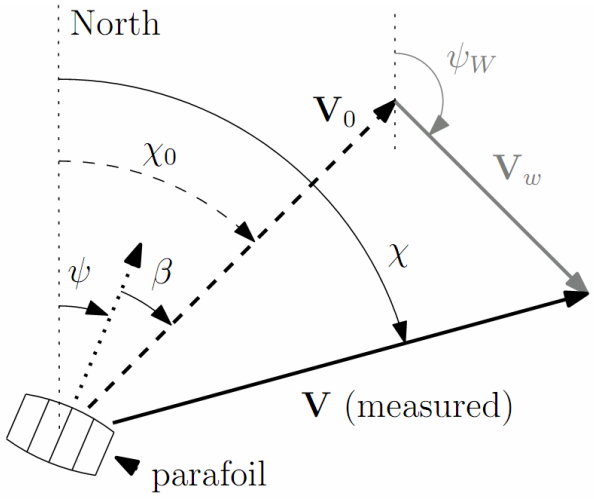

Figure 4.3: Decomposing Measured Velocity Vector

The wind vector and heading angle are defined as states in the observer. The state update equations defined by the vector geometry in Figure 4.3 are given in Table 4.2. These equations assume that the wind vector and heading rate are perturbed by a process noise vector consisting of independent perturbations.

Table 4.2: State Prediction Equations for Wind and Airspeed Estimator

States	$\mathbf{x}_{P,k+1}$	=	$\mathbf{f}_k$	$+ \mathbf{n}_k$
North Wind Component (ft/s)	$V_{WX\,k+1}$	=	$V_{WX\,k}$	$+ n_{VWX}$
East Wind Component (ft/s)	$V_{WY\,k+1}$	=	$V_{WY\,k}$	$+ n_{VWY}$
Heading (rad)	χ_{0k+1}	=	$\chi_{0k} + \dot{\chi}_{0k}\Delta t$	
Heading Rate (rad/s)	$\dot{\chi}_{0k+1}$	=	$\dot{\chi}_{0k}$	$+ n_{\dot{\chi}}$

Table 4.3: Measurement Update Equations for Wind and Airspeed Estimator

Measurement	$\mathbf{v}_k$	=	$\mathbf{g}_k$	$+ \mathbf{w}_k$
North GPS Velocity Component (ft/s)	$\dot{x}_k$	=	$V_0 \cos(\chi_{0k}) + V_{WX\,k}$	$+ n_{xd}$
East GPS Velocity Component (ft/s)	$\dot{y}_k$	=	$V_0 \sin(\chi_{0k}) + V_{WY\,k}$	$+ n_{yd}$

The state, covariance and Kalman filter gain updates are given in Eqs. (4.9) and (4.10).

$$\mathbf{x}_{k+1} = \mathbf{f}_k + G_k(\mathbf{v}_{k+1} - \mathbf{x}_{P,k+1}) \tag{4.9}$$

$$\begin{aligned} P_n &= AP_kA^T + Q \\ G_k &= P_nC_k^T(C_kP_nC_k^T + R)^{-1} \\ P_{k+1} &= (I - G_kC_k)P_n \end{aligned} \tag{4.10}$$

where:

$$A = \frac{\partial \mathbf{f}_k}{\partial \mathbf{x}_k} = \begin{bmatrix} 1 & 0 & 0 & 0 \\ 0 & 1 & 0 & 0 \\ 0 & 0 & 1 & \Delta t \\ 0 & 0 & 0 & 1 \end{bmatrix} \tag{4.11}$$

$$C_k = \frac{\partial \mathbf{g}_k}{\partial \mathbf{x}_k} = \begin{bmatrix} 1 & 0 & -V_0 \sin(\chi_{0k}) & 0 \\ 0 & 1 & V_0 \cos(\chi_{0k}) & 0 \end{bmatrix} \tag{4.12}$$

and the process and measurement noise covariance matrices are defined as:

$$Q = \begin{bmatrix} \delta V_W & 0 & 0 & 0 \\ 0 & \delta V_W & 0 & 0 \\ 0 & 0 & 0 & 0 \\ 0 & 0 & 0 & \delta\ddot{\chi} \end{bmatrix} \tag{4.13}$$

$$R = \begin{bmatrix} \sigma_V^2 & 0 \\ 0 & \sigma_V^2 \end{bmatrix} \tag{4.14}$$

The process and measurement noise parameters are given in the table below:

Table 4.4: Noise Parameters for Wind and Airspeed Estimator

Parameter	Value
δV_W	0.01 $(ft/s)^2$
$\delta\ddot{\chi}$	.02 $(rad/s)^2$
σ_V	2 (m/s)

C. Control

Lateral control is provided by a model predictive controller tracking a commanded heading angle. The use of an MPC controller for lateral control of a parafoil and payload system is not new, and it is not claimed that this controller provides substantially improved performance over the typical PID controller used for guided airdrop systems. The main benefit of the MPC controller in this case is the simplicity of selecting the control gains.

The controller uses an internal model of the turn rate dynamics to determine an optimal set of control inputs given a set of heading commands. The goal of the model predictive controller is to determine a vector of control inputs that will minimize the error between the predicted output vector and a commanded output vector over a finite time horizon with a minimum amount of control effort. This control strategy is depicted in Figure 4.4.

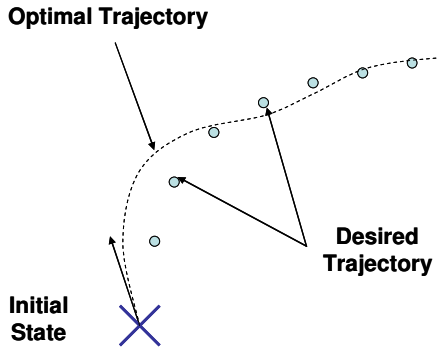

Figure 4.4: Model Predictive Control Strategy

The controller assumes the turn rate response is related to the differential brake deflection by the first order linear model specified by Eqs. (4.15-4.17), where τ is the turn rate time constant and b is the control sensitivity.

$$x_{k+1} = Ax_k + Bu_k, \; y_k = Cx_k \tag{4.15}$$

$$x_k = \begin{Bmatrix} \chi_k \\ \dot{\chi}_k \end{Bmatrix},\ u_k = \delta_A,\ y_k = \chi_k \tag{4.16}$$

$$A = \begin{bmatrix} 1 & \Delta t \\ 0 & 1 - \Delta t / \tau \end{bmatrix}, B = \begin{bmatrix} 0 \\ b\Delta t / \tau \end{bmatrix}, C = [1 \quad 0] \tag{4.17}$$

The A, B, and C matrices describing the internal model are used to generate a commanded brake differential, δ_a, given a current state estimate from navigation, x_k, and a vector of heading commands, Y_c, from guidance.

$$\delta_{A,C} = k_1 (Y_c - K_{CA} x_k) \tag{4.18}$$

The term k_1 refers to the first row of the gain matrix specified in Eq. (4.19)

$$k = (K_{CAB}{}^T K_{CAB} + R)^{-1} K_{CAB}{}^T \tag{4.19}$$

$$K_{CA} = \begin{bmatrix} CA \\ CA^2 \\ \vdots \\ CA^{Hp-1} \end{bmatrix} \tag{4.20}$$

$$K_{CAB} = \begin{bmatrix} CB & 0 & 0 & \cdots & 0 \\ CAB & CB & 0 & \cdots & 0 \\ CA^2B & CAB & CB & \cdots & 0 \\ \vdots & \vdots & \vdots & \ddots & \vdots \\ CA^{Hp-1}B & \cdots & CA^2B & CAB & CB \end{bmatrix} \tag{4.21}$$

Parafoil and payload aircraft typically exhibit a random turn bias so that zero differential brake input usually results in a non-zero turn rate. The internal model used by the controller is used to estimate this bias over time with a heavily damped filter:

$$\delta_{A,BIAS} = \delta_{A,BIAS} + K_I(\dot{\chi}_C - \dot{\chi})/b \tag{4.22}$$

This bias estimate is subtracted from the differential brake commands from the model predictive controller:

$$\delta_A = \delta_{A,C} + \delta_{A,BIAS} \tag{4.23}$$

D. Example Simulated Flight

A simulated flight trajectory from an altitude of 250 meters is shown below. The average wind speed is 4 m/s from the North and the standard deviation of the vertical wind for the Dryden turbulence model was set to 0.6 m/s.

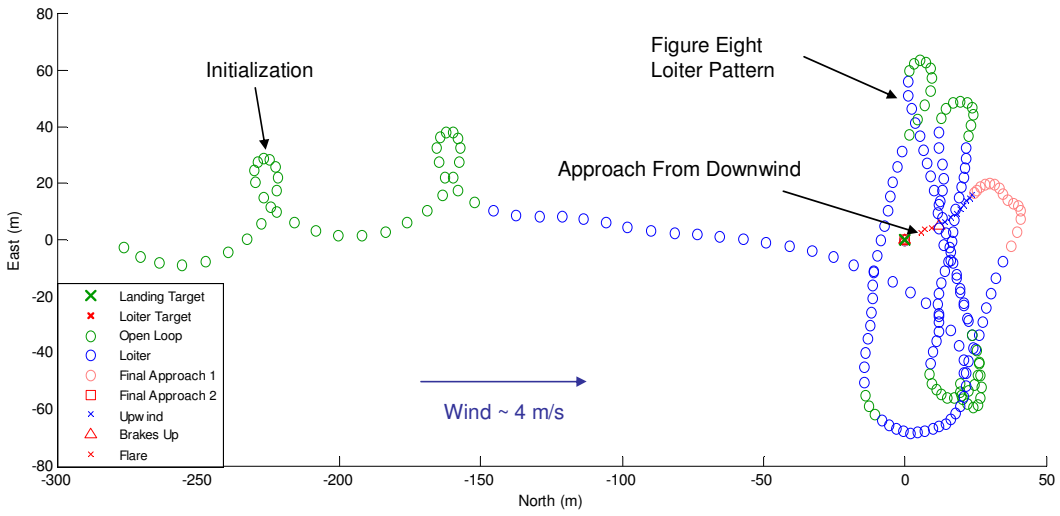

Figure 4.5: Example Simulated Autonomous Flight

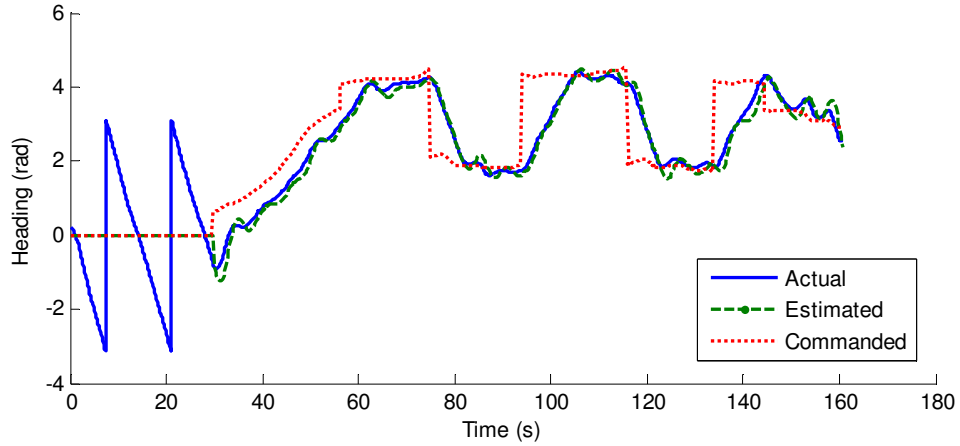

Figure 4.6: Heading Angle Estimation and Tracking

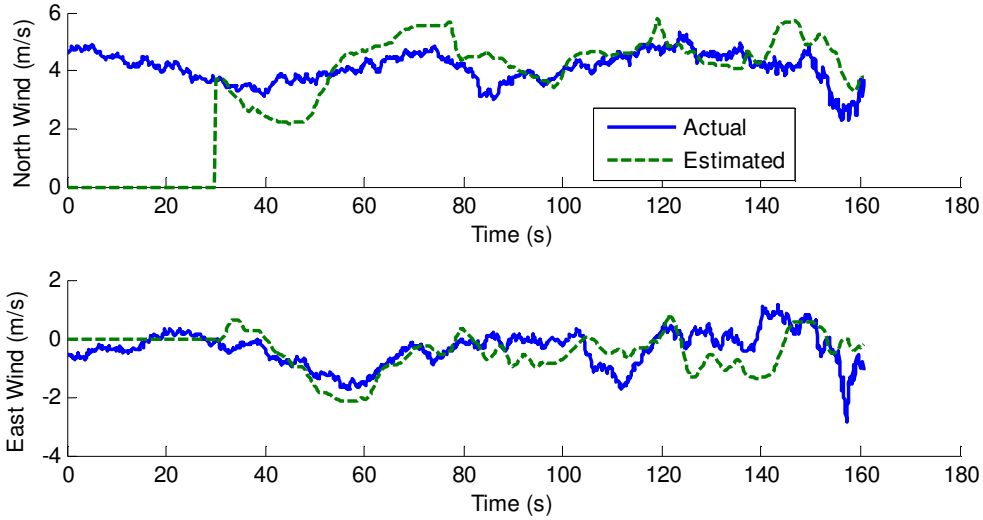

Figure 4.7: Wind Estimation in Autonomous Simulation

CHAPTER 5

PARAFOIL INCIDENCE ANGLE CONTROL AUTHORITY

While the main goal of this work is the demonstration of autonomous, adaptive glide slope control of a parafoil and payload aircraft in flight, a significant amount of preliminary work had to be performed, both in simulation and flight test, before any autonomous flights could be attempted. The first main contribution of this preliminary work is an extensive set system identification flight tests performed to gain insight into variable canopy incidence angle as a glide slope control mechanism for parafoils. This flight test program focused on studying the interaction of incidence angle with the traditional control mechanism of trailing edge brake deflection and also on determining what sets the limits of glide slope control with variable incidence angle. The second contribution of the preliminary work is an in-depth study in simulation of the benefits of in-flight system identification to determine how reliably information about the flight dynamics of a parafoil and payload aircraft can be obtained in-flight in different conditions.

A. Glide Slope Control with Variable Incidence Angle

This section presents an examination of the aspects of glide slope control with variable incidence angle. The definitions and sign conventions of canopy incidence angle and symmetric brake deflection used throughout the current work are shown in Figure 5.1. A negative incidence angle indicates that the leading edge of the canopy is pulled

down from horizontal, and a positive brake deflection indicates that the trailing edge is pulled down from the chord line. This means that a change in incidence angle with constant brake deflection is equivalent to a pure rotation of the canopy.

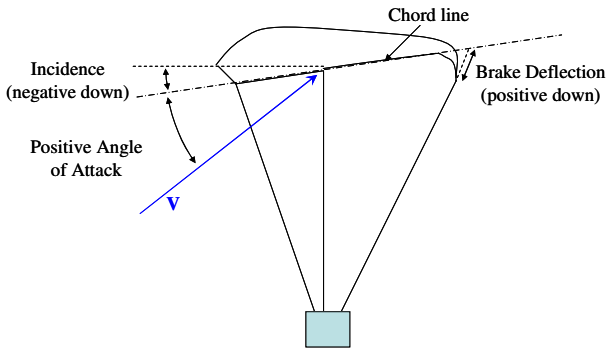

Figure 5.1: Sign Conventions for Incidence Angle and Brake Deflection

1. Introduction to Glide Slope Control with Variable Incidence Angle

The system developed by Slegers, Beyer and Costello to demonstrate glide slope control through variable incidence angle is shown in Figure 5.2. In addition to the standard control mechanism of symmetric and asymmetric trailing edge deflection, the canopy rigging can be adjusted in flight to allow longitudinal rotation of the entire canopy about the aerodynamic center to directly control the trim angle of attack in flight. Flight test results are shown in Figure 5.3, demonstrating that the incidence angle variation can produce a substantial change in the glide angle of the parafoil.

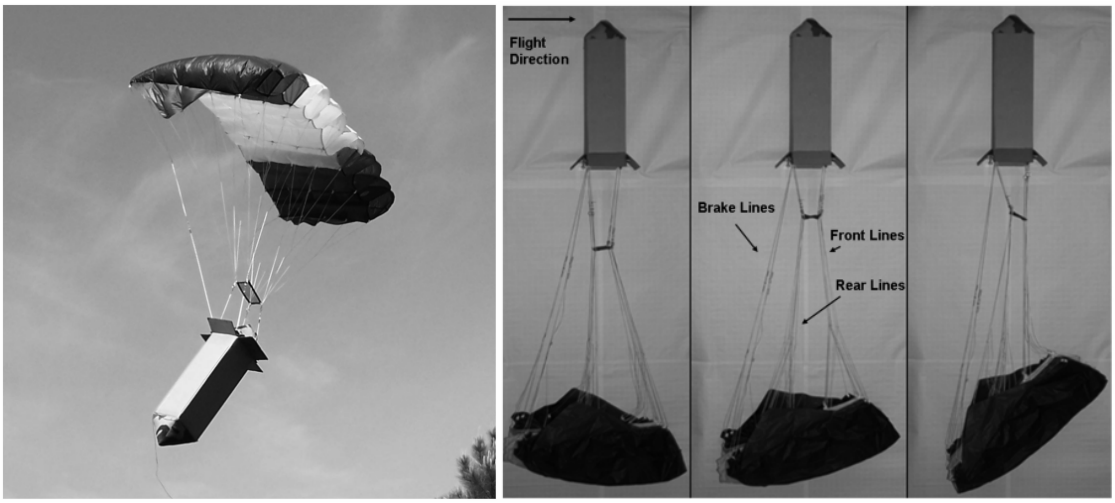

Figure 5.2: Variable Incidence Angle Tested by Slegers, Beyer, and Costello [12]

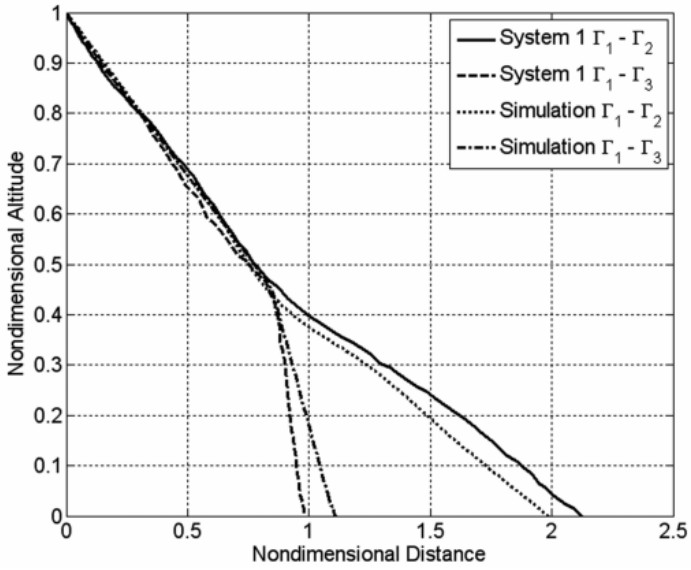

Figure 5.3: Flight Test Results of Variable Incidence System [12]

The effect of changing the incidence angle on a parafoil and payload system is very similar to the effect of the elevator on a fixed wing aircraft in glide. Just as the elevator alters the trim angle of attack of the wing, altering the incidence angle produces a change in the trim angle of attack of the parafoil canopy. Assuming that the pitch angle of the

system is constant (location of the center of pressure of the canopy is constant), the sum of the incidence angle and the angle of attack will be the flight path angle. This means that there is a unique curve of flight path angle vs. angle of attack for a given setting of incidence angle. Similarly, there is a unique lift to drag ratio (glide slope) vs. angle of attack curve determined by the aerodynamic characteristics of a given canopy. The intersection of the flight path angle curve for a given incidence angle setting and the glide slope curve for a given canopy represents the trimmed flight condition for that combination of incidence angle and canopy. This concept is shown in Figure 5.4 for two notional canopies.

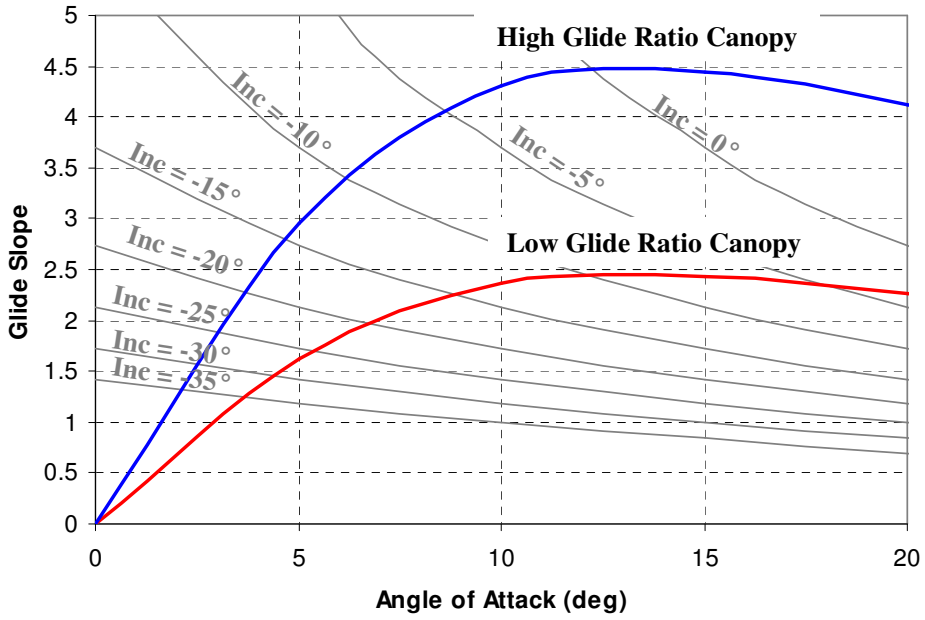

Figure 5.4: Conceptual Plot of Canopy Trim Conditions

The first canopy has a peak glide ratio of 2.5, while the second canopy has a peak glide ratio of 4.5. This plot provides some important insight into the use of incidence

angle as a glide slope control mechanism. In particular, the glide slope range is increased for a more efficient (higher glide ratio) canopy, the sensitivity of glide slope to incidence angle is highest just below the peak glide ratio trim point, and the sensitivity of glide slope to incidence angle is dramatically reduced at low glide ratios. Incidence angle has a more direct influence on flight path angle than glide slope, so it is important to keep in mind the nonlinear relationship between glide slope and flight path angle. As shown in Figure 5.5, a reduction in glide slope from 3 to 2 represents an 8 degree change in flight path angle, while a reduction in glide slope from 2 to 1 represents an 18 degree change in flight path angle. For this simple reason, it is more efficient to apply variable incidence angle as a glide slope control mechanism on canopies with high glide ratios.

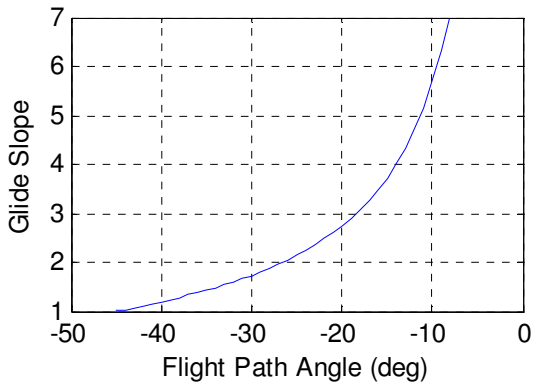

Figure 5.5: Relationship of Glide Slope to Flight Path Angle

Figure 5.6 shows glide ratio plotted vs. aspect ratio for a variety of parafoil canopies [43,72, 83, 84. There are two distinct groups in this plot, the lower aspect ratio/lower glide ratio group is composed of airdrop systems, and the higher aspect ratio/higher glide ratio group is composed of paragliding canopies designed for soaring flight. The current work focuses on canopies at the higher end of the spectrum of airdrop systems.

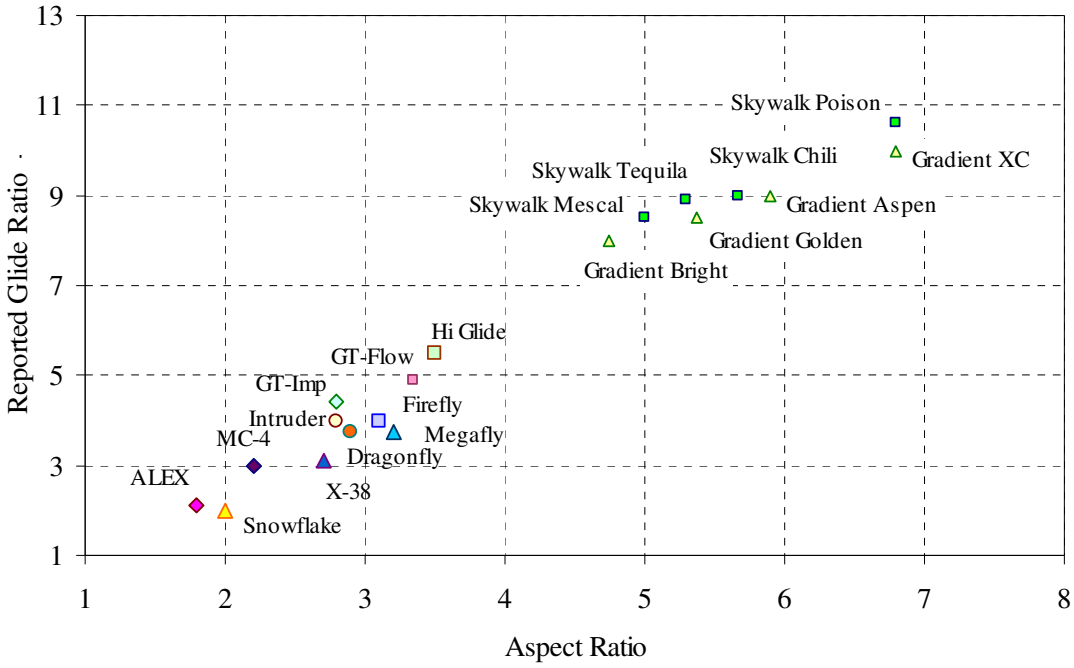

Figure 5.6: Reported Glide Ratio vs. Aspect Ratio for Several Parafoil Systems

2. Description of Flight Test Hardware

An experimental flight test program was conducted to explore the ability of in-flight incidence angle changes to control glide slope. A self-powered parafoil and payload system was developed specifically for the purpose of exploring parafoil glide slope control concepts. The system uses a small gas motor. Control is achieved with the use of three winch servos. Two winch servos are used to control the left and right brakes independently, and a single winch servo is used to control canopy incidence angle. The payload contains a sensor suite including a GPS receiver and barometric altimeter as well as a flight computer for autonomous control input and data logging. The combined sensor suite/flight computer unit was developed by Slegers [48], and has been flown extensively

on the Snowflake autonomous airdrop system. The self-powered payload is shown in Figure 5.7.

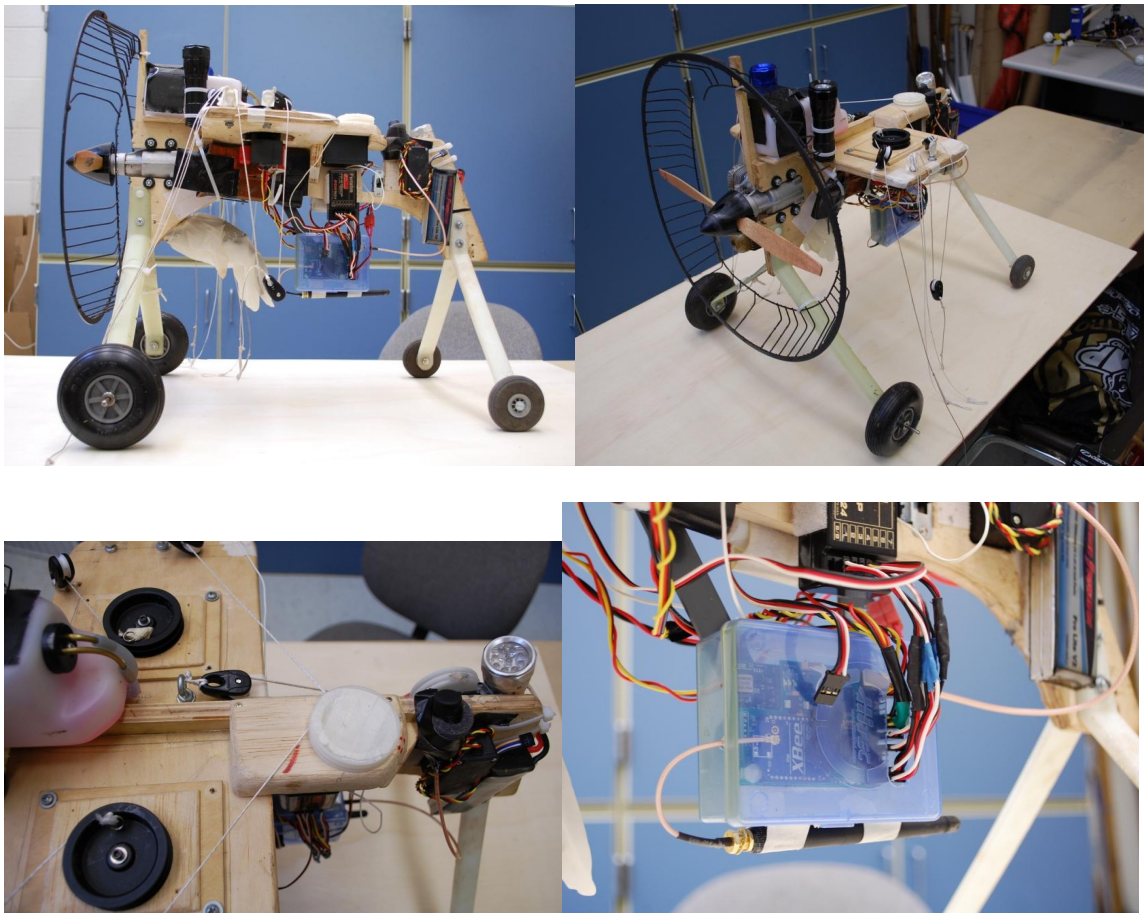

Figure 5.7: Flight Test Vehicle (Bottom Left: Winch Servos, Bottom Right: Flight Computer)

Two canopies with aspect ratios of approximately 2.8 and 3.4 were tested. The canopy planforms and line attachment points are shown in Figure 5.8 and Figure 5.9. The canopy attachment points were split into four groups. “A” lines all run to the incidence angle control winch, “B” lines and tip lines run to fixed attachment points on the payload, and brake lines run to the left and right brake winches.

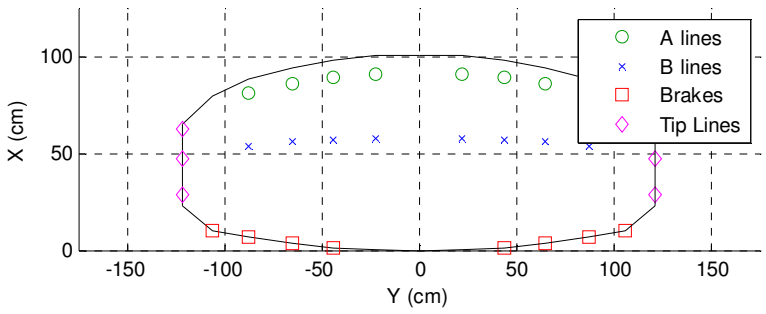

Figure 5.8: Low AR Canopy Planform Showing Attachment Points

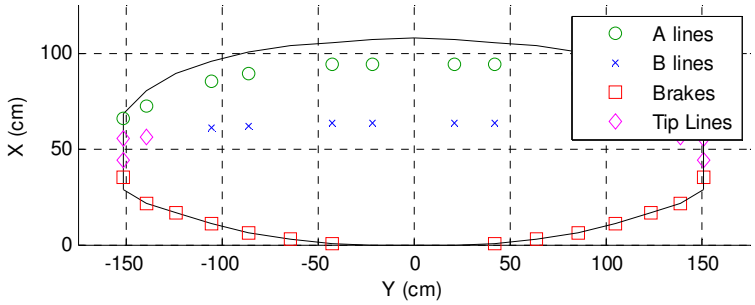

Figure 5.9: Medium AR Canopy Planform Showing Attachment Points

By trimming the A lines in concert with the brakes, a pure longitudinal rotation of the canopy to different incidence angles can be achieved as shown in Figure 5.10. This provides direct control over the trim angle of attack, allowing the full range of the canopy's lift to drag ratio to be utilized in flight.

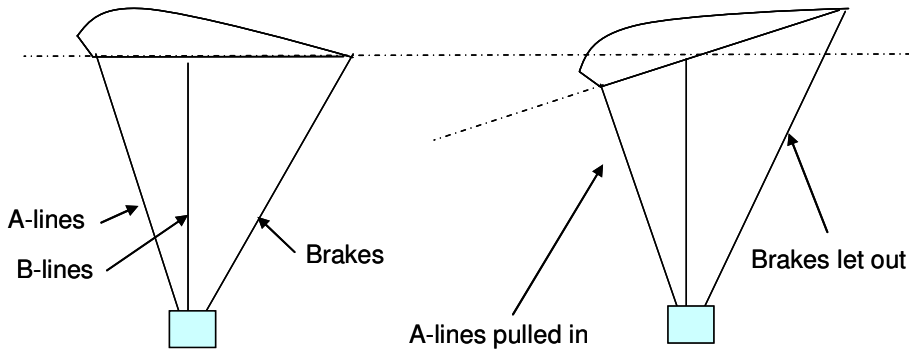

Figure 5.10: Incidence Angle Control

The canopies are designed to be rigged in a style more typical of paragliders than airdrop systems. The center 60% of the canopy span is a circular arc with a radius equal to 70% of the canopy span. The outboard sections of the canopy are transitioned from this circular arc to be tangent to the vertical at the wingtips. The low and medium aspect ratio canopies were rigged to generate this same shape. The resulting rigging geometries are shown in Figure 5.11 and Figure 5.12. The photo depicting the actual geometry of the medium aspect ratio canopy in flight is shown in Figure 5.13.

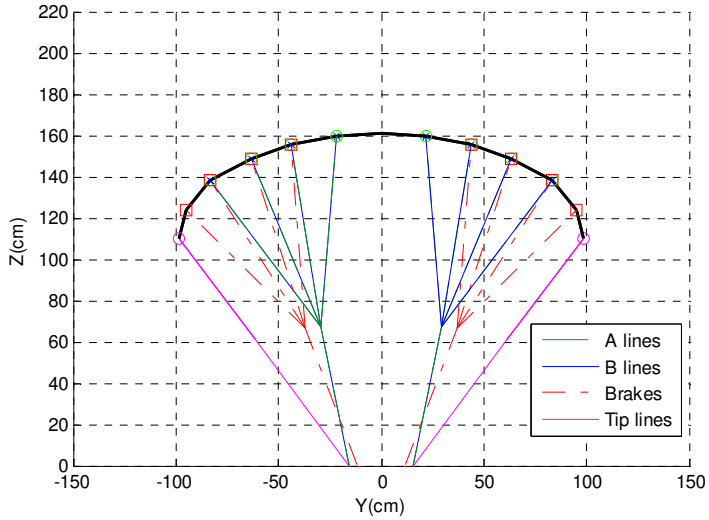

Figure 5.11: Low AR Canopy Rigging Geometry

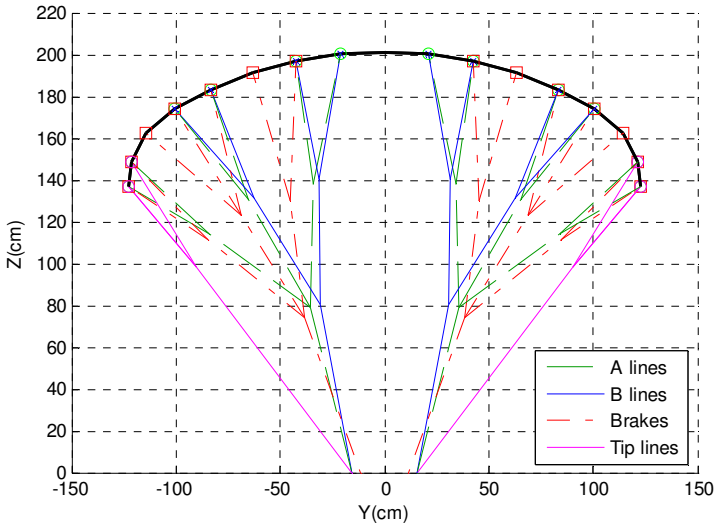

Figure 5.12: Medium AR Canopy Rigging Geometry

Figure 5.13: Medium Aspect Ratio Canopy in Flight

The canopy geometry, rigging geometry and mass properties of the low and medium aspect ratio test systems are given in Table 5.1. The medium aspect ratio canopy is slightly larger than the low aspect ratio canopy, so ballast was added when flying the medium aspect ratio canopy to maintain a similar wing loading. The ballast consisted of lead plates mounted to the estimated location of the center of gravity of the payload.

Table 5.1: Canopy, Rigging, and Payload Parameters for Flight Test Vehicle

	Low AR	Mid AR
Aspect Ratio	2.79	3.35
Area	2.1 m^2 (22.6 ft^2)	2.72 m^2 (29.3 ft^2)
Span	2.4 m (7.9 ft)	3.0 m (9.8 ft)
Mean Chord	0.88 m (2.9 ft)	0.91 m (3.0 ft)
Canopy Arc Radius	1.68 m (5.5 ft)	2.1 m (6.9 ft)
Projected Aspect Ratio	2.01	2.39
Projected Area	1.7 m^2 (18.3 ft^2)	2.23 m^2 (24.0 ft^2)
Total rigging line length	26 m (84 ft)	57 m (187 ft)
Mass (Weight)	3.7 kg (8.1 lb)	4.72 kg (10.4 lb)
Wing Loading	1.76 kg/m^2 (0.36 lb/ft^2)	1.74 m^2 (0.35 lb/ft^2)
Mass Ratio	1.01	0.88

Figure 5.14: Comparison of Low and Medium Aspect Ratio Canopies in Flight

3. Flight Test Procedure and Data Reduction

The flight tests were focused on obtaining steady state values of airspeed and glide slope as a function of incidence angle and brake deflection. The flight test procedure begins by climbing under power up to test altitude (normally 1500 ft AGL). Once the testing altitude is reached, power to the motor is cut and the incidence angle and symmetric brake level are set to preprogrammed settings. The data logger is switched on and GPS and barometric altimeter data are recorded for approximately 20 seconds of gliding flight. The system is then sent back up to test altitude to repeat the procedure for the next control setting. For each setting of incidence angle and symmetric brake, a small amount of asymmetric brake is applied to produce a noticeable turn rate (normally 5-15 deg/s) to expose the wind. If a noticeable turn rate could not be achieved with less than 2 cm of brake differential, then the constant control segment was interrupted after approximately 10 seconds, the pilot took control and turned the system manually through approximately 180 degrees, and the constant control segment was continued for roughly another 10 seconds on the new heading angle.

Estimates of the atmospheric wind and forward airspeed were generated based on the vector diagram in Figure 5.15. The airspeed and wind vector are assumed constant for each segment of the flight where a constant control deflection is held. The airspeed and wind vector are estimated simultaneously for each constant control segment using an optimizer to minimize the difference between the measured ground track velocity ($\boldsymbol{V}_G$) and the estimated ground track velocity (computed as the sum of the estimated airspeed and wind vectors). This process works well when each constant control segment covers a

large change in azimuth to expose the wind (e.g., if a control input is held long enough to fly a complete circle, the airspeed is just the average speed measured over the circle and the wind vector is determined from the drift of the circle). The estimation process breaks down if a constant control segment does not contain enough azimuthal variation (e.g., if the vehicle flies in a straight line during the constant control segment it is impossible to extract separate estimates of the airspeed and wind vector). This is handled by appending a penalty to the optimization cost function proportional to the difference in the estimated wind vector between concurrent flight segments. In other words, if there is no unique airspeed and wind vector combination that can be extracted from a given flight segment then the optimizer will set the wind vector to match adjacent flight segments.

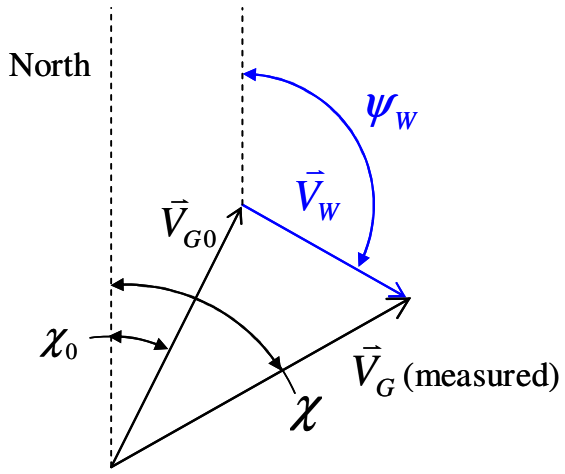

Figure 5.15: Decomposition of Ground Speed Vector

Figure 5.16 shows a sample GPS ground track for a constant control flight segment. Notice the gentle turn rate and the drift of the system over ground due to wind. Figure

5.17 shows the measured ground speed, the estimated airspeed, and the ground speed reconstructed from the airspeed and wind estimates. Figure 5.18 shows the descent rate derived from the barometric altimeter reading during the flight segment. The descent rate estimate is obtained as the median of the measured descent rate.

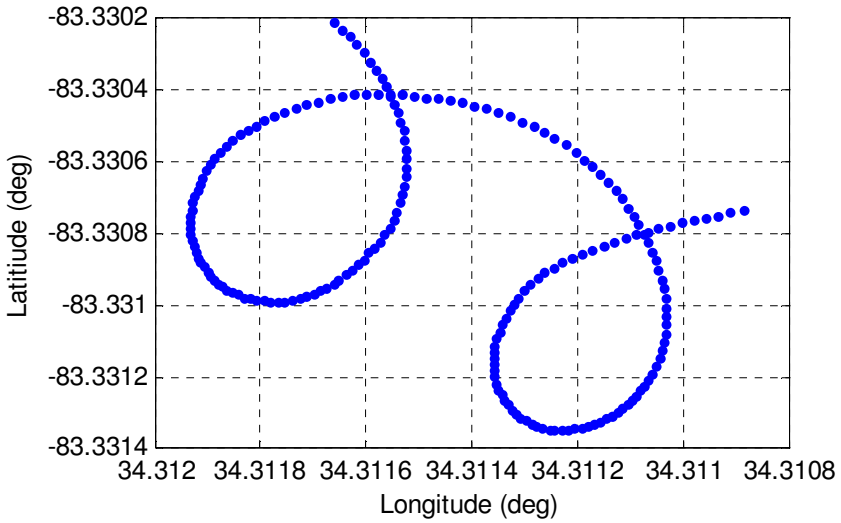

Figure 5.16: GPS Track for Constant Control Segment

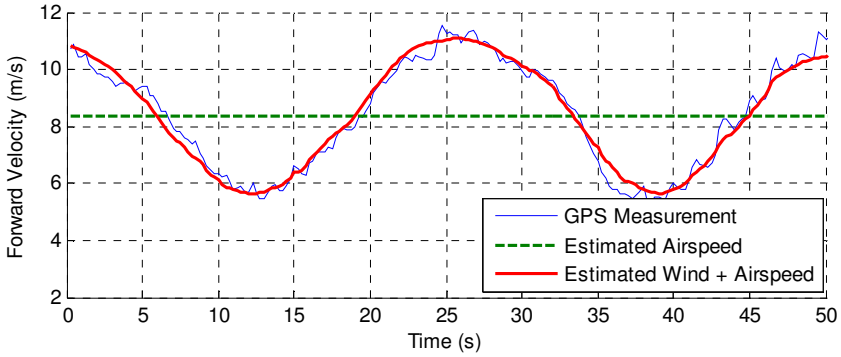

Figure 5.17: Extracting Forward Airspeed from GPS Groundspeed

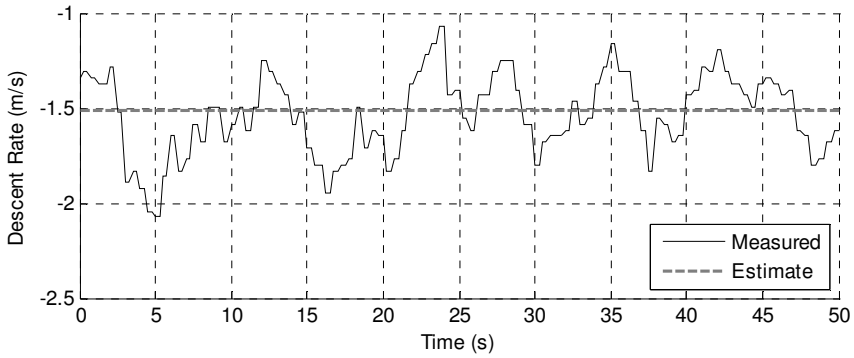

Figure 5.18: Descent Rate Estimate from Constant Control Segment

Each segment of constant control gliding flight results in a single data point of forward speed, descent rate, and turn rate for a particular combination of incidence angle and symmetric brake. These speeds are converted into lift and drag coefficients according to Figure 5.19 and Eqs. (2-1) to (2-3).

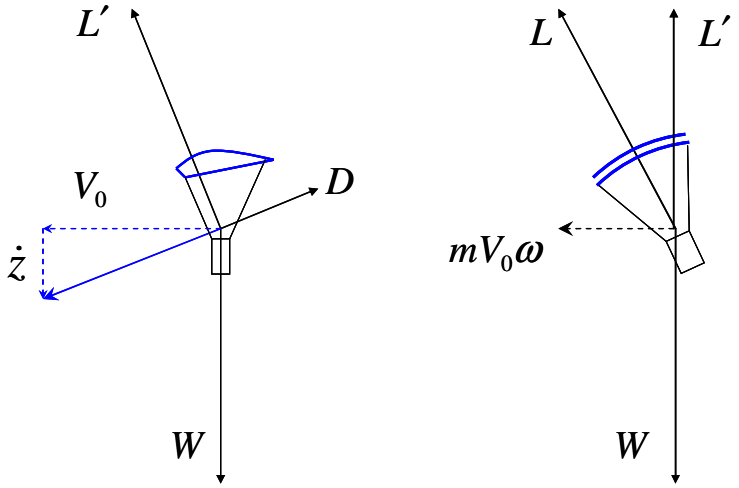

Figure 5.19: Estimating Lift and Drag from Forward Speed, Descent Rate, and Turn Rate

$$1/\tan\theta = V_0/\dot{z} = L/D \tag{5.1}$$

$$L' = W\cos\theta \tag{5.2}$$

$$L = \sqrt{L'^2 + (mV_0\omega)^2} \tag{5.3}$$

The variation in canopy incidence angle produces a change in angle of attack. The angle of attack can be approximated as the difference between the flight path angle and the incidence angle. This is an approximation because the pitch angle of the entire system is neglected; however, the pitch angle variation appears to be quite small. The lift and drag coefficients are assumed to vary with angle of attack based on Eqs. 4 and 5. Using the lift, drag, and angle of attack estimates extracted from fight test data, the aerodynamic parameters in these equations are estimated using linear regression. Finally, the definition of symmetric brake used in the presentation of the results is given in Eq. 6, where δ_R and δ_L are right left brake deflections, respectively, and *c* is the mean canopy chord.

$$C_L = C_{L0} + C_{LA}\alpha + C_{LA3}\alpha^3 \tag{5.4}$$

$$C_D = C_{D0} + C_{DA2}\alpha^2 \tag{5.5}$$

$$\delta_B = \frac{(\delta_R + \delta_L)}{2\mathrm{c}} \tag{5.6}$$

4. Results

a) Comparison of Low and Medium Aspect Ratio Canopies

The low and medium aspect ratio canopies were flown at varying incidence angles with zero symmetric brake. In other words, the canopies were rotated through a variety of incidence angles with the brakes trimmed to keep a flat trailing edge. The extracted lift and drag coefficient vs. angle of attack behaviors for the low and medium aspect ratio canopies are shown in Figure 5.20 and the identified aerodynamic parameters are shown in Table 5.2. As expected, the lift curve slope for the medium aspect ratio canopy is higher than the low aspect ratio canopy. However, the medium aspect ratio canopy appears to have a higher profile drag coefficient than the low aspect ratio canopy. This may be due to the increased complexity of the rigging for the medium aspect ratio canopy. Referring to Table 5.1, the reference area of the medium aspect ratio canopy is only 30% larger than the low aspect ratio canopy, but there is 120% more rigging line (and line drag) for the medium aspect ratio canopy.

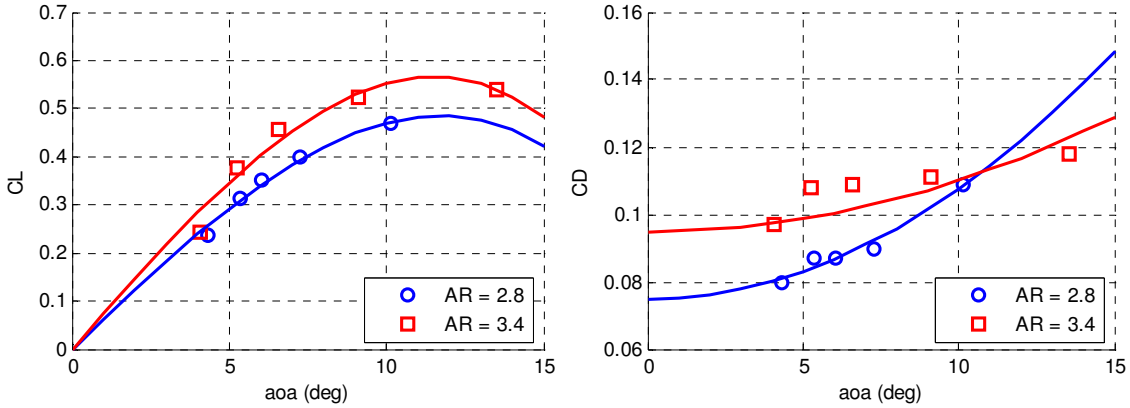

Figure 5.20: Lift and Drag Coefficient vs. Angle of Attack for Low and Medium Aspect Ratio Canopies

Table 5.2: Identified Lift and Drag Parameters with Zero Brake Deflection

Parameter	AR = 2.8	AR = 3.4
C_{L0}	0	0
C_{LA}	3.56	4.23
C_{LA3}	-28	-35
C_{D0}	0.074	0.095
C_{DA2}	1.12	0.496

The glide slope control achieved by varying incidence angle for these two canopies is shown in Figure 5.21. This plot shows that dramatic and effective glide slope control can be achieved by varying the canopy incidence angle. The low aspect ratio canopy has a peak glide slope of 4.4 and the medium aspect ratio canopy has a peak glide slope of 4.9. The lower limit of glide ratio for the canopies is not well established. There is a minimum angle of attack required to keep the canopies inflated, so testing near the lower limit of glide ratio risks a severe frontal collapse of the canopy.

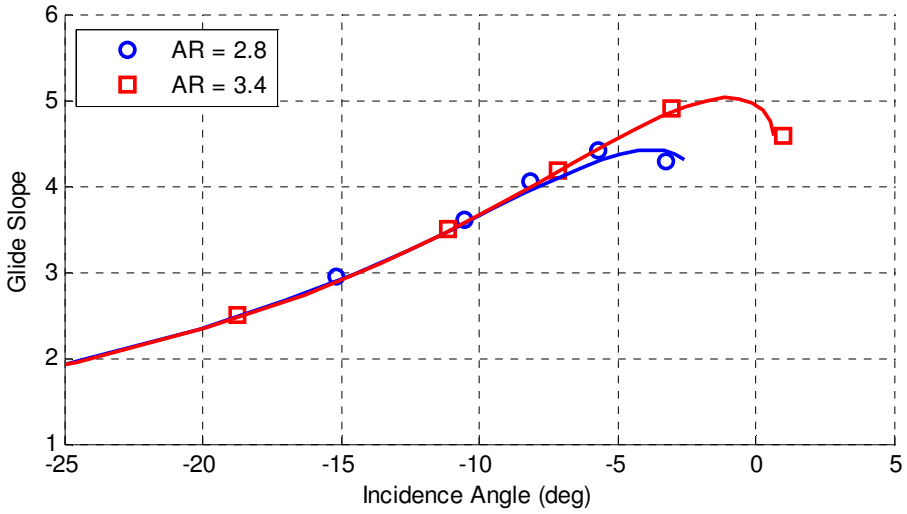

Figure 5.21: Glide Slope vs. Incidence Angle for Low and Medium Aspect Ratio Canopies

b) Interaction of Incidence Angle and Symmetric Brake

Flight tests were conducted for the low aspect ratio canopy at three levels of symmetric brake. The extracted lift and drag vs. angle of attack behavior is shown in Figure 5.22 and the identified aerodynamic parameters are given in Table 5.3. The variable incidence angle provides insight into the effect of symmetric braking that is not normally available from parafoil flight tests. The effect of symmetric brake is typically modeled as producing an increment in both lift and drag. It appears that in addition to this incremental effect, the symmetric brakes also increase the slopes of the lift and drag curves.

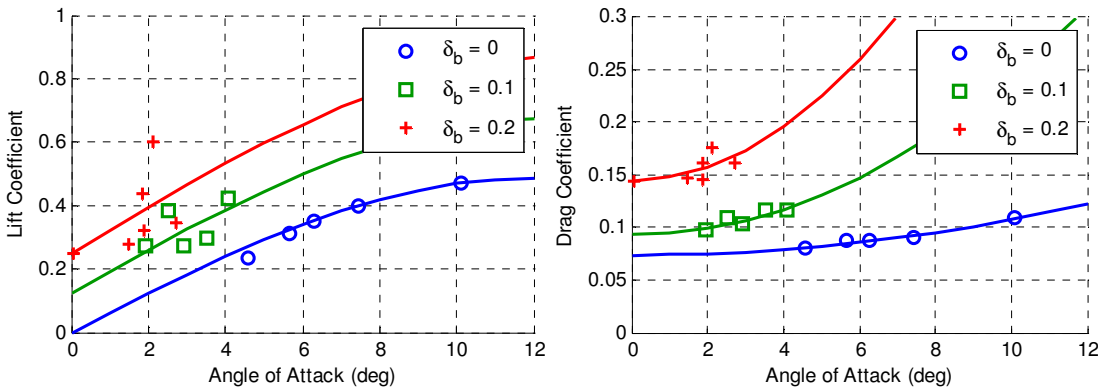

Figure 5.22: Lift and Drag Behavior vs. Angle of Attack and Symmetric Brake for Low Aspect Ratio Canopy

Table 5.3: Identified Lift and Drag Characteristics for Low Aspect Ratio Canopy

Parameter	$\delta_B = 0$	$\delta_B = 0.1$	$\delta_B = 0.2$
C_{L0}	0	0.125	0.251
C_{LA}	3.56	3.87	4.19
C_{LA3}	-28	-28	-28
C_{D0}	0.074	0.103	0.155
C_{DA2}	1.12	2.09	3.52

The effect of incidence angle on glide slope at the three symmetric brake levels is shown in Figure 5.23. Symmetric braking produces only a modest effect on glide slope. This is consistent with typical airdrop systems in that little change in glide slope is normally achieved with symmetric braking until the system nears stall.

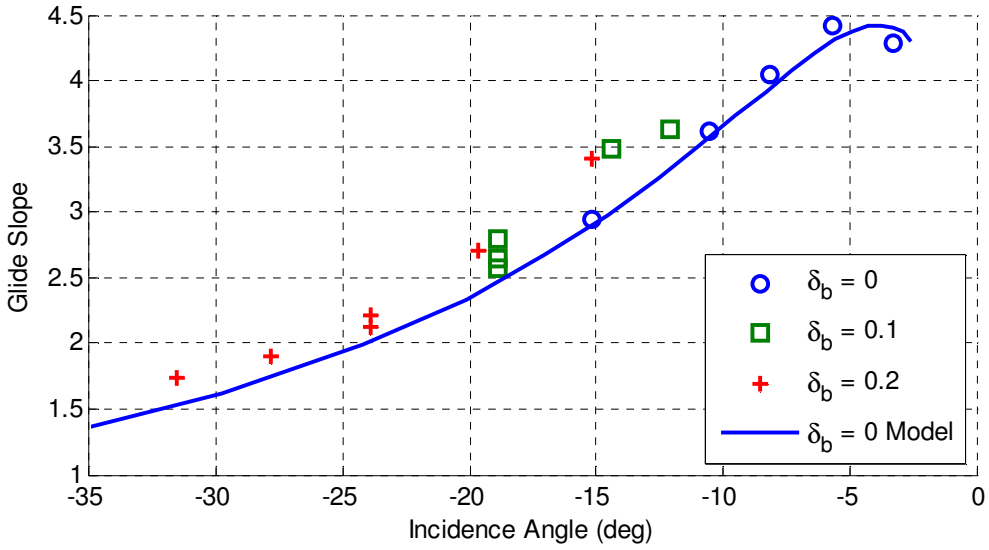

Figure 5.23: Glide Slope vs. Incidence for Low Aspect Ratio Canopy with Varying Symmetric Brake

Figure 5.24 shows the effect of incidence angle and symmetric brake on airspeed. This plot shows that incidence angle produces a dramatic effect on airspeed as well as glide slope. Though symmetric braking is not effective in controlling glide slope, it is quite effective in controlling airspeed. The relationship between incidence angle and symmetric brake produces the envelope of possible combinations of airspeed and glide slope shown in Figure 5.25. This is very interesting from a guidance and control perspective because it means that glide slope and airspeed can be controlled independently (within the constraints of the envelope) by modulating incidence angle and symmetric brake together.

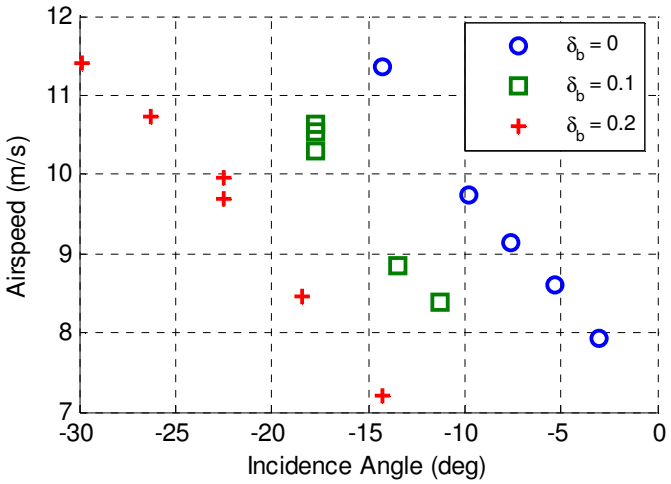

Figure 5.24: Airspeed vs. Incidence Angle for Low Aspect Ratio Canopy

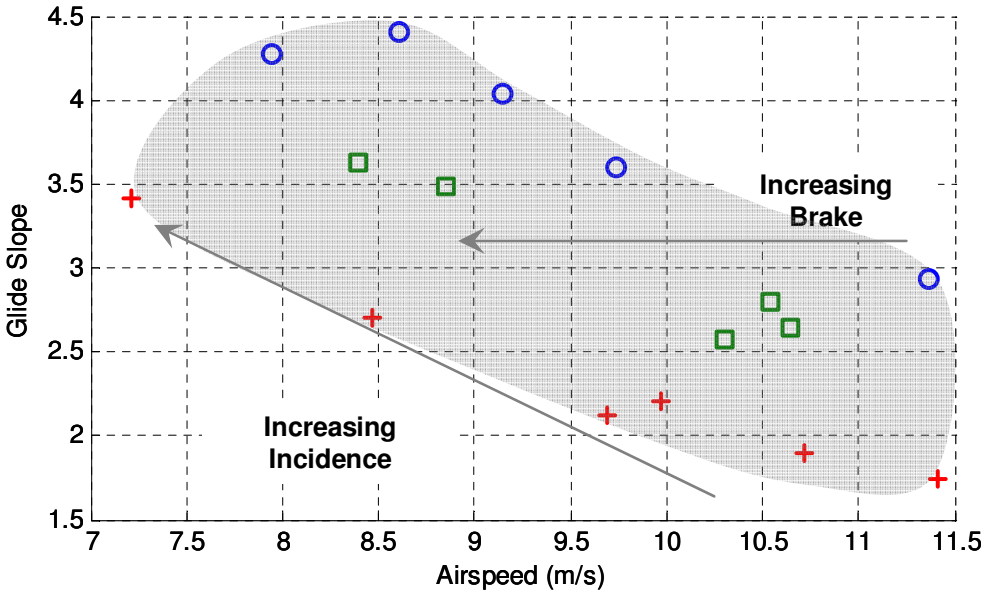

Figure 5.25: Glide Slope and Airspeed Envelope for Low Aspect Ratio Canopy

c) Dynamic Response to Incidence Angle Change

The medium aspect ratio canopy was given a large increase in incidence angle at zero symmetric brake. Figure 5.26 shows the estimated incidence angle winch response and Figure 5.27 shows the dynamic response of the system to this control input. An oscillation is excited where speed and glide ratio are exchanged in the manner of a Phugoid mode. While the incidence angle winch servo is able to reach the commanded incidence in roughly 3 seconds, it takes approximately 15 seconds for this oscillation to die down.

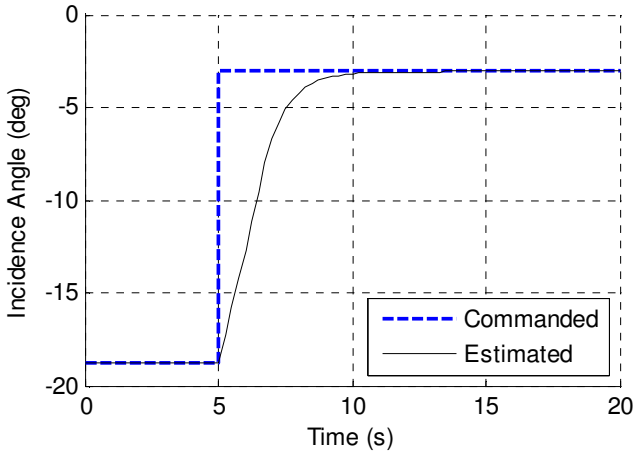

Figure 5.26: Dynamic Response of Medium Aspect Ratio Canopy to Large Increase in Incidence Angle

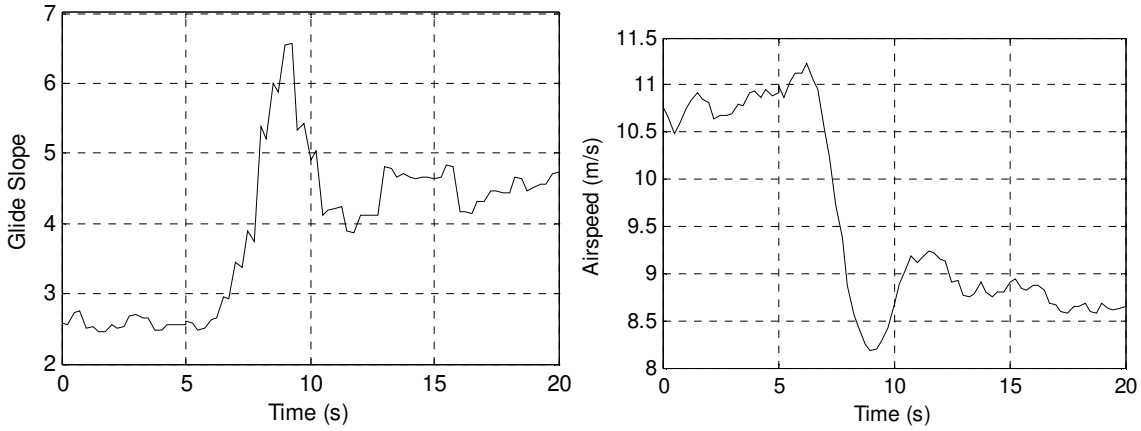

Figure 5.27: Dynamic Response of Medium Aspect Ratio Canopy to Large Increase in Incidence Angle

5. Glide Slope Over Ground

Variation of the canopy incidence angle can create substantial changes in the glide ratio of a parafoil with respect to the atmosphere. However, it is the glide ratio of the system with respect to the ground that must be controlled to improve landing accuracy. The glide slope over ground is the ratio of the forward speed over ground to the descent rate, where the forward speed over ground is determined by adding the component of wind aligned with the flight path to the forward airspeed. Figure 5.28 provides a visualization of the relationship between aerodynamic glide ratio, wind speed, and glide slope over ground.

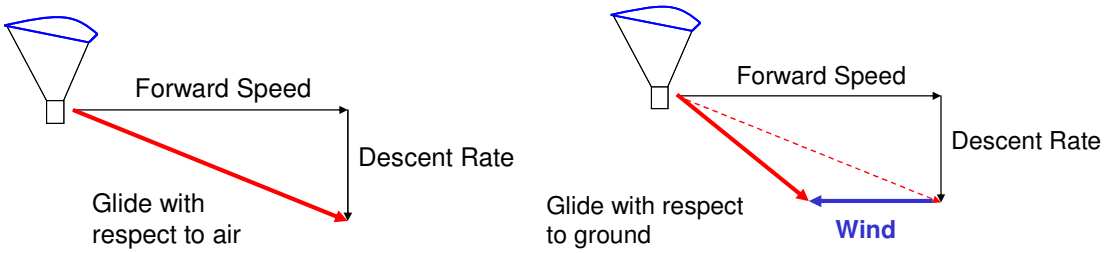

Figure 5.28: Glide Slope Over Ground

This is an important point because in any amount of wind, the glide slope over ground behaves in a very different manner than the glide slope with respect to the air. The variation in canopy incidence angle is used to vary the angle of attack of the parafoil canopy. The minimum incidence angle results in the minimum angle of attack which also corresponds to the minimum aerodynamic glide ratio but also the maximum airspeed. As incidence angle and, hence, angle of attack are increased, the glide ratio is increased while the airspeed is decreased. The consequence of this inverse relationship between aerodynamic glide angle and airspeed in terms of glide slope over ground is shown conceptually in Figure 5.29. In a zero wind environment, increasing incidence angle results in an increasing glide ratio over ground. As the wind is increased, the effect of variable incidence angle on glide slope over ground is diminished. In fact, there is a particular wind speed for which the variation in incidence angle will produce no change in the glide slope over ground. Beyond this wind speed, the effect of incidence angle on glide slope over ground is reversed, so that the maximum glide slope over ground is now achieved at the minimum incidence angle setting.

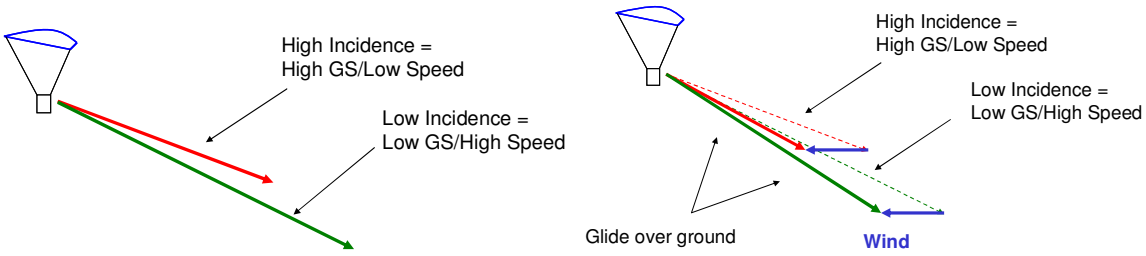

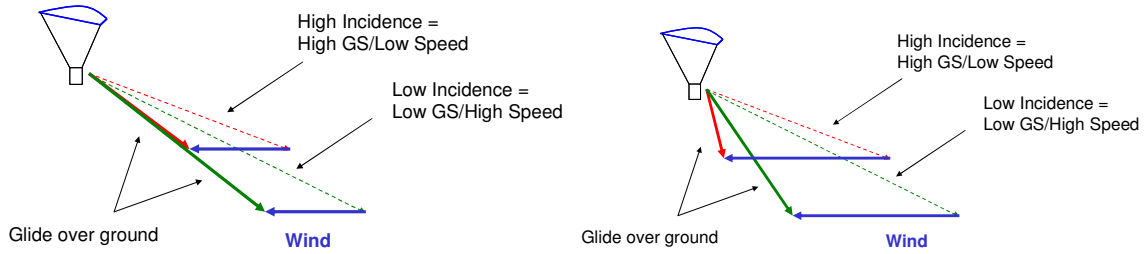

Figure 5.29: Behavior of Glide Slope over Ground vs. Incidence Angle

The use of symmetric trailing edge brake deflection to provide airspeed control in conjunction with variable incidence angle can dramatically improve the range of control of glide slope over ground. Figure 5.30 through Figure 5.33 show the range of glide slope over ground which can be achieved with incidence angle variation alone, and with incidence angle variation in conjunction with symmetric brake deflection. These results are based on the flight characteristics of the medium aspect ratio canopy used for the variable incidence angle flight tests discussed above. As shown in Figure 5.30 and Figure 5.31, the variation of the canopy incidence angle provides a significant range of control of glide slope over ground in zero and light wind conditions, while the deflection of trailing edge brakes provides almost no effect on glide slope control over ground. This is because trailing edge deflection provides a change in airspeed with little change in the aerodynamic glide angle of the parafoil canopy.

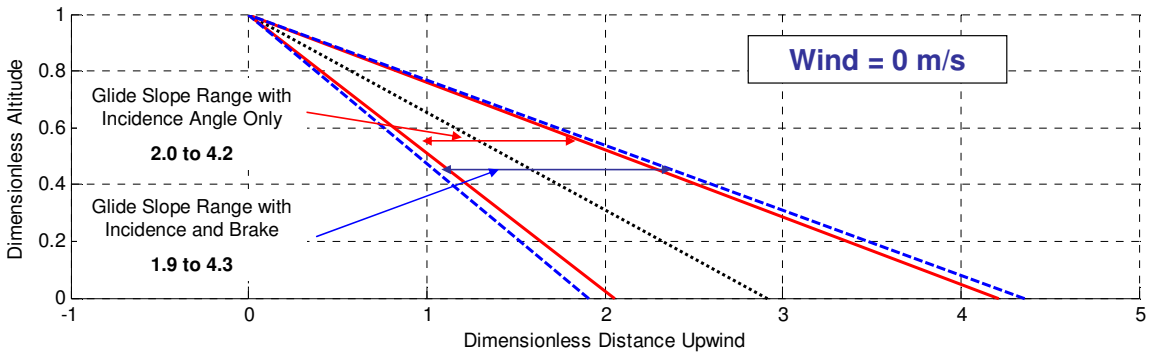

Figure 5.30: Range of Glide Slope over Ground in No Wind

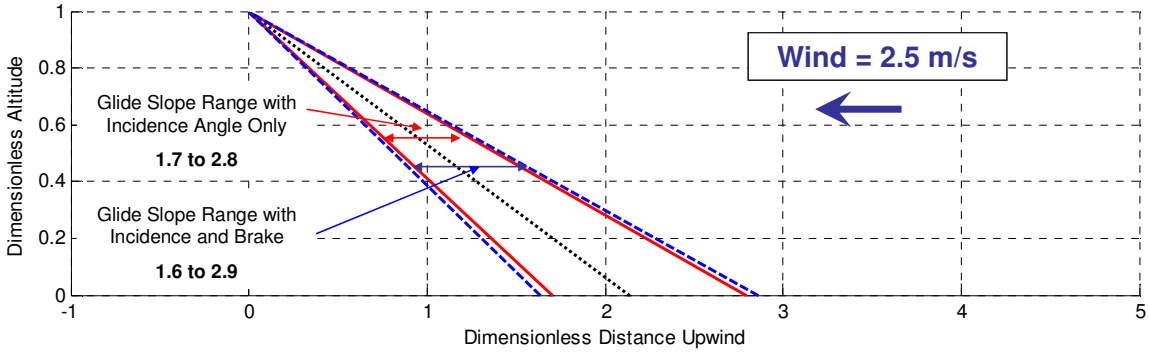

Figure 5.31: Range of Glide Slope over Ground in Light Wind

However, as shown in Figure 5.32, when the wind increases to the point where the variation of incidence angle produces no change in the glide slope over ground, the use of trailing edge brake deflection to alter speed can produce a significant range of control in the glide slope over ground. Furthermore, as shown in Figure 5.33, the range of glide slope control in stronger wind conditions can be dramatically increased by the use of trailing brakes in conjunction with incidence angle variation.

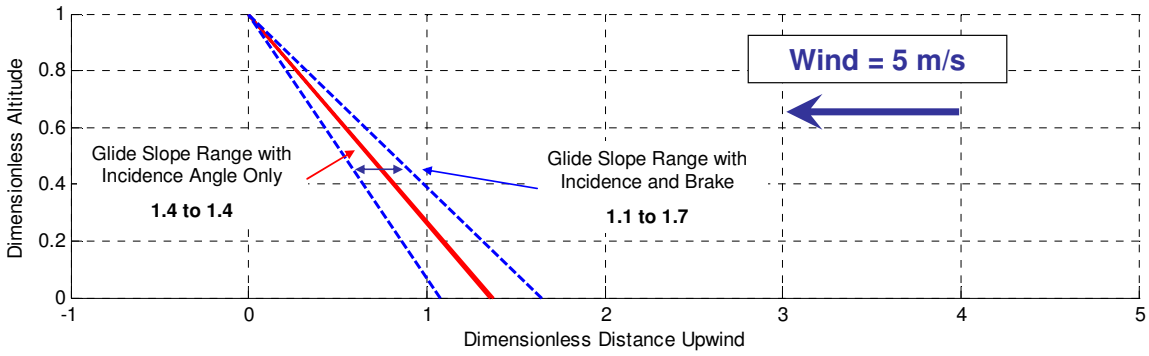

Figure 5.32: Range of Glide Slope over Ground in Moderate Wind

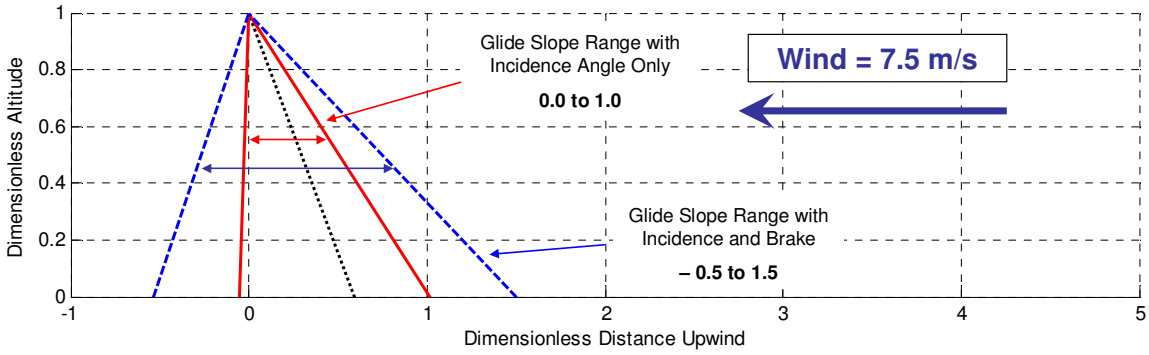

Figure 5.33: Range of Glide Slope over Ground in Strong Wind

To summarize, the variation of canopy incidence angle produces a significant change in the aerodynamic glide ratio of a parafoil, but the actual change in glide slope over ground can be dramatically reduced in certain wind conditions. The use of trailing edge brake deflection in conjunction with incidence angle variation can compensate for the reduced control authority in these wind conditions can dramatically improve the control authority in windy conditions.

CHAPTER 6

PARAFOIL GLIDE SLOPE CONTROL

Longitudinal control is obtained with a nonlinear proportional control strategy based on the coupled use of canopy incidence angle and trailing brake deflection to track a commanded glide slope over ground. This is an entirely new concept for guided airdrop control and is one of the primary contributions of this dissertation.

The glide slope control strategy is based on a nonlinear proportional control law which can be divided into two parts, 1) generating a commanded glide slope based on the current state of the parafoil aircraft and the environment, 2) determining the correct control input to achieve the commanded glide slope.

In discussing the formulation of the glide slope command logic, it is helpful to consider a quantity called the glide path to target:

$$GS_T = d / z \tag{6.1}$$

where d is the distance downwind from the target and z is the current altitude above the target. The glide slope control strategy is to make a straight line final approach to the target from directly downwind. While on final approach, if the glide slope over ground of the parafoil and payload aircraft is equal to the glide path to target, the aircraft will intersect the target. If the glide path to target is steeper than the minimum glide slope over ground of the parafoil, the system will fly past the target, and if the glide path to

target is shallower than the maximum glide slope over ground of the parafoil, the system will land short of the target. In this way, the minimum and maximum glide slopes over ground define the boundaries of the region from which the parafoil and payload aircraft will be able to reach the target. To maximize the ability of the system to reject any disturbances during final approach, the system should seek to maintain a nominal glide path in the center of this region. A normalized glide path error is defined as follows:

$$e_{GS} = \frac{GS_{nom} - GS_T}{(GS_{\max} - GS_{\min})/2} \tag{6.2}$$

When the glide path error is 0, the system is on an intercept course with the target on the nominal glide path. When the glide path error is 1, the system will hit the target with the controls set for minimum glide slope over ground, and when the glide path error is -1 the system will hit the target with the controls set for maximum glide slope over ground. To minimize control inputs near the nominal glide path, the glide slope commands are made proportional to the square of the glide path error. Finally an additional parameter e_{SAT} is used define the magnitude of glide path error at which the controls saturate. The parameter e_{SAT} is set to a value less than one so that the controls will saturate before the system reaches the minimum and maximum glide slope boundaries. The resulting glide slope command logic given in equations (6.1) through (6.4) provides a simple method for choosing a commanded glide slope GS_C based on the current glide path to target and the range of glide slope over ground that the parafoil can achieve in the current atmospheric conditions.

$$\tilde{e}_{GS} = \begin{cases} \min(e_{GS} / e_{SAT}, -1), & e_{GS} < 0 \\ \max(e_{GS} / e_{SAT}, 1), & e_{GS} > 0 \end{cases} \tag{6.3}$$

$$GS_C = \begin{cases} GS_{nom}(1 - \tilde{e}_{GS}^2) + \tilde{e}_{GS}^2 GS_{\max}, & e_{GS} < 0 \\ GS_{nom}(1 - \tilde{e}_{GS}^2) + \tilde{e}_{GS}^2 GS_{\min}, & e_{GS} > 0 \end{cases} \tag{6.4}$$

An example of the glide slope commands generated with this method is shown in Figure 6.1. For this scenario, the minimum glide slope over ground is set at 1, the maximum is set at 3, and the normalized error at which the controls saturate, e_{SAT}, is set at 0.5. The plot shows how the commanded glide slope is generated to bring the system smoothly onto an intercept course with the target on the nominal glide path. If the system is outside the boundaries set by the e_{SAT} parameter, the maximum or minimum glide over ground is commanded to bring the system back towards the nominal glide path, and if the system is outside the minimum and maximum glide slope boundaries it will not be able to reach the target.

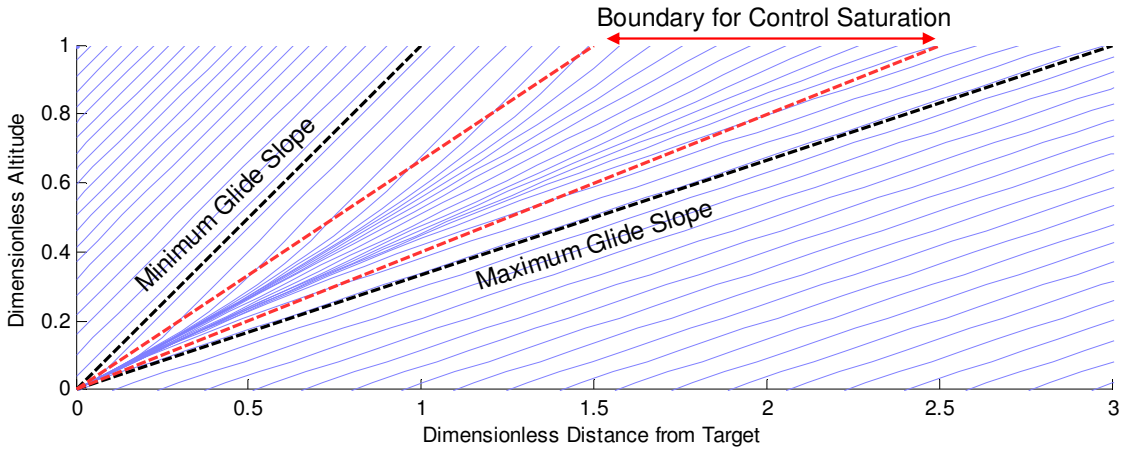

Figure 6.1: Visualization of Commanded Glide Slope Logic

The second part of the glide slope control algorithm is the selection of appropriate control inputs to achieve the commanded glide slope. This is done by inverting the mapping of incidence angle and brake deflection to glide slope over ground. For convenience and computational efficiency, mappings of incidence angle and brake deflection to horizontal airspeed and descent rate are stored as polynomial functions of normalized brake and incidence angle inputs.

$$\begin{aligned} V_A &= V_0 + \partial V_I \tilde{\delta}_I + (\partial V_B + \partial V_{BI} \tilde{\delta}_I + \partial V_{BI2} \tilde{\delta}_I^2) \tilde{\delta}_B \\ \dot{z} &= \dot{z}_0 + \partial \dot{z}_I \tilde{\delta}_I + \partial \dot{z}_{I2} \tilde{\delta}_I^2 + (\partial \dot{z}_B + \partial \dot{z}_{BI} \tilde{\delta}_I + \partial \dot{z}_{BI2} \tilde{\delta}_I^2) \tilde{\delta}_B \end{aligned} \tag{6.5}$$

Brake deflection and incidence angle are normalized to span the range -1 to 1. In practice, the limits of incidence angle are actually a function of the level of brake deflection. The limit on incidence angle is assumed to be linear function of brake input.

$$\begin{aligned} \tilde{\delta}_B &= 2(\delta_B - \delta_{B,MIN}) / (\delta_{B,MAX} - \delta_{B,MIN}) - 1 \\ \delta_{I,MIN} &= \delta_{IMIN0} + \delta_{IMINB} \delta_B \\ \tilde{\delta}_I &= 2(\delta_I - \delta_{I,MIN}) / (\delta_{I,MAX} - \delta_{I,MIN}) - 1 \end{aligned} \tag{6.6}$$

The speed over ground is determined by subtracting the wind speed from the forward airspeed estimate, and the glide slope over ground is determined as the ratio of the speed over ground to the descent rate.

$$GS = (V_A - V_W) / \dot{z} \tag{6.7}$$

Sample mappings were created to fit the flight test data vehicle used for autonomous landings. Contours of constant glide slope over ground for these example mappings are shown vs. incidence angle and brake deflection for 4 different wind levels in Figure 6.2.

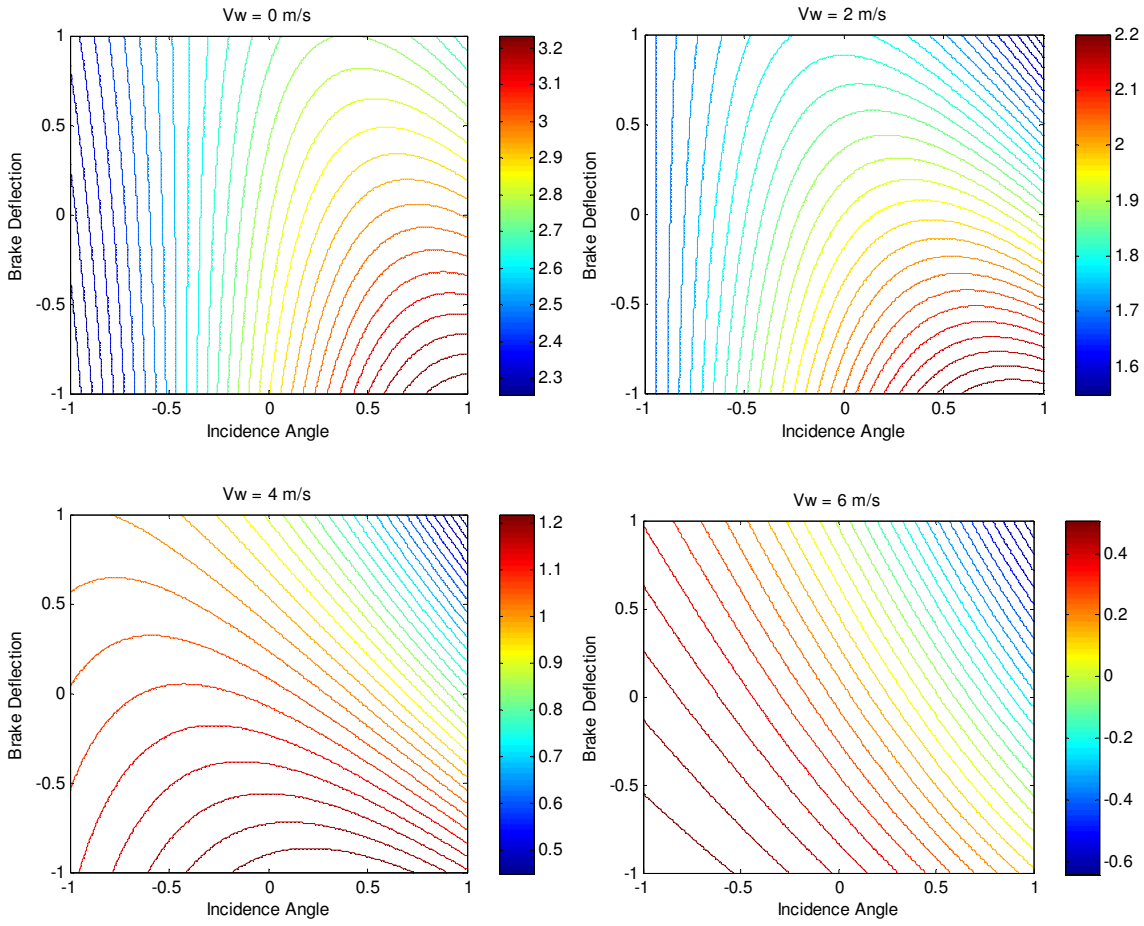

Figure 6.2: Glide Slope over Ground vs. Incidence Angle and Brake at Increasing Wind Levels

These plots demonstrate how very different the effect of the control inputs on glide slope over ground can be in different wind conditions. As stated above, the effect of incidence angle on glide slope over ground can be completely opposite in different wind

conditions. There is a complex interaction between incidence angle and trailing edge brake in determining the glide slope over ground in different wind conditions.

It is also clear from the plots in Figure 6.2 that a wide range of control inputs can produce the same glide slope over ground. The goal is to choose the "optimal" set of control inputs which achieves the commanded glide slope over ground. It is an interesting area for further research to explore different definitions of the "optimal" control logic for inverting the glide slope mapping. For instance, the controls could be chosen which either minimize or maximize the airspeed for a specified glide slope over ground. Alternatively, the controls could be chosen such that the system is able to move from the maximum to minimum glide slope setting in the minimum time. This idea inspired approach taken for this dissertation, which is to restrict the controls to lie on a line drawn on the glide slope mapping from the maximum glide point to the minimum glide point. This ensures that the full range of glide over ground is achieved, and the problem of inverting the nonlinear mapping to obtain the controls to achieve a given glide slope command is reduced to a line-search problem. The attraction of this approach is the simplicity of implementation and minimal computation time required.

These lines of optimal control inputs are plotted on top of the glide slope contours in Figure 6.3. The line-search problem is solved with successive three point quadratic approximations. In fact, since the minimum and maximum glide slope configurations always lie on the boundaries of the mapping, these quantities can be determined using the same line search algorithm.

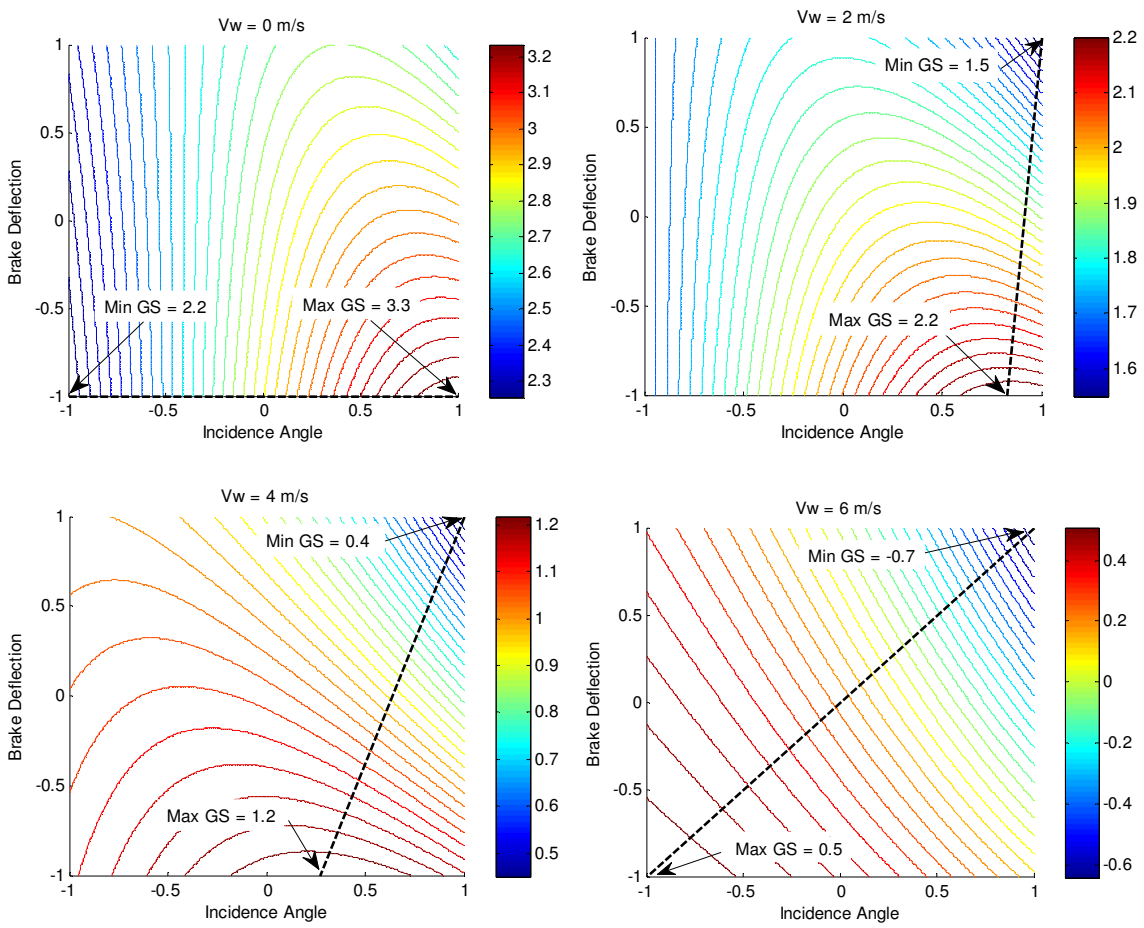

Figure 6.3: Range of "Optimal" Control Inputs at Increasing Wind Levels

Simulation results of an example final approach from an altitude of 100 m are shown in Figure 6.4. Two cases are shown, one cases uses the glide slope controller described above, the second case has the controls fixed. The minimum, maximum, and nominal glide slope lines shown in Figure 6.4 were determined based on the average winds during the final approach. The wind profiles used for the example approach are shown in Figure 6.5. The average wind is 5 m/s and the standard deviation of the vertical wind component used for the Dryden turbulence model is 0.8 m/s. Initially, the system is nearly on the

nominal glide path with the controls centered. Once the altitude drops below approximately 40 meters, the head wind weakens and, to make matters worse, a positive vertical wind component picks up. As shown by the controls-fixed flight path, this combination of changes in the wind would normally cause the system to overshoot by nearly 40 meters. As shown in Figure 6.6, the glide slope controller reacts to this change in the wind by quickly applying a large amount of trailing edge brake and increasing the incidence angle to the maximum setting. This causes a large reduction in forward flight speed and a significant reduction in the glide slope over ground, allowing the system to stay on the nominal glide path to the target.

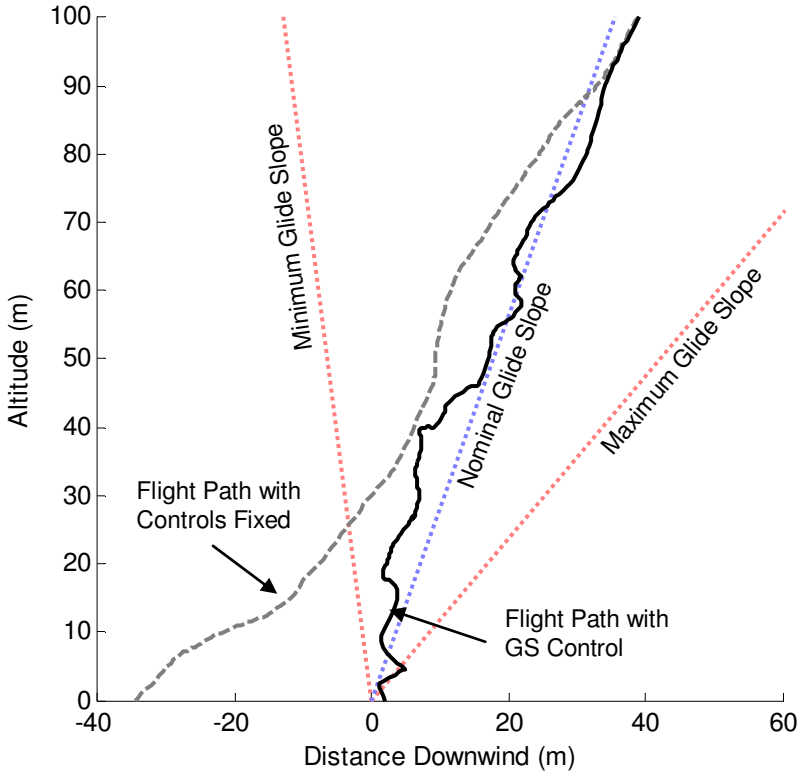

Figure 6.4: Final Approach Trajectories with and without Glide Slope Control

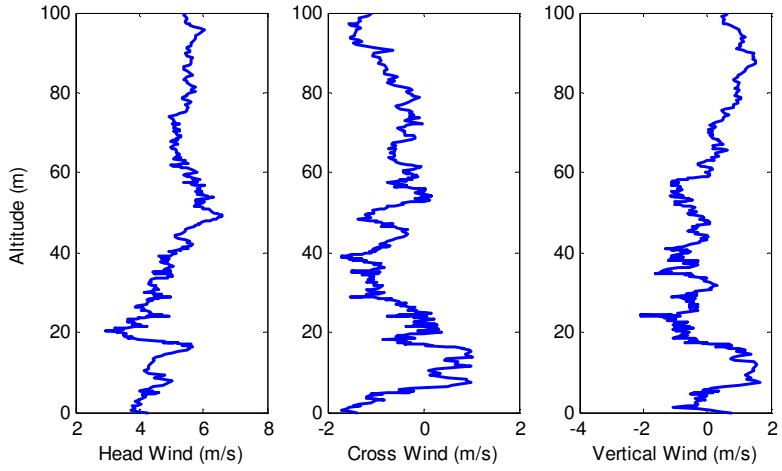

Figure 6.5: Wind Profiles for Example Approach

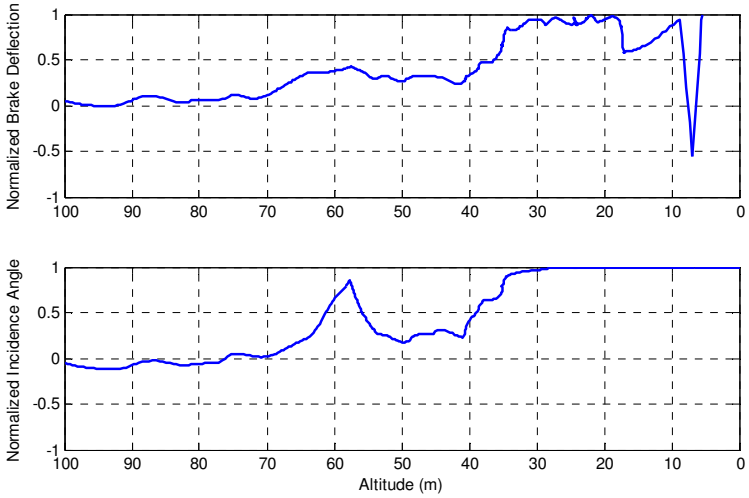

Figure 6.6: Control Inputs During Example Approach

To summarize, a nonlinear proportional glide slope controller was developed to utilize trailing edge deflection in conjunction with incidence angle variation to control glide slope over ground during a straight line final approach. The controller consists of two parts, a glide slope over ground command logic designed to keep the system on a nominal flight path to the target and an inversion of the control to glide slope mapping to obtain the optimal control input based on the commanded glide slope and wind conditions.

CHAPTER 7

IN-FLIGHT SYSTEM IDENTIFICATION

A. Benefits of In-Flight System Identification

A unique feature of airdrop systems is the inherent and large variability in flight dynamic characteristics. The same physical article dropped on two different occasions will exhibit significantly different dynamic response. In addition, a practical system will be expected to carry payloads of varying geometry and weight. Control systems for autonomous airdrop systems explicitly or implicitly assume knowledge of the flight dynamic characteristics in some way shape or form. A question facing autonomous airdrop designers is whether to use pre-computed dynamic characteristics inside the control law, or to compute the needed flight dynamic characteristics in flight and subsequently employ them in the control law. The first paper written as part of this dissertation established conditions when in-flight identified characteristics, with a focus on the turn rate dynamics, should be used, and when it is better to use pre-computed results. It was shown that with expected levels of system variability, sensor noise, and atmospheric wind, in-flight identification generally produces significantly more accurate dynamic behavior of the lateral dynamics than a pre-computed model of the nominal system, even when the in-flight identification is performed with highly inaccurate sensor data. The only exception to this rule observed in this work is the situation where atmospheric winds are high and a direct heading measurement is not available. In this

situation, a pre-computed estimate of the time constant of the lateral dynamics is more accurate than an in-flight estimate. These conclusions were reached though a comprehensive simulation study using a validated airdrop flight dynamic model applied to both a small and large parafoil.

Monte Carlo simulations were run to investigate the sensitivity of the results to changes in the assumed levels of sensor error, model uncertainty, and wind levels. The model uncertainty levels used in the first simulation were scaled from zero (perfect knowledge of the system) to 1.5 times expected levels (expected levels based on previous flight tests are +/- 15% asymmetric control bias, +/-25% left and right control sensitivities, +/-25% payload weight, and +/- 5% C_{L0} and C_{D0} for the entire canopy). The standard deviations for all of the sensor errors were scaled from zero (perfect sensors) to 2 times the expected levels (assumed sensors are GPS only and GPS with a heading measurement, see [10] for details). Cases were run with no wind and with constant mean wind magnitudes of 5 m/s (half the system airspeed) and 10 m/s (equal to system airspeed). From the results, the boundaries where the in-flight system identification and the fixed model produce the same errors in the steady state and transient turn response were calculated as a function of the model uncertainty and sensor error levels at the three different wind levels. Figure 7.1 explains how these boundaries are plotted. With model uncertainty on the y axis and sensor error on the x axis, the region above and to the left of the boundaries represents the space where the model uncertainty is large enough and the sensor data is good enough that it is better to perform the system identification in flight as

opposed to using a fixed model of the flight dynamics. The actual results are shown in Figure 7.2 and Figure 7.3.

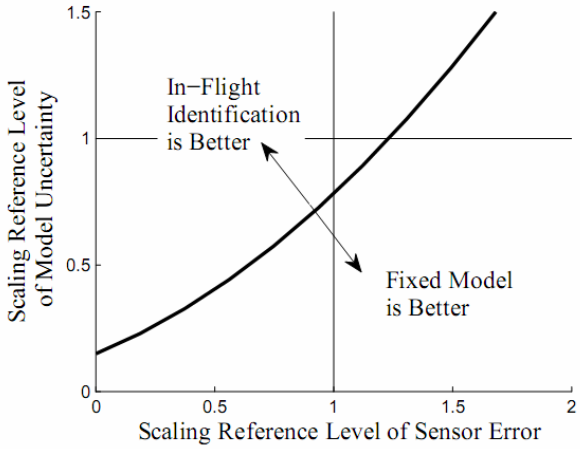

Figure 7.1: Explanation of In-Flight Identification vs. Fixed Model Boundaries

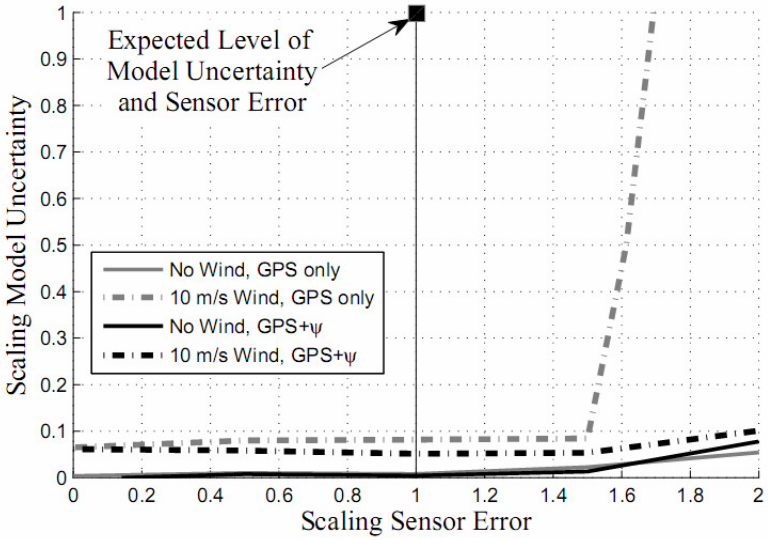

Figure 7.2: In-Flight Identification vs. Fixed Model Boundaries for Steady State Parameters

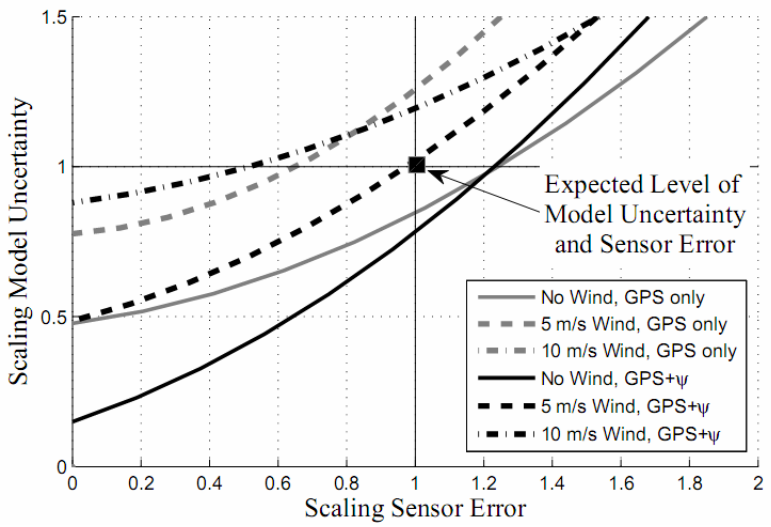

Figure 7.3: In-Flight Identification vs. Fixed Model Boundaries for Transient Response

Figure 7.2 shows that if there is any flight-to-flight variation in the system at all, then it is better to estimate the steady state characteristics of the system in flight. Figure 7.3 shows that when only GPS measurements are available it is difficult to obtain a good estimation of the transient response with moderate to high wind levels. The boundary for the 10 m/s wind case lies off the chart because it is better to use a fixed model over the entire range of sensor error and model uncertainty considered. For the results with the heading sensor included, the boundaries run through the assumed levels of model uncertainty and sensor errors, implying that it makes little difference if the time constant is estimated in flight or if a pre-computed time constant is used.

System identification relies on state estimates that are degraded by atmospheric turbulence and sensor errors. The traditional scenario when system identification is performed on the ground takes advantage of the ability to estimate parameters over multiple maneuvers and multiple flights so that the effects of sensor errors and turbulence

are averaged out. The results presented here show that it is always beneficial to estimate steady state quantities in flight with reasonable levels of model uncertainty, sensor noise, and wind because the estimation is performed by averaging over a series of measurements. On the other hand, transient characteristics estimated in flight over the small windows of data during maneuvers are much more sensitive to sensor noise and turbulence, and the results show that it is not always beneficial to estimate these transient characteristics in flight. In other words, for transient characteristics, the degradation in the quality of in-flight estimates from sensor noise and turbulence is comparable to the degradation in the quality of fixed estimates from model uncertainty. It is important to note that this result is dependent on the nature of the air vehicle. Airdrop systems typically have very benign flight dynamics, so precise control of the transient response is not required. For a vehicle with very lightly damped or unstable flight dynamics, precise transient control and, hence, accurate knowledge of the transient characteristics would be critical.

B. Implementation

The in-flight system identification is integrated into the loiter phase of the autonomous flight. The loiter phase consists of a series of figure eight turns created by tracking alternating loiter targets. Each time a loiter target is reached, a turn towards the next target is initiated. Reliable estimates of steady state characteristics are obtained by holding a gentle turn with constant control deflection, so this turning phase after a loiter target is reached is a convenient time to estimate steady state flight characteristics. Normally, the system turns until it is facing the next target and then begins homing to it,

but while estimating quantities in flight, the constant control segment is held until a criterion for a valid airspeed estimate (described below) is met. Pairs of left and right turning segments are completed at various incidence angle and brake levels to build an internal mapping of the controls to airspeed, descent rate and turn rate. A long loiter phase allows a greater opportunity to update the internal model. Conversely, if there is little or no time for loiter, then the internal model is not updated in flight.

The first step in the system identification process is wind estimation. The same method used to estimate wind and airspeed with the off-line system identification procedure described earlier in this dissertation is used for the in-flight system identification of the steady state flight characteristics. An upper bound on the airspeed estimation error was given as the following:

$$\sigma(\hat{V}_0) < \frac{\sigma(V_{GPS})}{\sin(\delta/4)^2}, \quad \delta = \min(|\Delta\psi|, 2\pi) \tag{7.1}$$

The airspeed error bound obtained from Eq. (7.1) provides a convenient metric for evaluating the quality of an airspeed estimate obtained in flight. If the result is 1, it indicates the system has completed at least one complete circle. This should always be true for the initialization phase of the autonomous flight. When performing a series of estimates during the loiter phase of the flight, the result from Eq. (7.1) is evaluated at each time step while recording data for a constant control segment. When the value falls below a threshold, it indicates that a valid airspeed estimate has been obtained, the constant control segment is ended, and the system returns to the normal loiter routine.

The remaining flight characteristics of interest are the descent rate and the heading rate. The descent rate can simply be averaged over the constant control segment and the standard deviation of the descent rate can be used as a metric to evaluate the quality of the estimate from a particular flight segment. One method for estimating the heading rate is to use the wind vector obtained from the linear regression to go back and solve the vector diagram in Figure 4.3 for every measurement of the constant control segment. This provides a series of heading angles which can then be differentiated to obtain heading rate. An alternative way to obtain heading rate is based on convenient approximation derived by Calise [87],

$$\dot{\psi} \approx \dot{\chi} V_G / V_0 \tag{7.2}$$

which allows heading rate to be determined from the ground speed, course rate (which can be obtained by differentiating the GPS ground course), and airspeed. Since the airspeed is a constant during the flight segment, the numerator in the heading angle approximation can be obtained at each measurement update and the airspeed can be divided out at the end of the flight segment. This approximation allows an efficient computation of the average heading rate over the constant control segment. In simulation, heading rates obtained with this approximation agreed with the heading rates calculated with the exact method described above to within 1%. The quality of a heading rate estimate is evaluated based on the standard deviation in heading rate over the flight segment.

CHAPTER 8

PERFORMANCE OF ADAPTIVE GLIDE SLOPE CONTROL

All autonomous landing results are based around the flight test vehicle shown in Figure 8.1 and Figure 8.2. The test vehicle is a small, electric powered parafoil aircraft with a flight weight of 4.5 lbs. The canopy is a 1.5 m^2, rectangular planform airdrop-style parafoil with an aspect ratio 2.35. The longitudinal response to symmetric brake and incidence angle were shown in Figure 3.4 through Figure 3.9, and the turn rate response to differential brake was shown in Figure 3.10.

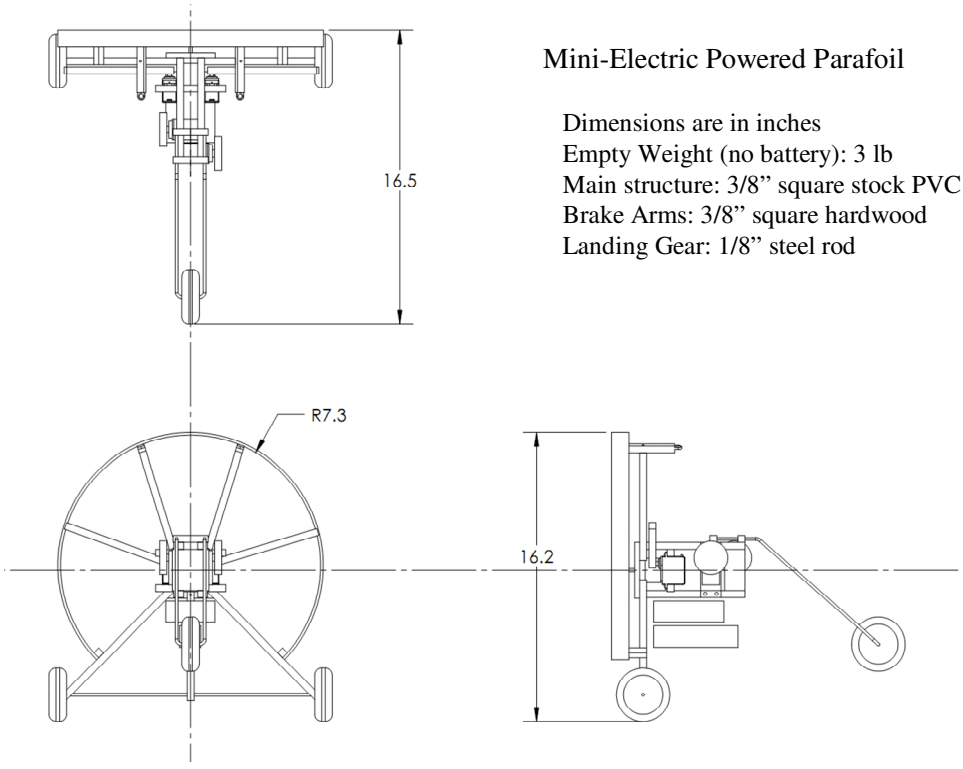

Figure 8.1: Schematic of Powered Parafoil and Payload Aircraft

Figure 8.2: Self Powered System in Flight

A. Performance of Glide Slope Control in Simulation

Predicted landing accuracy for the baseline case of autonomous landing using only lateral control is shown in Figure 8.3 for different wind speeds and levels of turbulence. The turbulence level is the standard deviation of the vertical wind component used in the Dryden gust model. This plot was generated by running 50 autonomous landing simulations with average wind speeds of 0, 2, 4, 5, and 6 m/s at turbulence levels of 0.0,

0.2, 0.4, 0.6, 0.8, and 1.0 m/s for a total of 1500 simulated landings. In general, increasing the level of turbulence increases the average miss distance. This is the expected trend for any autonomous airdrop landing algorithm. The plot shows that when using only lateral control, the landing accuracy becomes extremely sensitive to turbulence at high wind speeds. This is because the wind speed is approaching the nominal forward airspeed of 6 m/s for this particular system. A strong wind gust when the average wind is near the forward airspeed can push the system downwind of the target. If the gust persists, there is no way for the system to make progress upwind towards the target. Another interesting trend in this plot is the increase in average miss distance when the wind speed is near 2 m/s in turbulent conditions. The reason for this increase has to do with changes in the wind direction. In strong winds, even strong wind gusts will not produce dramatic changes in the wind direction. However, in light winds, even a small wind gust can result in a large change in the wind direction. The result is that in light, gusty conditions, it is not uncommon for the system to set up on final approach into the current wind direction, only to have the wind shift dramatically so that the system is landing across the wind or even downwind. As the mean wind speed increases, this occurs less frequently, and the system is almost always facing into the wind during the entire approach.

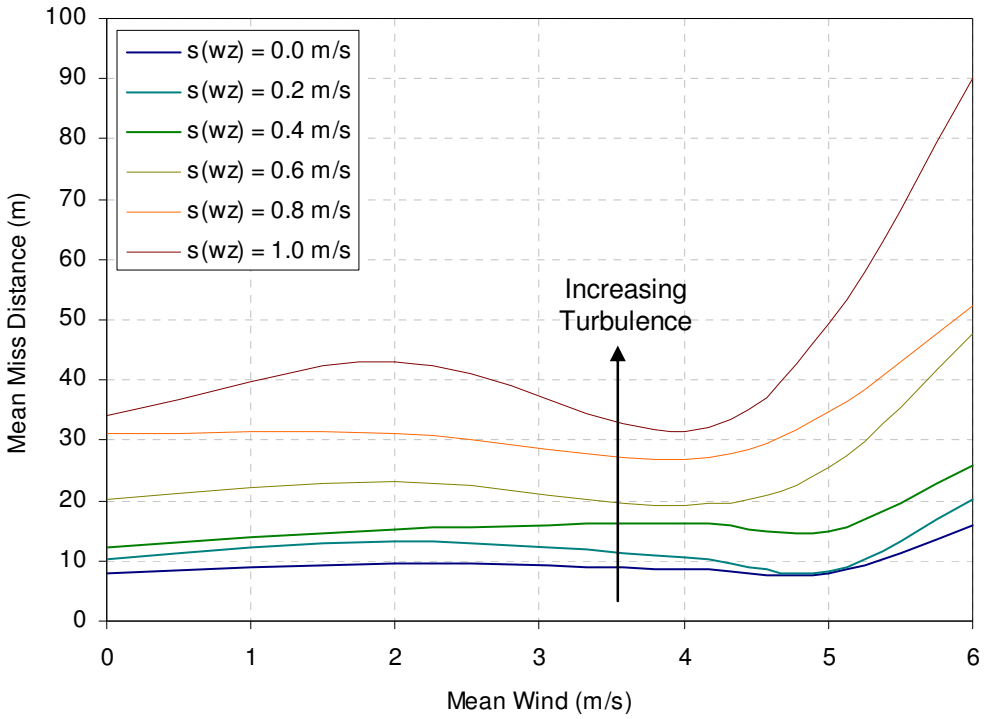

Figure 8.3: Predicted Landing Accuracy vs. Wind Speed using only Lateral Control

Figure 8.4 shows the simulated landing accuracy for autonomous landings with the glide slope controller. The same set of mean wind and turbulence combinations described above were run for a total of 1500 simulated landings. The average miss distance is significantly lower in most combinations of wind and turbulence. In zero wind with no turbulence, the average miss distances are essentially the same because there are no disturbances for the glide slope controller to react to. While increasing turbulence does tend to increase the average miss distance, increasing the average wind speed actually tends to decrease the average miss distance in all but the most turbulent cases. This is because the control authority of the glide slope controller is increased in windy

conditions due primarily to the increasing effect of trailing edge brakes on glide slope over ground as the wind speed increases.

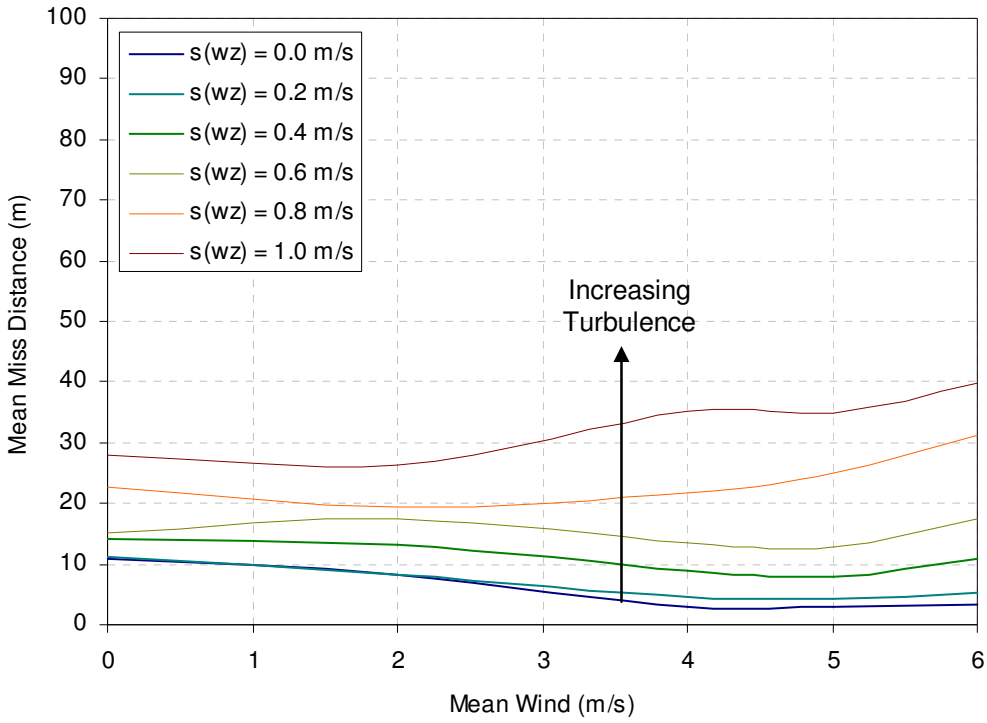

Figure 8.4: Predicted Landing Accuracy vs. Wind Speed using Glide Slope Control

Figure 8.5 shows the landing accuracy using the basic control algorithm compared to landing with glide slope control at different average wind levels. The turbulence level for this plot was set at 0.6 m/s. In light winds the addition of glide slope control provides a 30% improvement in landing accuracy. As the average wind increases to 5 m/s, the glide slope controller improves landing accuracy by a factor of two, and as the wind increase to 6 m/s, the glide slope controller improves accuracy by a factor of three. The important thing to take away from these plots is that the performance of any autonomous landing

algorithm can be heavily dependent on the average wind and especially the level of turbulence. In calm conditions there is little improvement in landing accuracy when using glide slope control because there is essentially nothing for the controller to do. It is in windy conditions when the addition of glide control begins to produce dramatic effects due largely to the wide range of forward airspeed that can be achieved by varying incidence angle in concert with the trailing edge brakes.

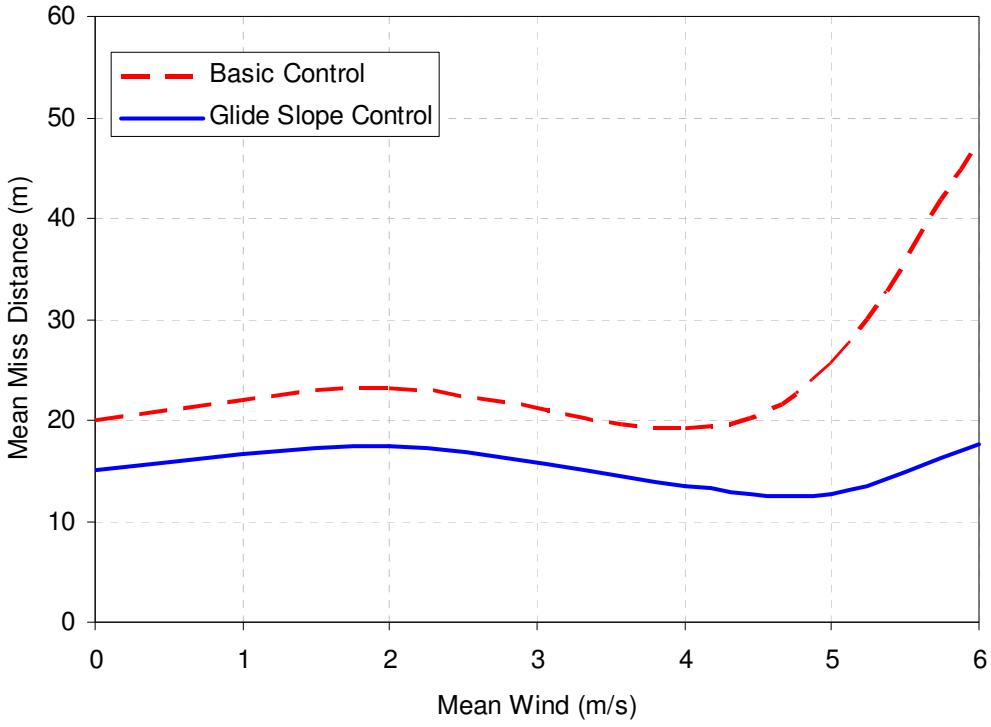

Figure 8.5: Comparing Predicted Landing Accuracy with Basic Control and with Glide Slope Control

Figure 8.6 compares the simulated landing dispersion of the basic and glide slope control algorithms with a turbulence level of 0.6 m/s and an average wind speed of 6 m/s. Positive downrange indicates downwind, so the wind is blowing from the bottom of these

plots and the system is approaching the target from positive downrange. Two circles are draw around the target, the solid circle has a radius equal to the average miss distance and the dashed circle has a radius equal to the median miss distance. The mean and median miss distances for the basic control algorithm are very different due to the very large miss distances when the system is blown downwind. By comparison, the glide slope control algorithm is able to prevent exceedingly large miss distances in the same condition due to the ability to change airspeed to counter the strong, varying winds.

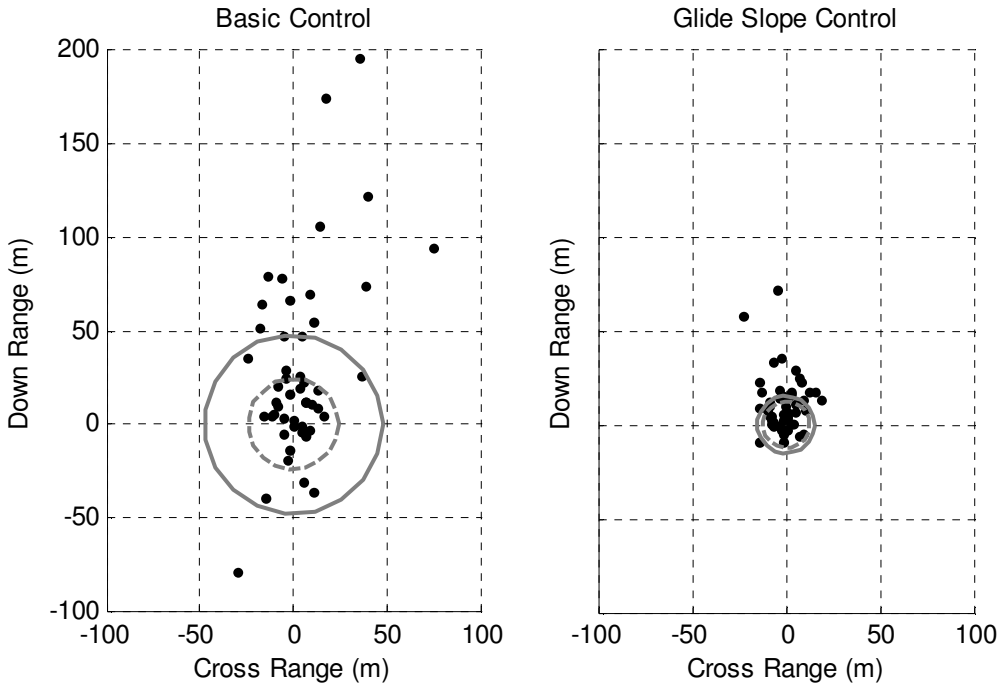

Figure 8.6: Comparing Simulated Landing Accuracy of Basic and Glide Slope Control Algorithms with Average Wind of 6 m/s

B. Performance of Glide Slope Control in Flight Test

The basic control algorithm and the glide slope control algorithm were tested in a series of autonomous flight tests. 22 flights were performed with the basic control

algorithm and 20 flights were performed with the glide slope control algorithm. The flight tests of each control algorithm were conducted simultaneously, switching between the basic control algorithm and the glide slope control algorithm for each flight. This was done to ensure that the testing for the two control algorithms took place in similar weather conditions. The landing dispersions for each control algorithm are shown in Figure 8.7. Note: all impact points reported in this dissertation are determined from the GPS position reading at the instant the system touches down. The miss distances are plotted vs. average wind speed in Figure 8.8 with the average miss distances from simulation plotted as solid lines. The median miss distance (often referred to in the airdrop community as the circular error probable, CEP) and mean miss distance predictions from simulation are compared with statistics computed from the flight test data in Table 8.1. The flight test results agree quite well with simulation. The landings with glide slope control are generally closer to the target. Furthermore, at high wind speeds there is a rapid increase in miss distance with the basic control algorithm, while no such increase occurs with the glide slope control algorithm.

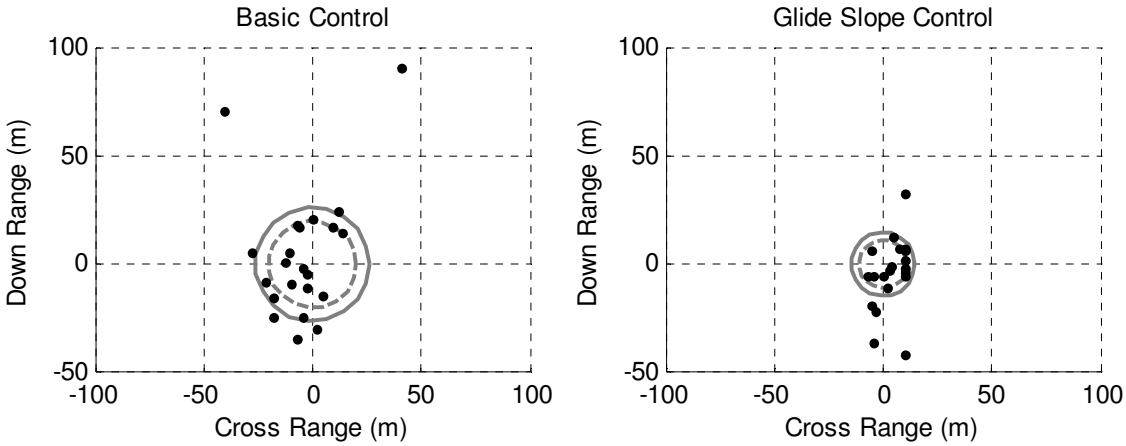

Figure 8.7: Landing Dispersions from Autonomous Flight Tests

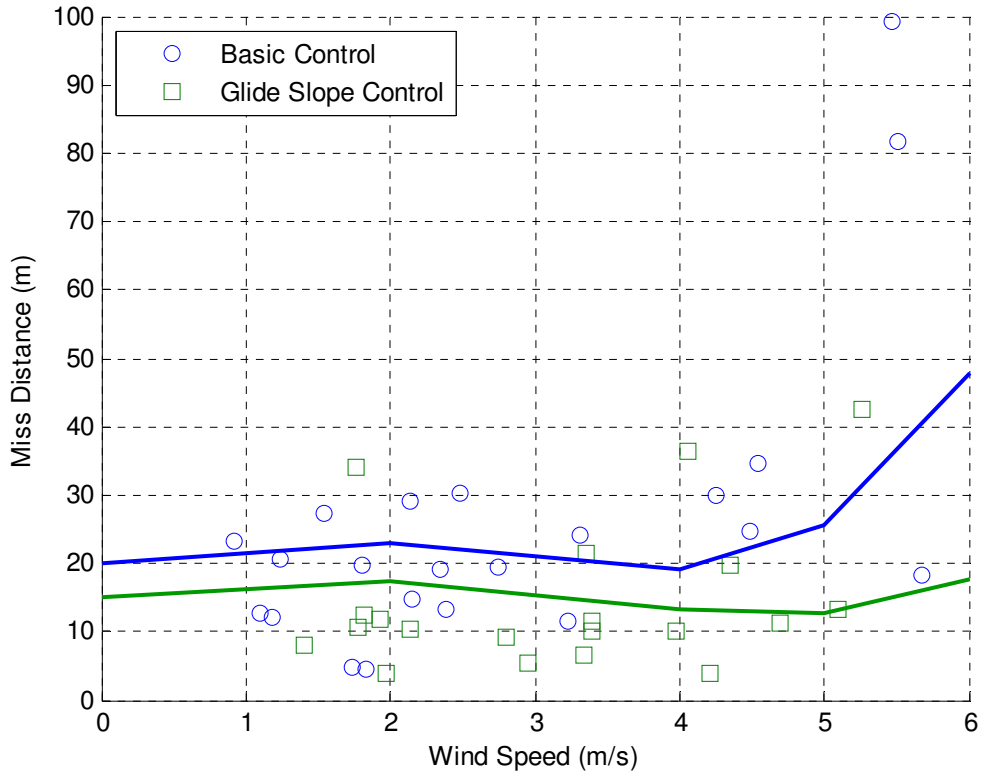

Figure 8.8: Comparing Flight Test Results of Landing Accuracy vs. Wind Speed with and without Glide Slope Control

Table 8.1: Simulated and Actual Landing Accuracy Statistics

	Simulation		Flight Test	
	CEP (m)	Mean Miss (m)	CEP (m)	Mean Miss (m)
Basic Control	19.1	27.2	20.1	26.2
Glide Slope	12.3	15.5	10.9	14.7

The excellent agreement between the accuracy predictions from simulation and the actual landing accuracy observed in flight test means that a high degree of confidence can be placed in trends in landing accuracy predicted with the simulation model. This allows

a number of interesting trade studies to be run very quickly which would otherwise entail weeks of flight testing.

C. Performance of Adaptive Glide Slope Control in Simulation and Flight Test

One of the primary difficulties of in-flight estimation of parafoil flight characteristics is the sensitivity to turbulence. A simulation study was performed to determine the influence of the turbulence level on the error in the in-flight estimates of three flight characteristics of interest, horizontal airspeed, descent rate, and heading rate. Fifty cases were run with an average wind of 3 m/s and turbulence levels of 0, 0.2, 0.4, 0.6, 0.8, and 1.0 m/s, for a total of 300 cases. The airspeed, descent rate, and heading rate values were compared to the known values from the simulation model. The average errors in each estimated quantity are plotted against the turbulence level in Figure 8.9. It is clear that reliable estimation of descent rate is extremely difficult to obtain in-flight. Horizontal airspeed and heading rate, on the other hand, can be estimated very reliably in flight even in very turbulent conditions. The reason for this is that the horizontal winds can be exposed by maintaining a gentle turn, allowing the airspeed to be distinguished from the wind vector, and heading rate can only by perturbed temporarily as the wind is changing in magnitude. In contrast, large slowly varying disturbances to descent rate can be caused by the vertical wind component, and there is no way to distinguish the wind component from the aerodynamic descent rate when only a measurement of the absolute descent rate is available.

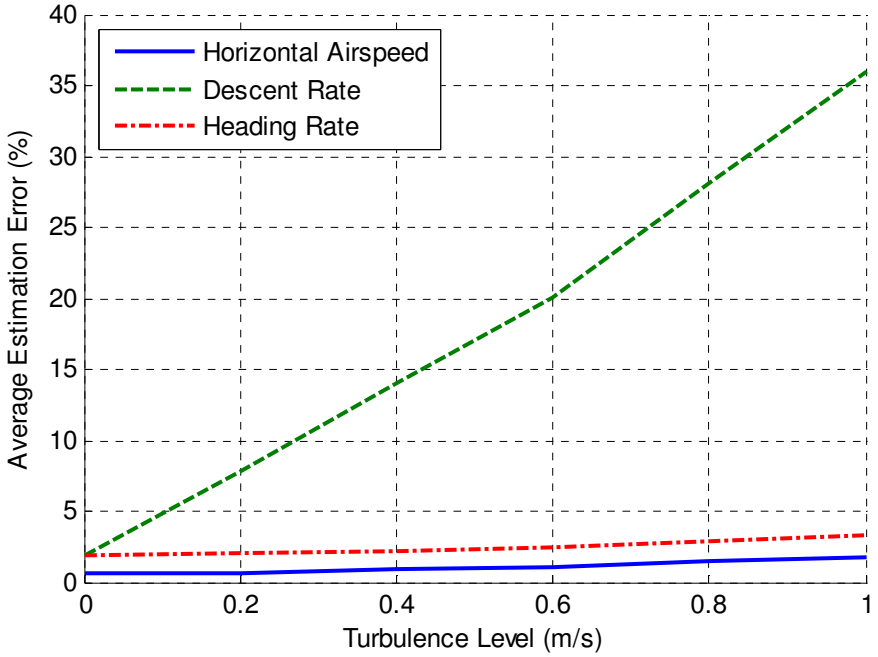

Figure 8.9: In-Flight Estimation Error vs. Turbulence Level

While it is not possible to separate the vertical wind component from the aerodynamic descent rate, it is possible to observe the presence of a significant vertical wind component. During the constant control segments used to produce the airspeed, descent rate, and heading rate estimates, any variation in descent rate from the mean value can only result from a vertical wind component. This means that while the average descent rate over a constant control segment contains contributions from both the vertical wind and the aerodynamic descent rate, the standard deviation of the descent rate over the segment contains only contributions from the vertical wind. Figure 8.10 shows the average in-flight estimation error of descent rate vs. the confidence interval in descent rate over the segment, where the confidence interval is approximated as twice the standard deviation over the square root of the number measurement sample. The strong correlation between the two quantities means that a reliable prediction of the quality of a

descent rate measurement obtained in flight can be obtained based on the computed standard deviation. For the remaining simulation results, a threshold of 0.155 m/s is set for the confidence interval on standard deviation, which corresponds to an average estimation error of 10%. If the confidence interval on the descent rate during a constant control segment exceeds this threshold, the descent rate data obtained for this segment is discarded.

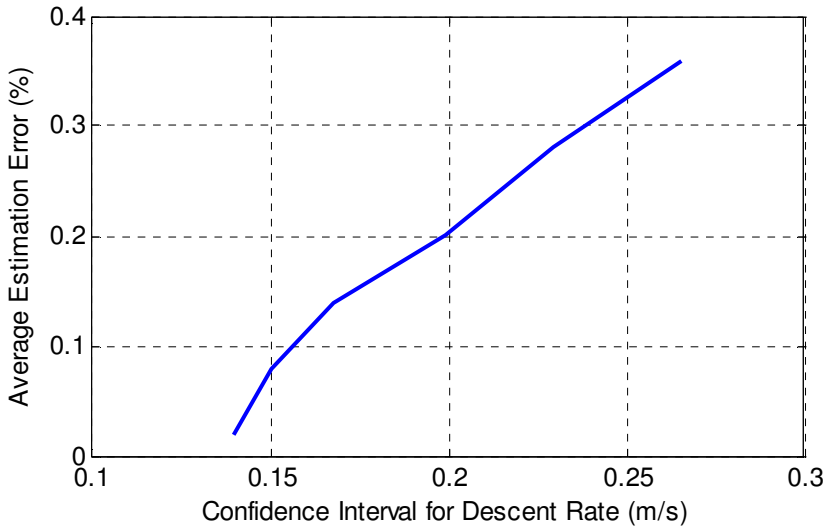

Figure 8.10: Correlation of Estimation Error to Descent Rate Confidence Interval

Six flights were conducted with the adaptive glide slope control algorithm with an average miss distance of 15 meters. Conditions were significantly more turbulent on this testing day compared to the flights shown in Figure 8.7. Three flights performed with the non-adaptive glide slope control algorithm on the same, turbulent day as the adaptive algorithm had miss distances of 36, 34, and 8 meters. The concern with using an adaptive algorithm is that in turbulent conditions, the in-flight estimates may be very poor, and if

the adaptive algorithm is not sufficiently robust, landing results could actually be worse with the adaptive algorithm. While these 6 adaptive flights are insufficient to compute statistically relevant landing accuracy numbers, it is clear from the excellent landing accuracy obtained in turbulent conditions that the adaptive control algorithm works properly in real flight conditions.

The heading rate, airspeed, and descent rate estimates from one of the adaptive flights are shown in Figure 8.11 through Figure 8.13. The steady state estimates obtained from the in-flight system identification algorithm for each segment of constant control are plotted on top of the real-time estimates from the navigation algorithm.

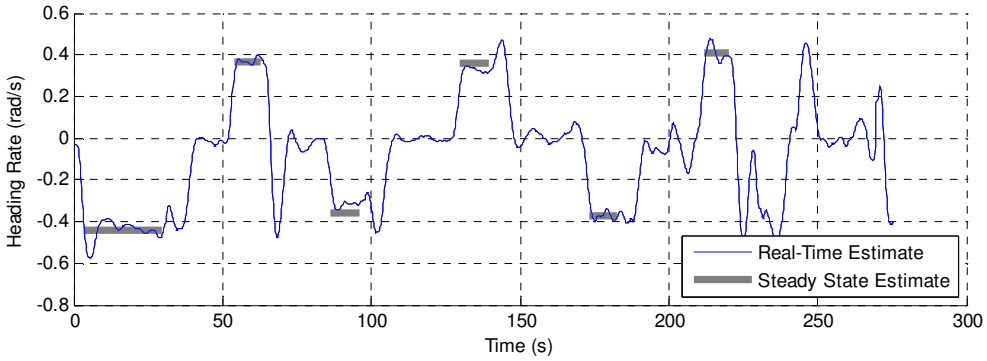

Figure 8.11: In-Flight Heading Rate Estimates

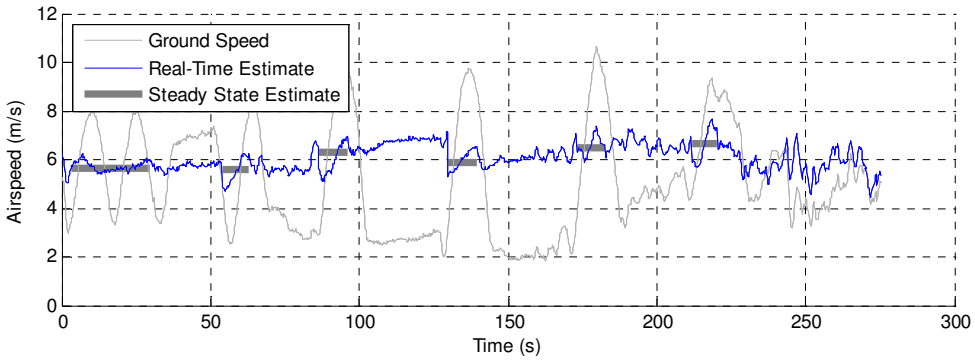

Figure 8.12: In-Flight Airspeed Estimates

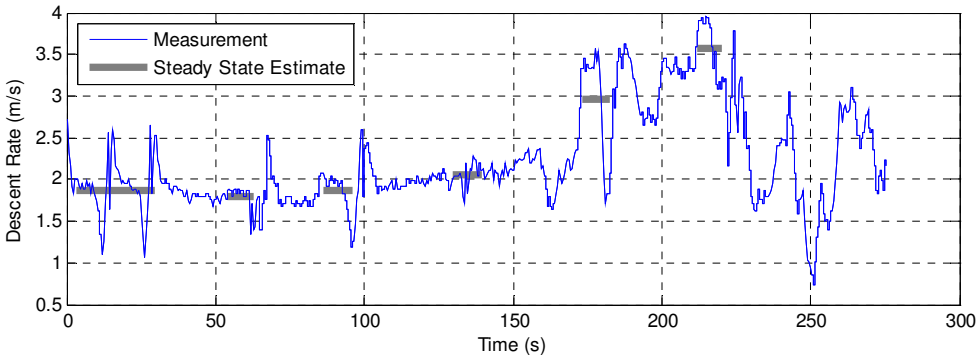

Figure 8.13: In-Flight Descent Rate Estimates

The large variation in descent rate during the constant control segments apparent in Figure 8.13 are evidence of the turbulent atmospheric conditions. The first two segments consist of left and right turns with the nominal incidence (0 cm) and brake deflection (-8 cm), the second two segments had the incidence control set at 0cm and brakes at 0cm, and the last two had the incidence set at -6cm and the brakes at -8cm. The steady state estimates for each segment are given in Table 8.2. The airspeed confidence is computed based on Eq. (7.7), while the descent rate and turn rate confidence values are twice the standard deviation over the square root of the number of measurements.

Table 8.2: In-Flight Airspeed, Descent, and Turn Rate Estimates

Segment	Airspeed (m/s)	Descent Rate (m/s)	Turn Rate (rad/s)	Airspeed Confidence	Descent Rate Confidence (m/s)	Turn Rate Confidence (rad/s)
1	5.64	1.87	-0.44	1	0.061	0.013
2	5.60	1.79	0.37	1.5	0.049	0.024
3	6.29	1.87	-0.36	1.5	0.067	0.024
4	5.91	2.06	0.36	1.5	0.043	0.023
5	6.48	2.97	-0.37	1.5	0.189	0.026
6	6.67	3.58	0.41	1.5	0.104	0.031

The airspeed confidence level is 1 for the initialization segment because this segment covers more than a complete circle, and the confidence level 1.5 for remaining segments because this was the threshold used to define the minimum length of each segment. The descent rate confidence interval threshold was set to 0.65 m/s for the flight tests, so the descent rate estimates for segments 3, 5, and 6 are considered invalid.

Figure 8.14 through Figure 8.16 show how the internal models of turn rate, airspeed and descent rate are updated from the initial guesses to match the estimates obtained in flight. The updated models demonstrate the successful adaptation of the internal flight dynamic model to match in-flight observations in actual, turbulent flight conditions.

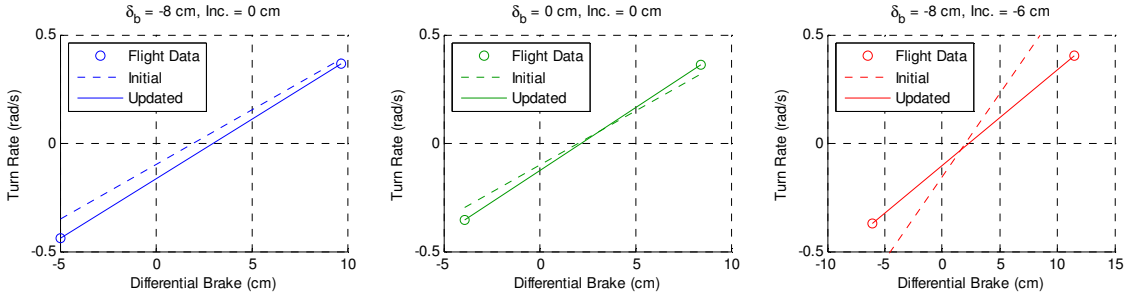

Figure 8.14: Initial and Updated Turn Rate Model Compared to Flight Data

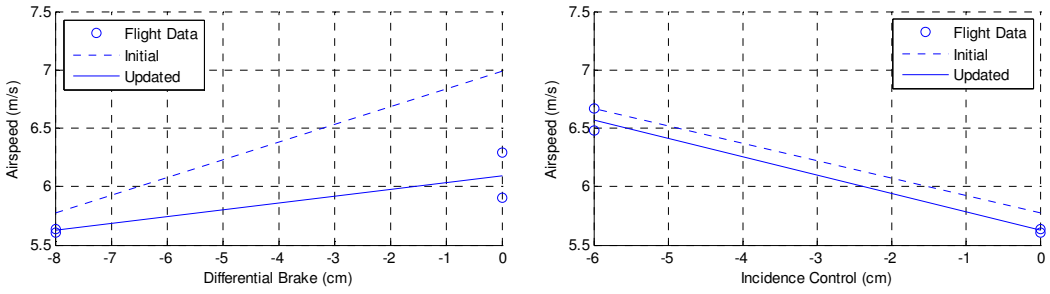

Figure 8.15: Initial and Updated Airspeed Model Compared to Flight Data

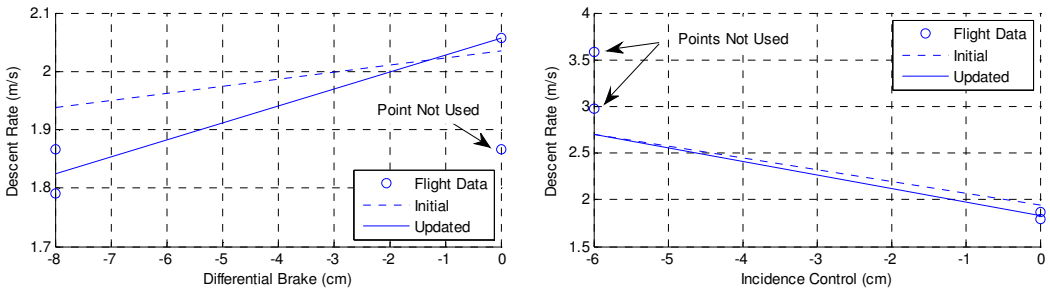

Figure 8.16: Initial and Updated Descent Rate Model Compared to Flight Data

To explore the benefits of in-flight system identification a series of autonomous landing simulations were performed with different levels of model uncertainty and different levels of adaptation. All of the flights included the 6 segment in-flight system identification and mapping update procedure used for the flight tests described above. In order to model uncertainty in a reliable and easily quantifiable way, perturbations are made to the internal model used by the autonomous landing algorithm rather than the parafoil simulation. Perturbations were made to the internal airspeed, descent rate, turn rate, and turn bias models. The perturbations to airspeed, descent rate, and turn rate are made as scalers, while the turn bias perturbations are absolute values. The forms of the perturbations are given in Eq. (8.1), where the subscript *INT* indicates the internal model, and the subscript *GNC* indicates the perturbed value used by the guidance, navigation, and control algorithm.

$$
\begin{aligned}
V_{0,GNC} &= V_{0,INT}\, p_{0,V}, \partial V_{B,GNC} = \partial V_{B,INT}\, p_{B,V}, \partial V_{I,GNC} = \partial V_{I,INT}\, p_{I,V} \\
\dot{z}_{0,GNC} &= \dot{z}_{0,INT}\, p_{0,Z}, \partial \dot{z}_{B,GNC} = \partial \dot{z}_{B,INT}\, p_{B,Z}, \partial \dot{z}_{I,GNC} = \partial \dot{z}_{I,INT}\, p_{I,Z} \\
\partial a_{TR,GNC} &= \partial a_{TR,INT}(p_{0,TR} + p_{I,TR}\tilde{\delta}_I + p_{B,TR}\tilde{\delta}_B) \\
\delta a_{BIAS} &= p_{0,DAB} + p_{I,DAB}\tilde{\delta}_I + p_{B,DAB}\tilde{\delta}_B)
\end{aligned}
\tag{8.1}
$$

The ranges of the perturbations are given in Table 8.3. The range for the bias term is normalized by the maximum differential brake deflection, so all the ranges are non-dimensional. The ranges were chosen to represent a typical level of uncertainty when flying a parafoil and payload aircraft for the first time. A series of autonomous landings with varying levels of model uncertainty. A model uncertainty of 0 corresponds to no perturbation of the internal model, while a model uncertainty of 1 indicates that the majority of the perturbations will be at the maximum values. This is done by selecting the perturbations randomly from bounded normal distribution scaled according to achieve the desired uncertainty level.

Table 8.3: Ranges of Model Perturbations

	V	$\dot{z}$	TR	δa_{BIAS}
p_0	(0.5,1.5)	(0.5,1.5)	(0.5,1.5)	(-.3,.3)
p_B	(0,2)	(0,2)	(-0.5,0.5)	(-.3,.3)
p_I	(0,2)	(0,2)	(-0.5,0.5)	(-.3,.3)

Fifty simulated landings were performed at model uncertainty levels of 0, 0.25, 0.5, 0.75 and 1.0. The mean wind was to 3 m/s and the turbulence level set to 0.5 m/s for all cases. The set of simulations was repeated for a basic case using glide slope control with

no adaptation of the internal model. In the second case, the internal model of turn rate and control bias was adjusted to match in-flight measurements. In the third case, the internal turn rate and horizontal airspeed models were adjusted to match flight data. Finally, for the fourth case, all of the internal models were adjusted based on flight test data. The average landing accuracy vs. model uncertainty for each case is shown in Figure 8.17.

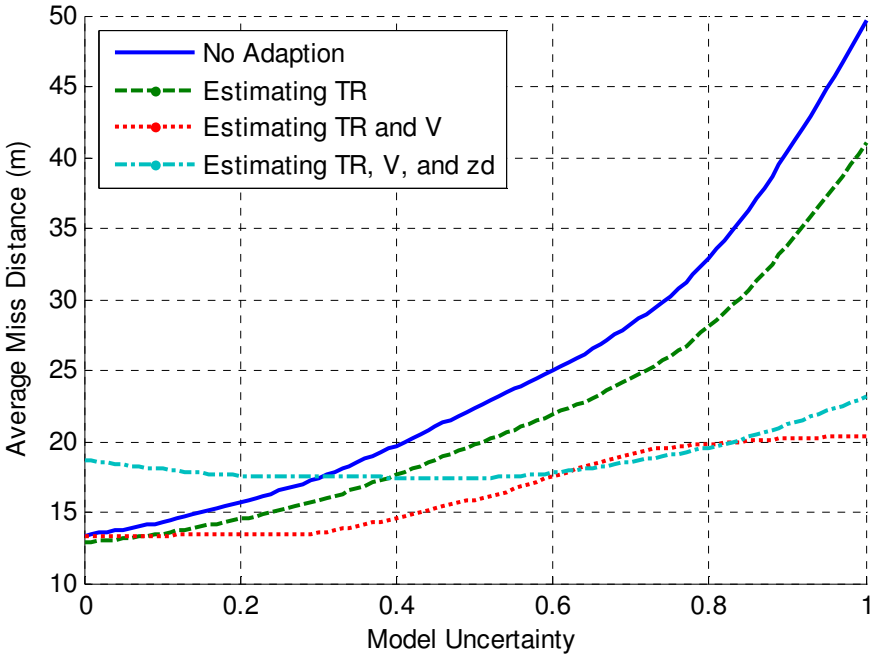

Figure 8.17: Simulated Landing Accuracy vs. Model Uncertainty with Increasing Levels of In-Flight System Identification

For the first case with no adaptation of the in-flight model, the average miss distance is increased dramatically as model uncertainty is increased. The landing accuracy with no model uncertainty is 13 meters, while the average landing accuracy with the model uncertainty at the maximum level is 50 meters, an increase of a factor of 4. This is to be expected since the internal model is diverging from the actual flight characteristics of the system. For the second case, with the turn rate and control bias models adjusted to match

in-flight estimates, the landing accuracy is somewhat improved. The average landing accuracy at the maximum level of model uncertainty in this case is reduced to 40 meters, a 20% improvement over the case with no adaptation. When both turn rate characteristics and airspeed model are adapted to match in-flight estimates, the landing error is reduced dramatically. For model errors up to 25% there is essentially no degradation in landing accuracy, and with model errors at maximum the landing error has only risen to 20 meters. For the final case, where the internal turn rate, airspeed, and descent rate models are all set to match flight test data, there is no improvement in landing accuracy compared to the case where descent rate is not estimated in flight. In fact, with low levels of model uncertainty, the landing accuracy is actually slightly degraded when the descent rate is estimated in flight. This indicates that descent rate estimates corrupted by vertical wind were still used to update the internal model, despite the threshold placed on standard deviation based on Figure 8.10. This means that the descent rate of a parafoil and payload system can only be reliably estimated in very calm conditions.

To summarize, in-flight estimation of the turn rate and airspeed characteristics of a parafoil and payload aircraft can be reliably estimated in-flight with only GPS and a barometric altimeter during the descent to target. The use of these in-flight estimates to update the internal turn rate and airspeed models used for guidance, navigation, and control calculations can dramatically increase the landing accuracy in situations where there is a significant amount of uncertainty in the aircraft flight characteristics.

CHAPTER 9

CONCLUSIONS

Current guided parafoil systems generally use very similar guidance, navigation and control techniques. Differential trailing edge brake control is used for steering, and some sort of optimal approach maneuver is used to plan a path that will place the system on the desired impact point just as it runs out of altitude. With only lateral control available, these systems have a limited capacity to react to any large changes in wind during final approach.

The goal of this dissertation is to provide a number of novel improvements to the standard guided parafoil guidance, navigation, and control architecture to enable increased autonomous landing accuracy. The primary contributions of this dissertation are: 1) the development of a reliable and robust method to identify a flight dynamic model for a parafoil and payload aircraft using minimal sensor data; 2) the first demonstration in flight test of the ability to achieve large changes in glide slope over ground using coupled incidence angle variation and trailing edge brake deflection; 3) the first development of a control law to implement glide slope control on an autonomous system; 4) the first flight tests of autonomous landing with a glide slope control mechanism demonstrating an improvement in landing accuracy by a factor of 2 or more in especially windy conditions, and 5) the first demonstrations in both simulation and flight test of the ability to perform in-flight system identification to adapt the internal

control mappings to flight data and provide dramatic improvements in landing accuracy when there is a significant discrepancy between the assumed and actual flight characteristics.

While all of the simulation and flight test results presented in this dissertation focus on small systems constructed solely for research purposes, all of the findings presented here are applicable to full scale airdrop systems. The guidance, navigation and control algorithms are all based solely on position and velocity feedback already available on all modern guided airdrop systems. While incidence angle control is not a typical feature of current systems, the promising results presented here suggest that it is worth considering this extra control channel for full-size systems in the future. The extra servo motor required for incidence angle control channel should not be a significant addition in cost or complexity to standard full-size systems. Even without incidence angle control, the in-flight system identification procedure would be simple to implement on current systems and the glide slope control algorithm presented here can still be used to provide a significant variation in glide slope over ground using only symmetric trailing edge brake deflection in windy conditions. These modifications could provide a significant improvement in the performance of current guided systems with only relatively simple modifications to flight software.

References

[1] Poynter, D., The Parachute Manual, A Technical Treatise on Aerodynamic Decelerators, Para Publishing, California, 1972.

[2] Bates, J., *Parachuting, from Student to Skydiver*, Tab Books, Pennsylvania, 1990.

[3] Meeks, C., *Skydiving*, Capstone Press, Minnesota, 1991.

[4] Painter, K.M., "Help from the Skies," *Popular Mechanics Magazine,* Vol. 52, No. 5, Nov. 1929, pp. 762-766.

[5] Ducote, R., Speelman, R., "Air Force Concepts for Accurate Delivery of Equipment and Supplies," *Journal of Aircraft,* Vol. 4, No. 4., Jul-Aug 1967, pp 383-392.

[6] Desabrais, K., "The Motion and Aerodynamics of an Airdrop Platform," 22nd AIAA Applied Aerodynamics Conference and Exhibit, Providence, Rhode Island, Aug. 16-19, 2004.

[7] Gionfriddo, M., "A survey of the U.S. Army R&D Programs in Airdrop," *AIAA Aerodynamic Deceleration Systems Conference,* Sept 7-9, 1966.

[8] Gionfriddo, M., "U.S. Army Airdrop Technology Needs for the Future," AIAA 89-0877, 1989.

[9] Computed Air Release Point Procedures, Air Force Instruction 11-231, August 2005.

[10] Hattis, P, et al., "An Advanced Onboard Airdrop Planner to Facilitate Precision Payload Delviery," *AIAA Modeling and Simulation Technologies Conference and Exhibit*, 14-17 August 2000.

[11] Hattis, P, et al., "Status of an Onboard PC-Based Airdrop Planner Demonstration", . AIAA 2001-2066, 2001.

[12] Campbell, D., et al., "An Onboard Mission Planning System to Facilitate Precision Airdrop," AIAA 2005-7071, 2005.

[13] Wright, R., Benney, R., McHugh, J., “An On-Board 4D Atmospheric Modeling System to Support Precision Airdrop,” AIAA 2005-7070, 2005.

[14] Wright, R., Benney, R., McHugh, J., “Precision Airdrop System,” AIAA 2005-1644, 2005.

[15] Dellicker, S., Benney, R., Brown, G., “Guidance and Control for Flat-Circular Parachutes”, Journal of Aircraft, Vol. 38, No. 5, Sep-Oct 2001, pp 809-817.

[16] Gilles, B., Hickey, M., Krainski, W., “Flight Testing of a Low-Cost Precision Aerial Delivery System,” 18th *AIAA Aerodynamic Decelerator Systems Technology Conference and Seminar*, 2005.

[17] Jorgenson D., Hickey, M., “The AGAS 2000 Precision Delivery System,” 18th *AIAA Aerodynamic Decelerator Systems Technology Conference and Seminar*, 2005.

[18] Nicolaides, J. D. and Knapp, C. F., “A Preliminary Study of the Aerodynamic and Flight Performance of the Para-Foil,” *Conference on Aerodynamic Deceleration*, University of Minnesota, July 8, 1965.

[19] Nicolaides, J. D., "On the Discovery and Research of the Para-Foil," *International Congress on Air Technology*, Little Rock, Ark., Nov. 1965.

[20] Nicolaides, J. D., “A review of Para-Foil Applications,” *Journal of Aircraft*, Vol. 7 No. 5, Sep-Oct 1970, pp 423-431.

[21] Nicolaides, J., “Parafoil Wind Tunnel Tests,” AFFDL-TR-70-146., U.S. Air Force Flight Dynamics Lab., Wright-Patterson Air Force Base, Ohio.

[22] Ware, G.M., Hassell, J.L., Jr., “Wind-Tunnel Investigation of Ram-Air-Inflated All-Flexible Wings of Aspect Ratios 1.0 to 3.0”, TM SX-1923, NASA, 1969.

[23] Nicolaides, J., and Tragarz, M., “Parafoil Flight Performance,” *AIAA Aerodynamic Decelerator Conference*, Sept. 1970.

[24] Nicolaides, J., “Improved Aeronautical Efficiency through Packable Weightless Wings,” AIAA Paper 70-880, 1970.

[25] Knapp, C., Barton, W., “Controlled Recovery of Payloads at Large Glide Distances, Using the Para-Foil,” Journal of Aircraft, Vol. 5 No. 2, Mar-Apr 1968, pp. 112-118.

[26] Goodrick, T., “Estimation of Wind Effect on Gliding Parachute Cargo Systems using Computer Simulation,” *AIAA Aerodynamic Decelerator Systems Conference*, Ohio, Sept 14-16, 1970.

[27] Goodrick, T., Pearson, A., and Murphy, A., “Analysis of Various Automatic Homing Techniques for Gliding Airdrop Systems with Comparative Performance in Adverse Winds,” 4th AIAA Aerodynamic Decelerator Conference, Palm Springs, CA, 1973.

[28] Mayer, R., “Terminal Descent Controlled Vehicle Recovery,” AIAA Paper 84-0801, 1984.

[29] Murray, J., Sim, A., Neufeld, D., Rennich, P., Norris, S., and Hughes W., "Further Development and Flight Test of an Autonomous Precision Landing System Using a Parafoil," NASA TM-4599, July 1994.

[30] Sim, A.G, Murray, J.E., Neufeld, D.C., and Reed, R.D., "Development and Flight Test of a Deployable Precision Landing System for Spacecraft Recovery," NASA Technical Memorandum #4525, 1993.

[31] Sim, A., Murray, J., Neufeld, D., and Reed, R., “Development and Flight Testing of a Deployable Precision Landing System,” Journal of Aircraft, Vol. 31, No. 5, Sep-Oct 1994, pp 1101-1108.

[32] Hattis, P., et al, "Precision Guided Airdrop System Flight Test Results," Proceedings of the 14th AIAA Aero-dynamic Decelerator Systems Technology Conference, San Francisco, CA, June 3-5, 1997.

[33] Hogue, J.R., and Jex, H.R., "Applying Parachute Canopy Control and Guidance Methodology to Advanced Precision Airborne Delivery Systems," *Proceedings of the 13th AIAA Aerodynamic Decelerator Systems Technology Conference*, Clearwater Beach, FL, May 15-18, 1995.

[34] Smith, B.D., "Steering Algorithms for GPS Guidance of RAM-AIR Parachutes," *Proceedings the 8th International Technical Meeting of the Institute of Navigation,* Palm Springs, CA, September 12-15, 1995.

[35] Development and Demonstration Test of a Ram-Air Parafoil Precision Guided Airdrop System, Volume 3, Simulation and Flight Test Results, Final Report CSDL-R-2752, Draper Laboratory, U.S. Army Contract #DAAK60-94-C-0041, October 1996.

[36] Development and Demonstration Test of a Ram-Air Parafoil Precision Guided Airdrop System, Addendum: Flight Test Results and Software Updates after Flight 19, Final Report CSDL-R-2771, Draper Laboratory, U.S. Army Contract #DAAK60-94-C-0041, December 1996.

[37] Hattis, P.O., et al, "Precision Guided Airdrop System Flight Test Results," Proceedings of the 14th AIAA Aero-dynamic Decelerator Systems Technology Conference, San Francisco, CA, June 3-5, 1997.

[38] Gockel, W., "Concept Studies of an Autonomous GNC System for Gliding Parachute," Proceedings of the 14th AIAA Aerodynamic Decelerator Systems Technology Conference, San Francisco, CA, June 3-5, 1997.

[39] Soppa, U., Strauch, H., Goerig, L., Belmont, J.P., and Cantinaud, O., "GNC Concept for Automated Landing of a Large Parafoil," Proceedings of the 14th AIAA Aerody-namic Decelerator Systems Technology Conference, San Francisco, CA, June 3-5, 1997.

[40] Kaminer, I., and Yakimenko, O., "Development of Control Algorithm for the Autonomous Gliding Delivery System," AIAA Paper 2003-2116, May 2003.

[41] Carter, D., George, S., Hattis, P., Singh, L., and Tavan, S., "Autonomous Guidance, Navigation, and Control of Large Parafoils," AIAA Paper 2005-1643, May 2005.

[42] Jann, T., "Advanced Features for Autonomous Parafoil Guidance, Navigation and Control," AIAA Paper 2005-1642, May 2005.

[43] Carter, D., George, S., Hattis, P., McConley, M., Rasmussen, S., Singh, L., and Tavan, S., "Autonomous Large Parafoil Guidance, Navigation, and Control System Design Status," AIAA Paper 2007-2514, May 2007.

[44] Calise, A., and Preston, D., "Swarming/Flocking and Collision Avoidance for Mass Airdrop of Autonomous Guided Parafoils," *Journal of Guidance, Control, and Dynamics*, Vol. 31, No. 4, 2008, pp 1123--1132.

[45] Carter, D., Singh, L., Wholey, L., Rasmussen, S., Barrows, T., George, S., McConley, M., Gibson, C., Tavan, S., and Bagdonovich, B., "Band-Limited Guidance and Control of Large Parafoils," AIAA Paper 2009-2981, May 2009.

[46] Slegers, N., and Yakimenko, O., "Optimal Control for Terminal Guidance of Autonomous Parafoils," AIAA Paper 2009-2958, 2009.

[47] Tavan, S., "Status and Context of High Altitude Precision Aerial Delivery Systems," AIAA Paper 2006-6793, 2006.

[48] Yakimenko, O., Slegers, N., and Tiaden, R., "Development and Testing of the Miniature Aerial Delivery System Snowflake," AIAA Paper 2009-2980, 2009.

[49] Slegers, N., Beyers, E., and Costello, M., "Use of Variable Incidence Angle for Glide Slope Control of Autonomous Parafoils," *Journal of Guidance, Control, and Dynamics*, Vol. 31, No. 3, 2008, pp 585-596.

[50] Calise, A., and Preston, D., "Design of a Stability Augmentation System for Airdrop of Autonomous Guided Parafoils," AIAA Paper 2006-6776, May 2006.

[51] Goodrick, T.F., "Theoretical study of the longitudinal stability of high-performance gliding airdrop systems," AIAA Paper 1975-1394, 5th AIAA ADS Conference, Albuquerque, NM, November 17-19, 1975.

[52] Crimi, P., "Lateral Stability of Gliding Parachutes," *Journal of Guidance, Control Dynamics*, Vol. 13 No. 6, 1990.

[53] Iosilevskii, G., "Center of Gravity and Minimal Lift Coefficient Limits of a Gliding Parachute," *Journal of Aircraft*, Vol. 32 No. 6, 1995, pp.1297-1302.

[54] Goodrick, T.F., "Simulation studies of the flight dynamics of gliding parachute systems," AIAA Paper 1979-0417, 1979.

[55] Goodrick, T.F., "Comparison of simulation and experimental data for a gliding parachute in dynamic flight," AIAA Paper 1981-1924, 1981.

[56] Slegers, N., and Costello, M., "Aspects of Control for Parafoil and Payload System," *Journal of Guidance, Control, and Dynamics*, Volume 26, Number 6, pp. 898-905, November-December 2003.

[57] Mooij, E., Wijnands, Q. G. J., and Schat, B., "9 DoF Parafoil/Payload Simulator Development and Validation," *AIAA Modeling and Simulation Technologies Conference*, Austin, Texas, August 2003.

[58] Prakash, O., Ananthkrishnan, N., "Modeling and Simulation of 9-DOF Parafoil-Payload System Flight Dynamics," *AIAA Atmospheric Flight Mechanics Conference and Exhibit* 21 - 24 August 2006, Keystone, Colorado.

[59] Gorman, C., Slegers, N., "Comparison and Analysis of Multi-Body Parafoil Models with Varying Degrees of Freedom," *21st AIAA Aerodynamic Decelerator Systems Technology Conference and Seminar*, Dublin, Ireland, 23 - 26 May 2011.

[60] Lissaman, P., Brown, G., "Apparent Mass Effects on Parafoil Dynamics," AIAA-1993-1236, *12th AIAA Aerodynamic Decelerator Systems Technology Conference and Seminar*, London, England, May 10-13, 1993.

[61] Barrows, T.M., "Apparent mass of parafoils with spanwise camber," *16th AIAA Aerodynamic Decelerator Systems Technology Conference and Seminar*, Boston, MA, May 21-24, 2001.

[62] Barrows, T.M., "Apparent mass of parafoils with spanwise camber," *Journal of Aircraft*, Vol. 39 no. 3, 2002.

[63] "Military Specification, Flying Qualities of Piloted Airplanes," MIL-F-8785C, Aug. 1980.

[64] "Background Information and User Guide for MIL-F-8785B", Air Force Flight Dynamics Laboratory, August 1969.

[65] "Background Information and User Guide for MIL-F-8785C", Air Force Flight Dynamics Laboratory, July 1982.

[66] "Military Standard, Flying Qualities of Piloted Aircraft," MIL-STD-1797A, Jan. 1990.

[67] Gage, S., "Creating a Unified Graphical Wind Turbulence Model from Multiple Specifications," *AIAA Modeling and Simulation Technologies Conference and Exhibit*, Austin, Texas, 11-14 August 2003.

[68] Etkin, B., *Dynamics of Atmospheric Flight*, Wiley, New York, 1972.

[69] Klein, V., and Morelli, E., *Aircraft System Identification: Theory and Practice*, AIAA Education Series, Virginia, 2006.

[70] Jategaonkar, R. V., *Flight Vehicle System Identification: A Time Domain Approach*, AIAA Education Series, Virginia, 2006.

[71] Jann, T., Doherr, K., and Gockel, W., "Parafoil Test Vehicle ALEX – Further Development and Flight Test Results", AIAA-1999-1751, *15th CEAS/AIAA Aerodynamic Decelerator Systems Technology Conference,* Toulouse, France, June 8-11, 1999.

[72] Jann, T., "Aerodynamic Model Identification and GNC Design for the Parafoil-Load System ALEX," AIAA-2001-2015, *16th AIAA Aerodynamic Decelerator Systems Technology Conference and Seminar*, Boston, MA, May 21-24, 2001.

[73] Jann, T., "Aerodynamic Coefficients for a Parafoil Wing with Arc Anhedral –Theoretical and Experimental Results," AIAA-2003-2106, *17th AIAA Aerodynamic Decelerator Systems Technology Conference and Seminar*, Monterey, California, May 19-22, 2003.

[74] Jann, T., and Strickert, G., "System Identification of a Parafoil-Load Vehicle--Lessons Learned," AIAA-2005-1663, *18th AIAA Aerodynamic Decelerator Systems Technology Conference and Seminar*, Munich, Germany, May 23-26, 2005.

[75] Hur, G., and Valasek, J., "System Identification of Powered Parafoil-Vehicle from Flight Test Data," AIAA-2003-5539, *Proceedings of the AIAA Atmospheric Flight Mechanics Conference*, Austin, TX, 11-14 August 2003.

[76] Valasek, J., and Chen, W., "Observer/Kalman Filter Identification for Online System Identification of Aircraft," *Journal of Guidance, Control, and Dynamics*, Volume 26, Number 2, pp. 347-353, March-April 2003.

[77] Kothandaraman, G., and Rotea, M., "Simultaneous-Perturbation-Stochastic-Approximation Algorithm for Parachute Parameter Estimation," *Journal of Aircraft*, Volume 42, Number 5, September-October 2005.

[78] Yakimenko, O., and Statnikov, R., "Multicriteria Parametrical Identification of the Parafoil-Load Delivery System," AIAA-2005-1664, *18th AIAA Aerodynamic Decelerator Systems Technology Conference and Seminar*, Munich, Germany, May 23-26, 2005.

[79] Majji, M., and Juang, J., and Junkins, J., "Time-Varying Eigensystem Realization Algorithm," *Journal of Guidance, Control, and Dynamics*, Vol. 33, No. 1, pp. 13-28, January-February 2010.

[80] Majji, M., and Juang, J., and Junkins, J., "Observer/Kalman-Filter Time-Varying System Identification," *Journal of Guidance, Control, and Dynamics*, Vol. 33, No. 3, pp. 887-900, May-June 2010.

[81] Press, W., Teukolsky, S., Vetterling, W., and Flannery, B., *Numerical Recipes in Fortran 77*, 2nd Ed., Cambridge University Press, New York, 1992, Chaps. 9.6, 15.5.

[82] Chui, C.K., and Chen, G., *Kalman Filtering with Real-Time Applications*, 3rd ed., Springer-Verlag, New York, 1999, Chap. 8.

[83] Iacomini, C., and Cerimele, C., "Longitudinal Aerodynamics from a Large Scale Parafoil Test Program", AIAA Paper 99-1732, 1999.

[84] Airborne Systems, Product List. http://www.airborne-sys.com/products.htm, Aug. 2010.

[85] Gradient, Glider Technical Data, http://www.gradient.cx/en/gliders, Aug. 2010.

[86] Skywalk, Glider Technical Data, http://www.skywalk.info, Aug. 2010.

[87] Calise, A., Preston, D., "Approximate Correction of Guidance Commands for Winds," 20th AIAA Aerodynamic Decelerator Systems Technology Conference and Seminar, 4 - 7 May 2009, Seattle, Washington.